Title

Probing the Nature of Cataclysmic Variables via Photometric Studies on Multiple Timescales /

Permalink

https://escholarship.org/uc/item/9s16v2cv

Author

Armstrong, Eve

Publication Date

2013

Peer reviewed|Thesis/dissertation

UNIVERSITY OF CALIFORNIA, SAN DIEGO

Probing the Nature of Cataclysmic Variables via Photometric Studies on Multiple Timescales

A dissertation submitted in partial satisfaction of the requirements for the degree

Doctor of Philosophy

in

Physics

by

Eve Armstrong

Committee in charge:

Richard Rothschild, Chair
Adam Burgasser
Judy Kim
Hans Paar
Joseph Patterson
Barney Rickett

2013

The dissertation of Eve Armstrong is approved, and it is acceptable in quality and form for publication on microfilm and electronically:

Chair

University of California, San Diego

2013

DEDICATION

To Mom and Dad – Ellen and Peter, Sara, and Wayne

EPIGRAPH

"If it is any point requiring reflection ... we shall examine it to better purpose in the dark."
Edgar Allan Poe; *The Purloined Letter* (1845)

CONTENTS

FIGURES

TABLES

ACKNOWLEDGEMENTS

Family

Mom and Dad, Ellen and Peter Armstrong: From Day 1, you took my curious, adventurous spirit – which every child is born with – and lit it on fire. Never did you implant the notion that there existed an enterprise that my brain couldn't tackle. Thanks to your love and support, life has been a rich, bizarre, fascinating adventure.

Wayne Yeager: with you I know that it will continue to be. You are inspired and passionate. I knew that life with you would center on Now, because you understand that plans can be okay until they get squished by a passing Mack truck. And without you egging me on, this document wouldn't have materialized.

Sara Armstrong: I struck it rich having you as a partner in crime. The day you so deviously reconstructed that Rubik's Cube, I realized you were smarter than me. At the time, I was horrified. Now I could not be more proud of you. The only thing more beautiful than your brain is your heart.

Sam Selesnick and Philip Stieg: I have long admired the combination of spirit, drive, dedication, and talent. You showed me that there exist people who direct those qualities toward achieving an end that is just-plain good. Thank you for that. And thank you for the X number of years I have ahead to smile and run and eat peanut butter cornmeal pancakes and write dissertations.

Friends

Joe Patterson: thank you for sharing your physical intuition and for your faith that I would catch on sooner or later. I am lucky that as an impressionable first-year undergraduate, my introduction to this field was your high valuation of creativity in science and the pride you take in your methodology. You set a standard that, since then, few others have met.

Rick Rothschild: for your willingness to serve as Adviser at a Distance of 3000 Miles. From the start, that demonstration of trust was a confidence booster. For illuminating discussions on contact binaries of all colors, and for encouraging me to take a deep breath now and then.

George Fuller: for the spirit with which you approach a problem and – it seems – life in general. For your predilection for dark humor, which is a rare find in this neck of the woods. And for ruminations on the roles of women, synonyms, and magic hexes in academia.

Hans Paar: for your unhesitating welcome back to the department following an out-of-the-blue email from someone who, quite possibly, was merely suffering post-craniotomy brain damage.

Adam Burgasser: for suggestions on data interpretation, welcoming me to the Stars & Planets crowd, and for a healthful perspective on Being a Graduate Student.

David Helfand: for an impressive first impression of what “research” is supposed to mean. For your expectation that people use their brains in everyday life, and your eagerness to teach those who aren’t accustomed to that notion but are willing to adapt. And for the faculty e-profile photo of your electro-shock therapy.

Jules Halpern: for teaching me to master the 1.3-meter, setting an example that was difficult to match, and helping me stay awake via *A Prairie Home Companion*.

Eric Michelsen: for your continually renewed shock at being the sole adherer to your standards of integrity, despite the accumulation of bountiful evidence. For creating lightcurve.exe and lending me your cot.

Laura Tucker for moral support, brainstorming sessions, and crooning Gershwin through the condiments aisle at Ralph’s. Nancy Santagata for your dismay when I washed my hands of this the first time around, and for pink slug hunting at Black’s Beach. Bob Barr, Tony Negrete, Paul Hartmann for making MDM a home, and for terrifying tales o’ The

Creeper. The Creeper for your beneficence. Dana Johnson for situating me with ease every time I intermittently show up, and for being such fun as a neighbor down the hall. Alex Markowitz, Paul Hemphill, Evan Grohs for helping me wrestle my defense into coherent English sentences. John Thorstensen for your infectious enthusiasm. Ed Spiegel for the most engaging lectures of all time. Helena Uthas for pointing me to Python. Jonathan Kemp for invaluable reduction scripts. Kevin Smith for breathing life into my CASS desktop and rendering my hatchet unnecessary. Aleks Simic, Andrew Meyertholen, Adam Orin, Tyler Grassman, Evan Bierman for your friendships.

Accomplices

I thank my committee members: Joe Patterson, Rick Rothschild, Hans Paar, Adam Burgasser, Judy Kim, and Barney Rickett.

Chapters 3 and 4, in part, are reproductions of material as it appears in Monthly Notices of the Royal Astronomical Society: Armstrong, E., Patterson, J., Kemp, J. 2012, MNRAS, 421, 2310.

Chapters 5 and 6, in part, are being prepared for submission for publication, with the following authors: Armstrong, E., Patterson, J.

Chapter 7, in part, is a reproduction of material as it appears in Monthly Notices of the Royal Astronomical Society, 2013: Armstrong, E., Patterson, J., Michelsen, E., Uthas, H., Vanmunster, T., Hambsch, F.-J., Roberts, G., Dvorak, S. 2013, MNRAS, DOI: 10.1093/mnras/stt1335.

This dissertation author was the primary investigator and author of the material contained in chapters 3 through 7.

VITA

2011 – 2013	Ph. D. Physics: University of California, San Diego
2009 – 2013	Adjunct professor: Cooper Union for the Advancement of Science and Art
2010 – 2012	Adjunct professor: City University of New York
2008 – 2013	Co-artistic director: Reality Aside Theatre, Inc.
2004 – 2006	M.S. Physics: University of CA, San Diego
1998 – 2002	B.A. Astrophysics: Columbia College; Columbia University

PUBLICATIONS

1. Armstrong, E., Patterson, J., Michelsen, E., Thorstensen, J., Uthas, H., Vanmunster, T., Hambsch, F.-J., Roberts, G., Dvorak, S. *Orbital, Superhump, and Superorbital Periods in the Cataclysmic Variables AQ Mensae and IM Eridani*, 2013, Monthly Notices of the Royal Astronomical Society (MNRAS), DOI: 10.1093/mnras/stt1335

2. Armstrong, E., Patterson, J., Kemp, J. *Two Photometric Periods in the AM CVn System CP Eridani*, 2012, MNRAS, 421, 2310

3. Armstrong, E., Patterson, J. *Orbital period evolution and orbital sideband structure in AM Canum Venaticorum*, in preparation

4. Armstrong, E. et. al. *GRB 060102: MDM Observation*, 2006, GRB Coordinates Network, Circular Service, 4427, 1

5. Skinner, J., Thorstensen, J., Armstrong, E., Brady, S. *The New Eclipsing Cataclysmic Variable SDSS 154453+255*, 2011, Publications of the Astron. Soc. of the Pacific (PASP), 123, 901

6. Copperwheat, C.M., Marsh, T., Dhillon, V., Littlefair, S., Woudt, A., Warner, B., Patterson, J., Steeghs, D., Kemp, J., Armstrong, E., Rea, R. *The Photometric Period in ES Ceti*, 2011, MNRAS, 413, 3068

7. Dai, X, Halpern, J., Morgan, N., Armstrong, E., Mirabal, N., Haislip, J., Reichart, D., Stanek, K. *Optical and X-Ray Observations of GRB 060526: A Complex Afterglow Consistent with an Achromatic Jet Break,* 2007, Astrophysical Journal (Ap J), 658, 509

8. Thorstensen, J; Armstrong, E. *Is FIRST J102347.6+003841 Really a Cataclysmic Binary?*, 2005, Astronomical Journal (AJ), 130, 759

9. Patterson, J., Thorstensen, J., Armstrong, E. *The Dwarf Nova PQ Andromedae*, 2005, PASP, 117, 922

10. Patterson, J., Kemp, J., Harvey, D., Fried, R., Rea, R., Monard, B., Cook, L., Skillman, D., and 12 co-authors. *Superhumps in Cataclysmic Binaries. XXV.* q_{crit}*, epsilon(q), and Mass-Radius*, 2005, PASP, 117, 1204

11. Helfand, David, et al. Frontiers of Science. Columbia University, 2004

12. Patterson, J., Thorstensen, J., Vanmunster, T., Fried, R., Martin, B., Campbell, T., Robertson, J., Kemp, J., Messier, D., Armstrong, E. *Rapid Oscillations in Cataclysmic Variables. XVI. DW Cancri*, 2004, PASP, 116, 516

13. Pretorius, M.L. Woudt, P., Warner, B., Bolt, G., Patterson, J., Armstrong, E. *High-speed photometry of SDSS J013701.06 - 091234.9*, 2004, MNRAS, 352, 1056

14. Mirabal, N. Halpern, J., Chornock, R., Filippenko, A., Terndrup, D., Armstrong, E., Kemp, J., Thorstensen, J., Tavarez, M., Espaillat, C. *GRB 021004: A Possible Shell Nebula around a Wolf-Rayet Star Gamma-Ray Burst Progenitor*, 2003, Ap J, 595, 935

15. Armstrong, E. *Non-detection of the Tooth Fairy at Optical Wavelengths*, 2012 Mar 31, eprint arXiv:1204.0492

ABSTRACT OF THE DISSERTATION

Probing the Nature of Cataclysmic Variables via Photometric Studies on Multiple Timescales

by

Eve Armstrong

Doctor of Philosophy in Physics

University of California, San Diego, 2013

Richard Rothschild (Chair)

I examine the structure and evolution of hydrogen- and helium-rich cataclysmic variables (CVs), via their periodic variability captured by long-term time series photometry. Studies to be discussed address one of two sets of question.

One set pertains to helium CVs, which are poorly understood relative to their hydrogen-rich counterparts: *What is the long-term evolution – in terms of orbital period (P_{orb}) – of He CVs, and what does this imply about the nature of their secondaries?* Two methods of investigation are employed: i) using systems with positive superhump and orbital period

detections (Chapter 3) in order to chart the distribution of P_{orb} versus time for He CVs (Chapter 4); ii) direct pulse timing of P_{orb} in one system, via an 18-year baseline of photometry (Chapter 5). Results of the first study indicate that helium CVs are evolving toward longer P_{orb} and have secondaries that are well described as degenerate objects. The pulse timing of one object (and the same measurement in two other He CVs) shows no evidence for P_{orb} lengthening, and is consistent with P_{orb} shortening driven by angular momentum loss via gravitational wave radiation. Technically, the two results are not inconsistent, as AM CVn is the only point on the distribution with a P_{orb} timing. The apparent contradiction, however, illuminates our poor understanding of this class of CV: their routes to birth and the range of paths that a star can take following core hydrogen burning.

The second set of studies pertains to signals associated with the accretion disc: *Can a CV's accretion disc tilt with respect to the orbital plane? And what is the geometry and behavior of matter at various annuli in a tilted disc?* To this end, I examine orbital sideband signals in AM CVn (Chapter 6) and simultaneous orbital sidebands and superorbital signals in two hydrogen CVs (Chapter 7). I also tabulate, from the literature, ten additional CVs with reliable detections of these signals (Chapter 7). All results indicate that the mechanism of tilt is at work in these objects.

1 Cataclysmic Variable Stars

“Hear the loud alarum bells – Brazen bells!
What a tale of terror, now, their turbulency tells!
In the startled ear of night
How they scream out their affright!
Too much horrified to speak,
They can only shriek, shriek,
Out of tune”
Poe; *The Bells* (1848)

1.1 Background and the basic picture of a cataclysmic variable

Note: Sections 1.1 and 1.2 are designed for a reader with little knowledge of compact binaries. Other readers will miss nothing by beginning with §1.1.3.

1.1.1 Discovery

Observations of binary stars became common during the first half of the 20th century. They were studied by means of a light curve: a series of exposures that capture the variability of an object’s brightness over time. The most readily identifiable characteristic in the light curve of a binary was the presence of eclipses, from which an orbital period – the period at which the stars orbit their common center of mass – can be derived. At the time, a typical orbital period (hereafter P_{orb}) was between 8 – 12 hours. This range constrained the systems’ sizes and the densities of their stellar components, which were inferred to be stars of approximately a solar mass ($M_\odot$) undergoing core hydrogen burning (e.g. Chandrasekhar 1939).

Around 1950, two objects were identified as binaries with orbital motions of unprecedented speed (UX Ursa Majoris (Linnell 1949) and DQ Herculis (Walker 1954; Walker 1956)): around 4 hours and 40 minutes for each star. For a binary-star model to apply in these cases, one component must be denser and closer to the system's center of mass; moreover, the orbital separation would have to be significantly smaller. Thus there emerged a picture of a "compact binary", in which the mass donor is a hydrogen-burning star and the accretor is a white dwarf (WD): a ~ $1M_\odot$ star of He/C composition, which has completed nuclear burning and is supported primarily by electron degeneracy pressure (Schwarzschild 1958).

These short-period binaries show complicated light curves that are highly variable in magnitude on multiple timescales. Brightness often spans three magnitudes (in a single system), and in rare cases as many as 19 (flux ratios of ~ 10 to 10^7, respectively), on timescales of minutes to 100 years. Such behavior is suggestive of a system more complex than one containing two stellar components that are gravitationally bound but otherwise non-interacting. The magnitude changes suggest explosive events. The low coherence of some signals suggests that some of the matter in the system exists in a configuration less rigid than that which stellar structure permits. Furthermore, spectroscopy of these objects shows double-peaked emission line profiles – which are a signature of Doppler broadening, and they are superimposed upon a broad black-body flux distribution across wavelength – implying a multi-temperature object. The picture that emerges is of mass transfer via an accretion disc. In this scenario, the orbital separation is sufficiently small for the gravity of the white dwarf to accrete matter from its companion. Mass transfer causes varying brightness, due both to encounters with the WD surface and to varying viscosity, temperature, and radius of the disc.

Light at all optical wavelengths is dominated by disc emission, and hence the optical spectra indicate the makeup of the mass-donating star: typically CVs show strong hydrogen lines, indicating a low-mass main sequence star donor.

These compact binaries, in which a WD (the "primary") accretes matter from a lower-mass companion (the "secondary"), are cataclysmic variables (CVs). Fig. 1.1 shows the main components of a CV with a hydrogen-rich secondary. Roughly 2,500 CVs have been identified (Downes et al. 2005).

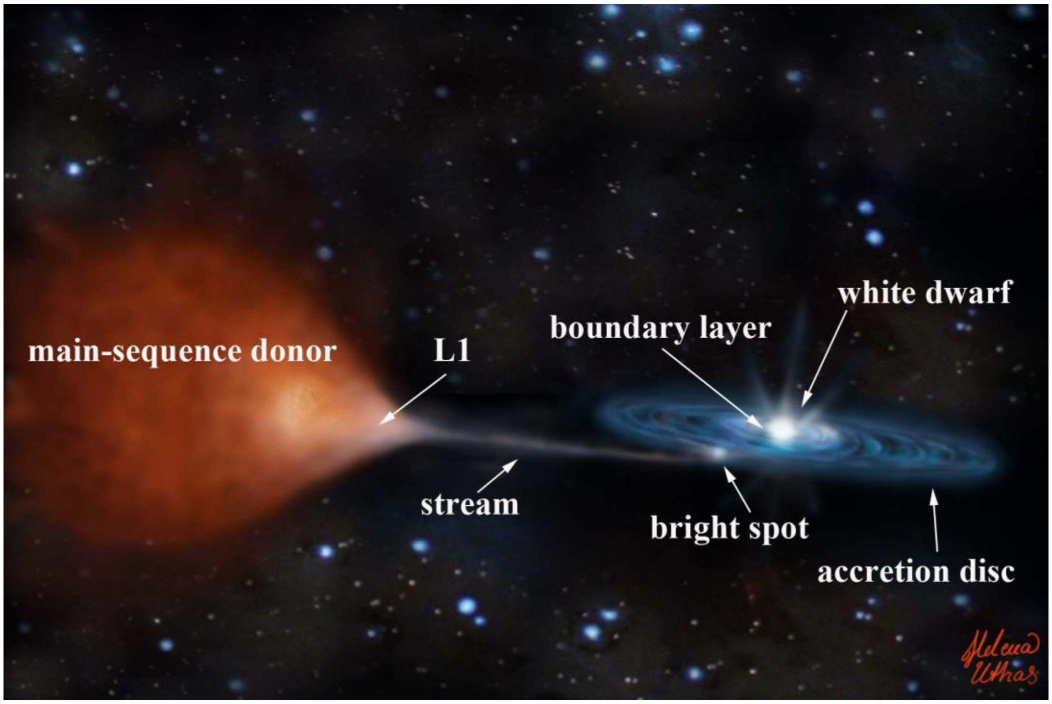

Fig. 1.1: Basic components of a hydrogen CV (Uthas 2010).

Using Roche geometry (§1.2.6.2), Kepler's law, angular momentum considerations (§1.2.6.3), and characterizing the secondary in terms of mass and evolutionary stage, we infer the sizes of CVs, their evolutionary histories, and likely futures. An understanding of CVs can illuminate broader questions in astrophysics, including the nature of accretion discs, rates of Type 1a SNe, post-main sequence evolution, and models of gravitational wave radiation. The following list of basic CV terminology (Table 1.1) may be a useful reference throughout this dissertation.

Table 1.1: Basic CV terminology to be used frequently throughout this dissertation

Term	*Definition*
binary	a system in which two stars orbit their common center of mass
accreting binary	a binary in which the higher-mass star accretes matter from its companion
primary	the higher-mass (accreting) stellar component
secondary; donor	the lower-mass stellar component
mass ratio (q)	the ratio of secondary mass to primary mass
accretion disc; disc	the structure that accreting matter assumes upon its trajectory toward the primary
accretion stream	the stream of matter traveling from the secondary to the disc
bright spot; hot spot	the area of enhanced luminosity where the accretion stream impacts the disc
orbital period; period	the period of revolution of the primary and secondary about their common center of mass
hydrogen burning	the process within a stellar core in which hydrogen is fused into helium
main-sequence star	a star undergoing core hydrogen burning
helium burning	the process within the core of a helium-enriched star, in which helium is fused into heavier elements; follows core H burning
red giant	a star that has recently completed core-H burning and whose atmosphere has expanded by many orders of magnitude; in a binary, this atmosphere becomes the “common envelope”
white dwarf	the cooling core of a star that has completed burning and lost its outer envelope, is of ~ He/C composition, and is supported primarily by electron degeneracy pressure
CV; white dwarf binary	an accreting binary in which the primary is a white dwarf
Hydrogen CV; H CV	a CV with a spectrum dominated by hydrogen lines, and whose secondary is inferred to be a H-burning star of ~ solar mass
Helium CV; He CV; AM CVn star	a CV with a spectrum dominated by He lines (and no H), whose secondary is inferred to have evolved beyond main sequence burning.
common envelope phase	the stage of evolution prior to the birth of a H CV, where both stellar components reside within the red giant atmosphere of the primary
double common envelope	the presumed requirement for the birth of a He CV, in which both stellar components must evolve beyond main sequence burning.

1.1.2 CV synthesis

Prior to the birth of a CV, two main sequence stars are gravitationally bound but otherwise non-interacting. The more massive star – the component that is destined to become the primary – evolves faster to the red giant phase, fills its Roche lobe, and transfers matter to its less-massive companion. Since the primary is closer to the system's center of mass, this mass transfer is unstable: the orbital separation decreases to conserve overall angular momentum, thereby increasing the rate of mass transfer, and the result is a catastrophic runaway event in which the entire atmosphere of the red giant is deposited upon the secondary in < 10 years. The secondary cannot assimilate this matter as quickly as it acquires it, and the matter forms a cloud, or "common envelope" (CE), around the stars.

As the orbit propels the CE away, the CE imparts a resistance that drains angular momentum and reduces the orbital separation from ~ 10^3 to 1 solar radius in ~ 10^3 years. If the separation has sufficiently decreased in size by the end of the CE phase, the secondary now fills its Roche lobe. Long-term continuous mass transfer begins in the opposite direction, and the system is now a CV. For details on CV synthesis and subsequent evolution, see Knigge (2011). For an historical review, see Warner (1995).

Two topics merit a mention before we proceed with a detailed examination of the physics governing CVs.

No angular momentum conservation?

There exists a fatal problem with the model of a CV as it has been delineated thus far: if the system conserves angular momentum, then long-term continuous mass transfer from the secondary is precluded. Conservation of angular momentum dictates that as mass flows from a lower-mass to higher-mass component, the orbital separation must increase. Consequently, the secondary should soon (in ~ 10^2 years) detach from its Roche lobe and accretion should stop. This is not observed to occur. Continuous mass transfer appears to be occurring for at least 10^8 years. To rescue the model, we postulate that there exists an angular momentum drain on these systems. Two likely candidate mechanisms for angular momentum loss will be examined in §1.2.6.3.

“Ultra-compact” CVs

In the first two decades following the discovery of compact accreting binaries, all known members of the class had orbital periods greater than a few hours and hydrogen-rich spectra. Then, in the early 1970’s, a few objects with periodicities significantly shorter than an hour were identified as CVs with rapid orbital periods. Spectroscopically, they are hydrogen-deficient and helium-rich (He/H ~ $10^{3\text{-}4}$ by number). These data imply compact secondaries that have evolved beyond hydrogen burning and are on their way to becoming degenerate white dwarfs themselves. These are the *helium* CVs, or “He CVs”, or “AM CVn stars” after the first identified member of the class.

For He CVs, the basic model remains the same. Key differences are:

- short P_{orb} implies a smaller geometric scale;
- a secondary that has evolved beyond the main sequence implies a different evolutionary history and future;
- rapid rotation and compact secondary predict that He CVs should be strong emitters of gravitational wave radiation;
- small sample size of 26 objects leaves important questions unresolved.

Section 1.2 will focus on hydrogen CVs, as their model is more fully developed than, and provides the basis for, an understanding of their helium-rich counterparts. We will examine the helium CVs in §1.3.

1.1.3 In this dissertation

The studies presented in this dissertation comprise two areas:

- Probing the nature of He CVs, using superhump and orbital signal detections (Chapters 3 and 4), and direct pulse timings of P_{orb} (Chapter 5);

- Examining evidence for tilted accretion discs in CVs (Chapters 6 and 7).

The first goal involves characterizing the evolution of the relatively poorly-understood He CVs in terms of orbital period change, in order to infer the nature of the secondaries, likely paths to creation of the systems, and their likely futures. The second goal addresses the "tilted-disc" model, which was developed for low-mass X-ray binaries with neutron star accretors and is a problematic model when applied to CVs.

The remainder of this introduction presents foundations of CV theory, in order to provide the reader with a context for the studies to be discussed.

1.2 Hydrogen CVs

1.2.1 Variability on multiple timescales

CVs display variability on timescales of seconds to years. Some modulations persist at stable periods for decades, while others are quasi-periodic, intermittent, or transient. A given periodic modulation tends to exhibit a consistent degree of coherence, which– over all signals in all systems – can range from one part in 10^3 to one part in 10^8 (in terms of variation in period value). Fig. 1.2 shows light curves of six variable stars (Hellier 2001). The figure is intended to illustrate the variation in behavior among CVs and the importance of conducting long-term monitoring in order to study them. Magnitudes correspond roughly (± 0.3 mag) to V light, and the timescale of each observation is denoted in the bottom right corner of each frame.

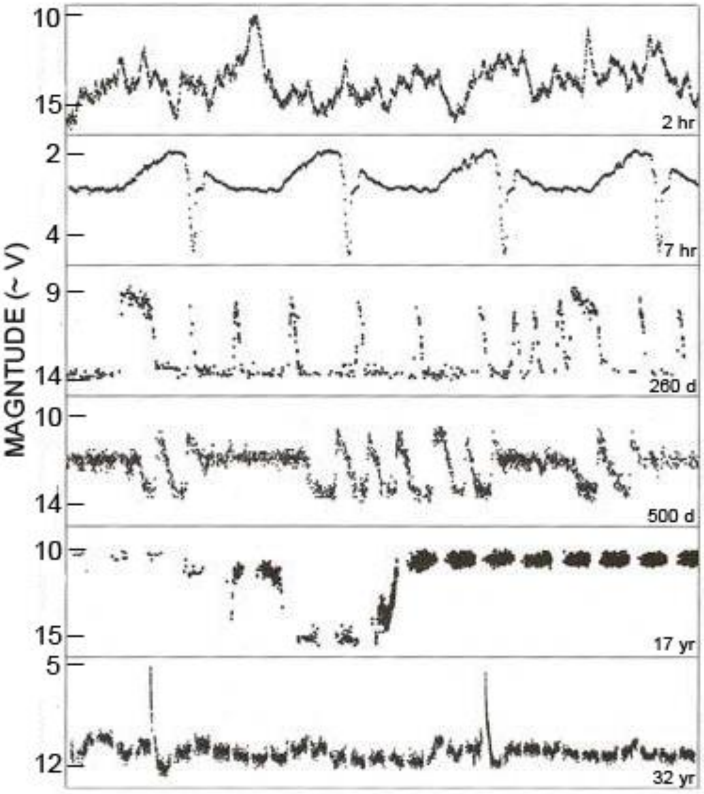

Fig. 1.2: Light curves of 6 variable stars. *From top*: RX Andromedae, IY Ursa Majoris, VW Hydri, Z Camelopardalis, TT Arietis, RS Ophiuchi. Magnitudes correspond roughly to V light. Timescale is noted at bottom right of each frame. *Adapted from Hellier (2001*).

1.2.2 The orbital period

The fundamental clock in a CV is its orbital period. P_{orb} is most easily identifiable in eclipsing CVs, where the eclipse modulation is attributed to the periodic occultation of the disc by the secondary. Fig. 1.3 shows one orbital cycle in the light curve of SDSS 154453+2553, with a deep eclipse occurring every ~ 4.1 hours. If eclipses are not present, P_{orb} can usually be identified as optical modulation due to the “bright spot”: the location at which infalling matter hits the outer region of the disc[1].

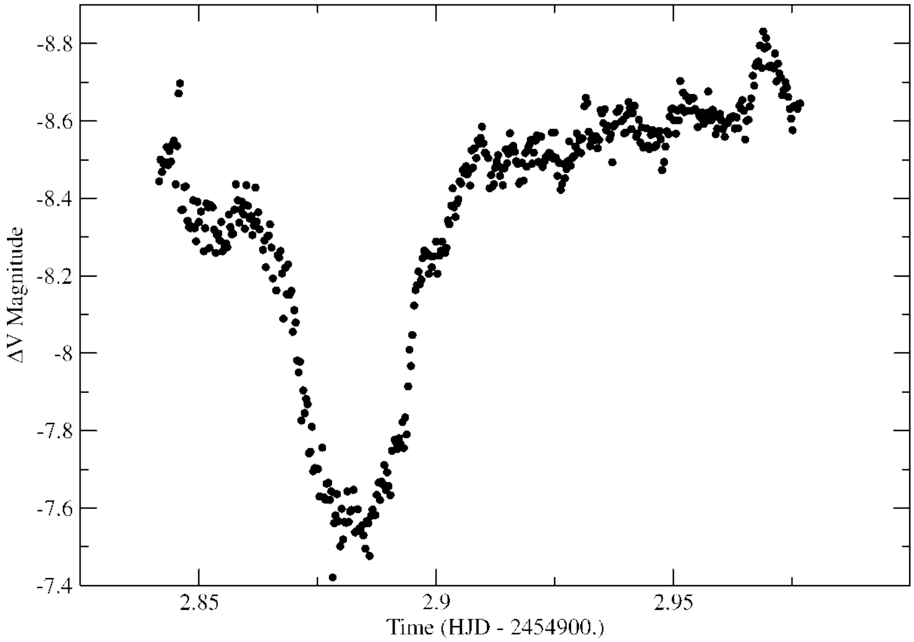

Fig. 1.3: One orbital cycle in the light curve of the CV SDSS 154453+2553 obtained in V light (reproduced from Skinner et al. (2011). A deep eclipse of ~ 0.1 mag occurs every ~ 4.1 hours, and constitutes an unambiguous P_{orb} determination.

Orbital periods in hydrogen CVs range from ~ 1 to 12 hours. The strength of their modulations relative to the total brightness varies among CVs and is highly dependent on eruptive behavior (§1.2.3). Orbital period measurements constrain the size, geometry, and evolutionary history of a CV.

In particular, if the orbital period change serves as a proxy for the long-term (secular) evolution of a CV, then direct pulse timings of orbital signals in individual CVs can be extremely valuable characterizations of these systems. Specifically: What was their path to

---

[1] The bright spot does not necessarily impact the disc in a consistent location throughout an orbit. In systems with discs that are tilted with respect to the orbital plane (see Chapter 7), the bright spot does not impact the disc edge-on, but rather spills over one face. Such variation should not affect the timing of an orbital period that is based on the bright spot modulation. To time the modulation, one folds the light curve over many periods, which will average out any variation over each orbit.

creation, what is their likely future, and what can we learn about the nature of matter comprising the secondary star? This will be the topic of Chapters 4 and 5.

1.2.3 Outburst behavior

Eruptions are hallmarks of CVs and can be divided into two general classes: those due to instabilities within the disc ("dwarf nova" outbursts and superoutbursts), and those due to encounters of matter with the white dwarf surface ("recurrent novae" and "classical novae"). It is the former of these two mechanisms that pertains to the studies comprising this thesis. The terms listed in Table 1.2 will be used frequently in discussions of eruptive CVs.

Table 1.2: Terminology describing eruptive behavior in CVs.

Term	*Definition*
Dwarf nova outburst; normal outburst	A sudden brightening of a CV by ~ 2-8 mag, which tends to recur periodically; attributed to a cyclic thermal instability in the disc
Dwarf nova superoutburst	A slightly greater brightening that tends to recur on several times the normal outburst timescale; attributed to a tidal instability caused by the secondary's torque upon the disc
High state; bright state; hot state	A state of high luminosity that is attributed to a high rate of mass accretion and a hot disc (T ~ 30,000 K)
Low state; quiescence	A state of low luminosity that is attributed to a low rate of mass accretion and a cool disc (T ~ 5,000 K)
Positive superhump	The modulation in a CV light curve with a period slightly longer than P_{orb}, which corresponds to a negative orbital sideband in the power spectrum; linked to outburst behavior

Dwarf nova outbursts

Dwarf nova outbursts are brightenings by ~ 5 mag that occur within about a day, and are followed by a gradual return to quiescence over days to weeks. Typically this behavior occurs on a cycle of weeks to months. Fig. 1.4 shows a dwarf nova eruption in OY Carinae (Rutten et al. 1992), in which deep eclipses define P_{orb}.

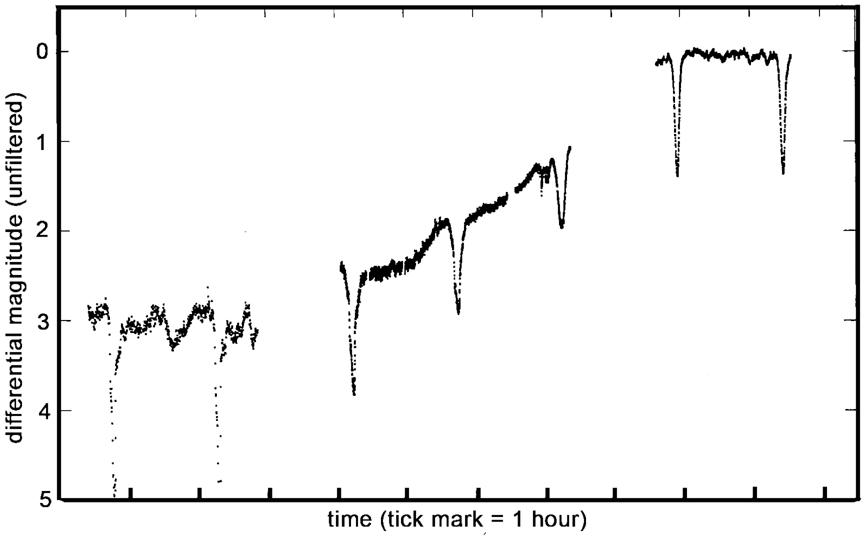

Fig. 1.4: Light curve of differential magnitude, showing a dwarf nova eruption in the cataclysmic variable OY Carinae, in white (unfiltered) light (Rutten et al. 1992). From left to right, the system is observed in quiescence, during rise to outburst, and at outburst maximum. The deep features are eclipses on the orbital cycle.

Dwarf nova outbursts are attributed to a thermal-viscous instability in the accretion disc (Osaki 1974), which is essentially due to the fact that the rate of mass transfer from the secondary ($\dot{M}_2$) to the outer disc exceeds the rate at which the matter can then be transported through the disc to onto the WD. Consequently matter builds up within the disc until a critical viscosity is reached, at which point a large amount of matter is deposited onto the WD. The gravitational potential energy lost in the WD's well causes the observed brightening. In detail, the cycle goes as follows.

We begin in quiescence, with a cold (T ~ 5000 K) disc comprised of neutral atoms. As the secondary surrenders its matter, the disc's density increases, matter becomes optically thick, and the temperature rises to ~ 10,000 K, at which point the matter is partially ionized. The onset of ionization causes the opacity and temperature to climb rapidly (to ~ 30,000 K), at which point a critical viscosity is reached and a large amount of mass is deposited onto the white dwarf. At the same time, to conserve overall angular momentum in the disc, some of the matter spreads farther outward– hence the disc grows in radius as it heats. After outburst, the disc, now depleted of matter, decreases in temperature and returns to quiescence.

The disc is gradually replenished with mass from the secondary, which begins orbiting at the "circularization radius" (R_{circ}), set by Kepler's third law. Because the disc has spread outward during the previous accumulation of matter, the outer disc radius (R_{outer}) is now larger than R_{circ}. As a result, during quiescence, as new matter is acquired in the disc, the disc shrinks to near its original value. The cycle repeats[2].

Evidence for a disc governed by a thermal instability

The signatures that various components of a CV impart upon a light curve will be outlined in Chapter 2. One signature merits a mention now because it constitutes strong evidence in favor of Osaki's thermal cycle model: absorption and emission lines. Well-resolved spectral lines generally appear in emission during quiescence and absorption in outburst. This observation can be understood as follows.

When the disc is hot, it is optically thick: a photon cannot travel far between interactions with other particles. Thus the observed line photons must have emerged from near the disc surface. The continuum, which emerges from more deeply within the disc, is hotter – and brighter than the lines. Hence the lines will appear in absorption. In a quiescent disc, opacity is low and essentially all light escapes unscathed; hence the lines will appear in emission.

---

[2] Doubt remains regarding whether a disc instability alone can reproduce the observed change in flux of a CV experiencing a dwarf nova outburst. An additional source of enhanced mass transfer might be required. A viable candidate is increased irradiation of the secondary (Vogt 1983), which is probably responsible for some features of a CV light curve, particularly increased amplitudes of various signals during outbursts (Smak 1991), and might also play a role in maintaining disc tilt (Chapter 7). Currently, the role of irradiation during dwarf nova outbursts is unclear.

Dwarf novae superoutburst cycles

In some CVs, a series of dwarf novae eruptions is punctuated by superoutbursts. Superoutbursts are typically a few magnitudes brighter than the "normal" outbursts just discussed, rise roughly as rapidly, and are followed by a more gradual decline to quiescence.

About a day after the system's rise to maximum light in superoutburst, a modulation called "positive superhumps" usually appear. Their appearance in the light curve has earned them this nickname: a large-amplitude (~ 0.4 mag) "sawtooth" fluctuation that dominates all other modulations. They are denoted as "positive" because their period (P_{SH+}) is 2 – 5% longer than the orbital period in a given system. Superoutbursts occur on timescales of months to years, and positive superhumps tend to appear and disappear on that cycle, fading in the weeks to months that follow each eruption.

The top panel of Fig. 1.5 shows a ~ 78-day light curve following the superoutburst of WZ Sagittae (Knigge et al. 2002), in which positive superhumps appeared around day #10 after maximum light (bottom panel; Patterson et al. 2002). Note the different x-axes between the top and bottom panel. Superhumps are not visible in the full light curve because each point represents a mean over one superhump period. (The series of visible re-brightenings during days ~ 29-53 are "echo outbursts", not to be confused with superhumps. Echo outbursts, which are occasionally observed during a CV's fall from superoutburst, will not be explored in this dissertation).

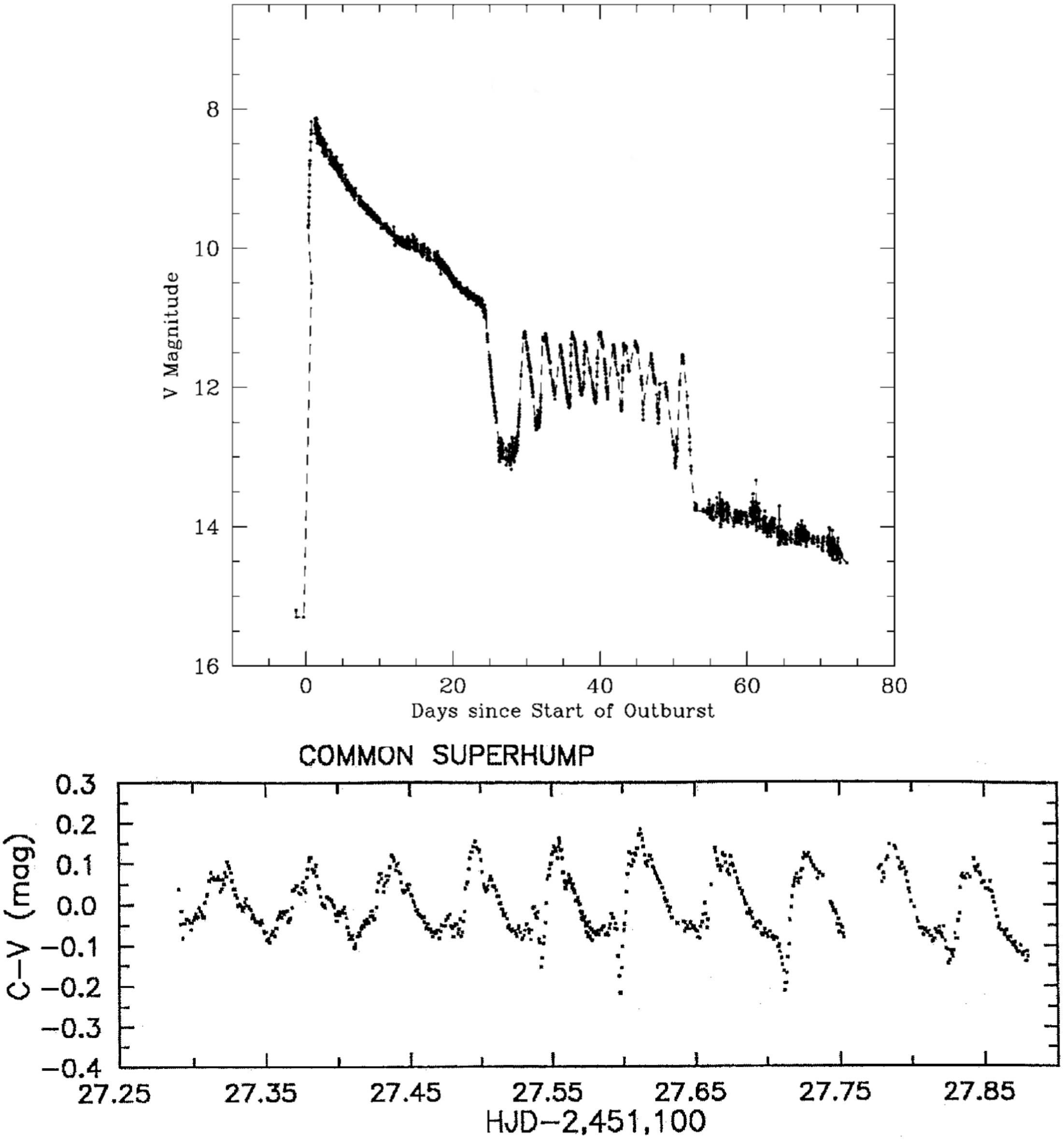

Fig. 1.5: *Top panel*: VSNET V-mag light curve of WZ Sagittae during its 78-day decline from superoutburst (modified from Knigge et al. (2002)). A gradual decline in brightness by ~ 7.5 magnitudes is punctuated by shorter "echo outbursts" during days ~ 30-48. (Echo outbursts are not discussed in this dissertation and should not be confused with superhumps). Superhump modulations begin to dominate the light curve on day #10, as is indicated on the figure, but are not visible to the eye in this light curve because points are averaged over one superhump period. *Bottom panel*: A closer inspection of the light curve, also in V light, during day 10, in which the superhump modulation dominates (Patterson et al. 2002).

Osaki (1989) proposed that the superoutburst cycle – and positive superhumps – can be understood as a combination of the thermal/viscous instability and a tidal instability due to the perturbing effect of the secondary upon the disc. As noted above, during quiescence between outbursts, R_{outer} decreases as infalling matter attempts to match the Keplerian velocity at R_{circ}. By the time the next outburst is triggered, the disc has not necessarily had sufficient time to return to its original size. Rather, over a series of outbursts, R_{outer} gradually grows. Eventually, an outburst pushes R_{outer} to a size at which it is unstable to the tidal effect of the secondary. The disc then grows eccentric. If the orbits of matter in the outer disc resonate with the secondary orbit, then the disc eccentricity can grow to the point at which the disc's line of apsides precesses in a prograde direction with respect to the orbit. This probably occurs at the 3:1 resonance[3]. The orbits of material in the outer disc, no longer parallel, collide. The resulting dissipated energy causes the positive superhump modulation. Tidal stresses greatly enhance angular momentum drain on the disc, enhancing the inward flow of matter, which sustains the disc in the hot state.

Now, we can relate the periods of orbit, apsidal precession, and positive superhump as follows:

$$\frac{1}{P_{SH+}} = \frac{1}{P_{orb}} - \frac{1}{P_{prec}} \qquad 1.1$$

where P_{prec} is the period of prograde apsidal precession. In this context, P_{SH+} corresponds to a beat between orbital and precession motions. This relation will be valuable for charting the

---

[3] The gravity of the secondary will drive the disc eccentricity only if its periodic pull resonates with the radial motion within the disc. In this case, it can enhance the radial component of the disc motion, driving the outer material into eccentric orbits. Disc matter cannot resonate directly with the secondary because the Keplerian orbit at R_{outer} is faster than the secondary's orbit (see §1.2.6.2). The 2:1 resonance is also ruled out because the radius of orbits would be larger than the white dwarf's Roche lobe for CVs with mass ratio < ~ 0.025. The 3:1 resonance is accessible for systems with mass ratio < ~ 0.3. Observationally, in systems that display superoutbursts, mass ratio is less than 0.33 (e.g. Hellier 2001).

distribution of P_{orb} in time, for CVs as a group (chapters 3 and 4).

Using Osaki's model, numerical simulations can reproduce the observed superhump modulations of superoutburst light curves (Whitehurst 1988). A similar model to explain superhumps in low-mass X-ray binaries (LMXBs) has been worked out by Larwood (1998). For a thorough treatment of accretion disc physics, see Pringle (1981). For a review of superoutburst observations, see Patterson (1999). For a detailed observational study of superhump evolution during decline from superoutburst, see Patterson et al. (1995).

1.2.4 Signals associated with discs and tilted-disc geometry

Some CV light curves display "superorbital periods", which technically are modulations with periods longer than P_{orb}. In this dissertation, "superorbital periods" will refer to a class that are roughly an order of magnitude longer than orbital periods in CVs, and are associated with one of two types of precession of the accretion disc: 1) "apsidal" or prograde precession of the line of apsides of an eccentric disc – which was discussed above; 2) "nodal" or retrograde precession of the line of nodes of a disc that has tilted out of the orbital plane, possibly due to wind and/or irradiation torques. The model for apsidal precession was discussed previously and is consistent with observations. The second (nodal) type of precession is relatively problematic for CVs. The model of a tilted accretion disc was developed for X-ray binaries (XBs), in which irradiation by a primary neutron star can effect the disc tilt. (Pringle 1996, Wijers & Pringle 1999, Maloney & Begelman 1997). A primary white dwarf, however, is probably insufficient to incite tilt (e.g. Petterson 1977), and a viable alternative mechanism has not been satisfactorily identified. Prior to the studies discussed in Chapter 7, the amount of observational evidence for tilt in CVs was unclear.

In some CVs, superorbital modulations are accompanied by *negative* superhumps: signals that, by analogy with the positive superhumps, show periods (P_{SH-}) slightly shorter than the orbital period in a given system, such that the following equation is satisfied:

$$\frac{1}{P_{SH-}} = \frac{1}{P_{orb}} + \frac{1}{P_{prec}} \qquad 1.2$$

where P_{prec} now refers to a period of *retrograde* nodal disc precession. In this context, the negative superhump is a beat between the orbital and retrograde precession motions. The modulation at the superorbital period is attributed to varying surface area of the disc that is presented to the observer. The modulation at the negative superhump period is attributed to varying depth of the stream-disc impact point in the potential well of the primary.

We will examine evidence for tilted discs in CVs in Chapters 6 and 7.

1.2.5 Other signals in CVs

Other signals commonly detected in CVs include 1) “flickering” – a prominent and poorly understood feature of all CV light curves; 2) a highly coherent, fast periodicity interpreted as the spin of the primary; 3) “rapid oscillations” –a class of signals associated with strong magnetism; 4) recurrent and classical novae – associated with thermonuclear explosions on the WD surface. These observations are important to our understanding of CVs, but they do not directly relate to the studies comprising this thesis. For a summary, see Appendix A.

1.2.6 CVs in terms of basic physics

1.2.6.1 Energy considerations

We can reproduce the observed flux from a CV by invoking mass transfer and radiated gravitational potential energy during infall toward a WD. The rate of gravitational potential energy loss due to mass accretion $\dot{M}$ within the well of a black body sphere of mass M_1 is:

$$\frac{dE}{dt} = -\frac{GM_1\dot{M}}{r} \qquad 1.3$$

where r is the distance from the center of mass of M_1. We approximate the WD as a black body and use the following approximation for its luminosity:

$$L_{bb} = \sigma 4\pi R^2 T^4 \qquad 1.4$$

Chandrasekhar (1939). Then, from observed magnitudes, temperatures inferred spectroscopically, and estimates of the sizes of the stellar components derived from eclipse mapping, we infer mass accretion rates ($\dot{M}$) of 10^{-8-10} $M_{\odot}$ yr^{-1}, depending on orbital period. It is reasonable to expect that such rates can be sustained over the long term without resulting in detonations on the white dwarf surface (Iben et al. 1992). For details of these calculations, see Appendix B.

1.2.6.2 Roche geometry

We can infer the geometry and size of a CV as a function of mass ratio q (where q = $\frac{M_2}{M_1}$), density of the secondary ρ_2, and P_{orb}, via considerations of Roche geometry and Newtonian physics.

Fig. 1.6 shows the Roche geometry surrounding two stars with q = 2, where each contour represents a line of equal depth within a gravitational potential well. If the secondary fills its Roche Lobe, matter will flow onto the primary through the inner LaGrangian Point L_1 (e.g. Paczynski 1971).

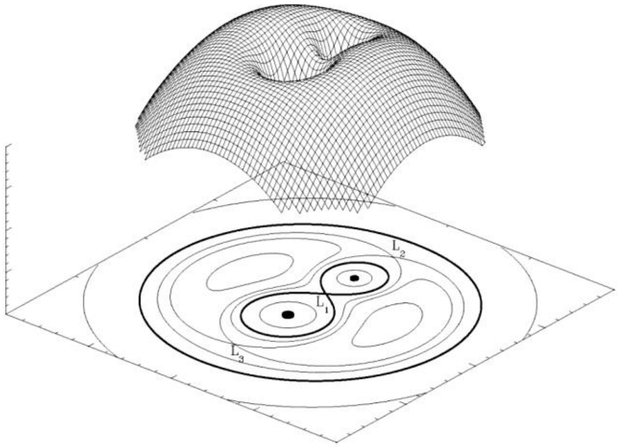

Fig. 1.6: The Roche potentials – lines of equal gravitational potential – surrounding a binary system with mass ratio 2. Mass transfer occurs via the inner Lagrangian point L_1. The topological map shows the gravitational wells of the two masses: their imprint upon the space-time in which they are embedded (http://hemel.waarnemen.com/Informatie/Sterren/hoofdstuk6.html#mtr).

Matter accreting from the secondary has too much angular momentum to fall directly onto the primary (several hundred km s^{-1}), and instead forms a circular orbit with a "Keplerian" velocity of

$$v_k = \sqrt{\left(\frac{GM_1}{R_{circ}}\right)} = \frac{2\pi R_{L1}}{P_{orb}} \tag*{1.5}$$

where R_{L1} is the distance between the inner Lagrangian point and center of the WD. Then:

$$R_{circ} = \frac{4\pi^2 R_{L1}^4}{GM_1 P_{orb}^2} = (1+q)\frac{R_{L1}^4}{a^3} \tag*{1.6}$$

The radius of the secondary, R_2, is approximately the radius of its Roche lobe volume, which depends only on q and the separation between the centers of the stellar components "a." For $0.1 < q < 0.8$, the range for most CVs, this relation can be approximated as:

$$\frac{R_2}{a} \sim 0.46\left(\frac{q}{1+q}\right)^{1/3} \tag*{1.7}$$

(Paczynski 1971). Taking that with Newton's version of Kepler's third law:

$$P^2 = \frac{4\pi^2 a^3}{G(M_1 + M_2)} \qquad 1.8$$

we obtain the period-density relation for Roche-lobe-filling stars:

$$\overline{\rho_2} = \frac{3M_2}{4\pi R_2^3} \sim \frac{95}{G}\frac{1}{P_{orb}} \qquad 1.9$$

From the chemical compositions inferred spectroscopically and the density inferred from Roche geometry, we can approximate the secondary as a main sequence star (e.g. Patterson 1984). This gives $\frac{M_2}{M_{sun}} \sim \frac{R_2}{R_{sun}}$, and mass and radius of secondary are set by P_{orb} alone:

$$\frac{M_2}{M_{sun}} \sim \frac{R_2}{R_{sun}} \sim 0.1 P_{orb}\ [hr] \qquad 1.10$$

From Newton and Kepler's laws, we can also infer the geometric size of a CV:

$$a = 3.53 \times 10^{10} M_1 (1+q)^{1/3} P_{orb}^{2/3}(hr)\ cm \qquad 1.11$$

If M_1 and M_2 are each ~ $0.5M_{sun}$ and $1 < P_{orb} < 12$ hours, the range for most CVs, then a ~ 0.5 – $3R_{sun}$. For a detailed model of the geometry of contact binaries, see Shu et al. (1976) and Lubow & Shu (1977).

1.2.6.3 Angular momentum considerations

The angular momentum of the accretion stream forces the matter into a ring around the WD, but it is clear that the matter does not remain in a ring. Due to viscous interactions that are not well understood, some matter spirals inward toward the WD. To conserve overall angular momentum in the disc, some of the material simultaneously spreads outward to larger radius; hence the matter's long-term configuration is a disc (Pringle 1981). The *overall* angular momentum *of the binary*, however, is evidently not conserved. If it were, continuous mass transfer would be precluded (for evidence that continuous mass accretion is indeed occurring on timescales of at least 10^8 years, see Appendix C). Here is how we reach this conclusion.

The angular momentum of a binary is:

$$J_{binary} = M_1 a_1 \frac{2\pi a_1}{P_{orb}} + M_2 a_2 \frac{2\pi a_2}{P_{orb}} \qquad 1.12$$

and $a_1M_1 = a_2M_2$. We define: $a \equiv a_1+a_2$, and $M \equiv M_1+M_2$, and combining Eq. 1.12 with Kepler's third law (Eq. 1.8), we obtain:

$$J = M_1 M_2 \left(\frac{Ga}{M}\right)^{1/2} \qquad 1.13$$

and:

$$\frac{\dot{J}}{J} = \frac{\dot{M}_2}{M_2}(1-q) + \frac{\dot{a}}{2a} \qquad 1.14$$

So if $\dot{J} = 0$, then for the values of q typical of CVs, mass loss from the secondary would require that $\dot{a}$ be positive: the Roche lobe would expand upon mass loss and $\dot{M}$ would quickly approach zero. Thus, for continuous mass transfer, we need $\dot{J} < 0$.

What could cause continuous angular momentum drain on a CV? A clue can be found in the distribution of orbital periods, shown in Fig. 1.7; namely: the "period gap" between ~ 2 and 3 hours. Most CVs lie either above or below this region, and this observation that can be explained by invoking two mechanisms for angular momentum loss in CVs. The first is magnetic braking, a scenario in which material is driven from the CV in a wind via the magnetic field of the secondary. The second mechanism is gravitational wave radiation, which will be discussed within the context of helium CVs.

In long-period CVs, magnetic braking is believed to dominate evolution. As the secondary evolves, its magnetic field weakens, and it is thought that magnetic braking essentially turns off for systems when $M_2 \sim 0.3M_{\odot}$ - which corresponds to a P_{orb} of ~ 3 hrs[4]. Meanwhile, gravitational wave radiation (GWR) strengthens as P_{orb} shortens, and should dominate evolution for the shorter-period CVs.

Within this picture, we can interpret the period gap as follows. As the secondary evolves below $0.3M_{\odot}$, the efficiency of magnetic braking decreases rapidly. Meanwhile, GWR is not yet sufficiently strong to keep the secondary in contact with its Roche lobe.

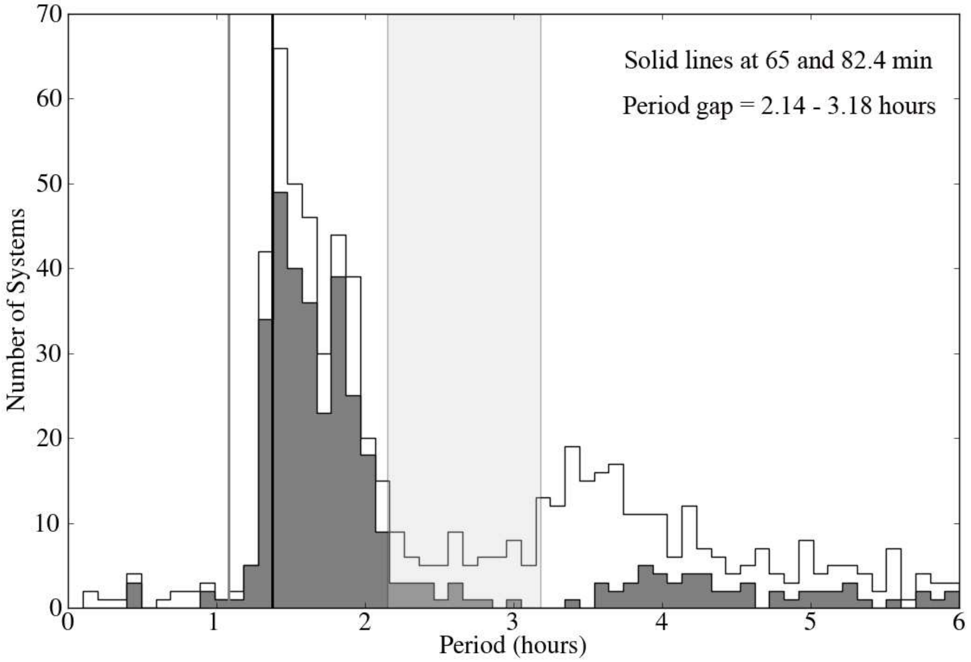

Fig. 1.7: The distribution of CVs according to orbital period (Ritter & Kolb version 7.14 (2010). The white region includes all non-magnetic CVs; the dark grey region represents CVs that experience dwarf nova explosions. The lightly-shaded rectangular area indicates the observed period gap between 2.14 – 3.18 hours. The light grey line represents the theoretical period minimum of 65 minutes (Kolb 1993); the black line represents the observed period minimum of 82 minutes (Gänsicke et al. 2009).

---

[4] Magnetic braking is believed to weaken due to the increasing size of the secondary's convective zone: as the secondary loses mass, its outer convective region expands, reaching an increasingly deeper level within the star (Schwarzschild 1958). For details, see Spruit & Ritter 1983; Rappaport et al. 1983. GWR is not yet sufficiently strong to keep the secondary in contact with its Roche lobe.

Hence the secondary detaches from its Roche lobe, mass transfer ceases, and the binary becomes too faint to observe. The binary separation continues to shrink, however, due to the effect of GWR – which is strengthening. Once the system reaches a P_{orb} of ~ 2 hours, GWR losses are sufficient to re-establish the secondary's connection to its Roche lobe. Mass transfer recommences and we see the system reappear at P_{orb} ~ 2 hours. For details, see Kolb (1993) and Knigge (2011).

Two other notable features of the period distribution are: a period maximum of ~ 12 hours and a period minimum of ~ 80 minutes. For a summary explanation, see Appendix D.

1.2.7 Evidence for period evolution

What is the long-term evolution of CVs? For clues, we can look to the following relations.

1.2.7.1 The M_2-P_{orb} relation

Fig. 1.8 shows a plot of M_2 versus P_{orb} for hydrogen CVs, where M_2 values were obtained independently of P_{orb}, either from eclipse data or superhump periods (see Chapter 4). For most CVs, M_2 and P_{orb} decrease roughly linearly, implying $\dot{P} \sim 10^{-11-13}$ (for $\dot{M}_2 \sim 10^{-8-10} M_\odot\ yr^{-1}$). Since decreasing M_2 points the direction of evolution, we infer that most H CVs are evolving toward shorter P_{orb}[5]. There exists mild evidence that this trend reverses around P = 80 minutes.

---

[5] The range of secondary masses shown in Fig. 1.8 (0.04-$0.6 M_\odot$) is at least an order of magnitude broader than the range of initial secondary masses at the onset of long-term mass transfer.

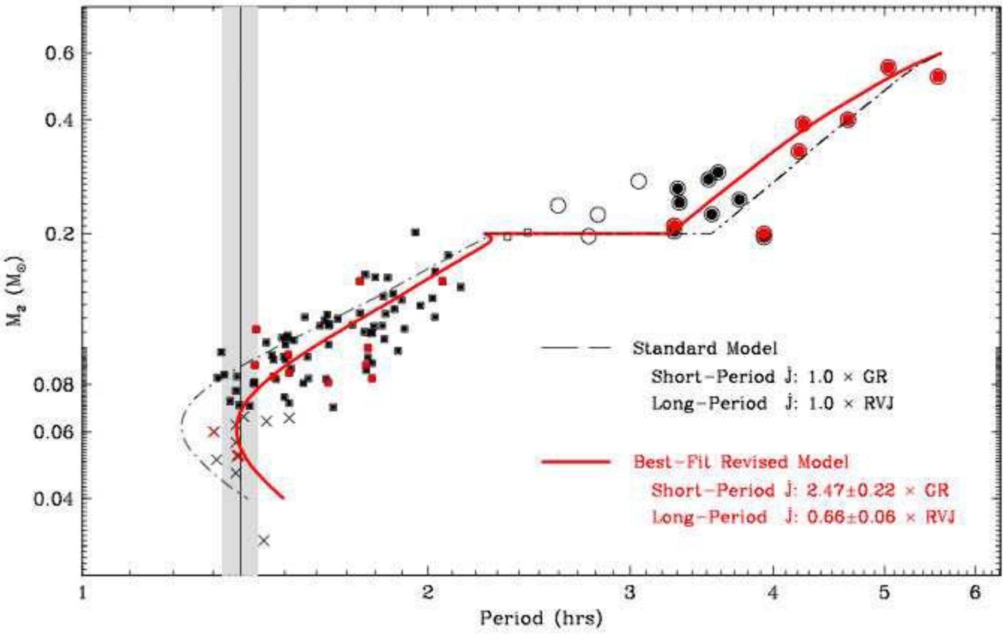

Fig. 1.8: The M_2-P_{orb} relation for H CVs (Knigge et al. 2011). The individual symbols represent observations; a red symbol indicates a mass determined from eclipse data; black indicates a mass determined via a positive superhump period. Observations indicate that M_2 decreases as P_{orb} shortens, and there is weak evidence of a "turnaround period" around 80 minutes. The lines are models, which predict that after a minimum P_{orb} is reached, the direction of P_{orb} will reverse upon further mass loss from a degenerate secondary.

1.2.7.2 The ε-P_{orb} relation

The ε-P_{orb} relation is another indicator of P_{orb} evolution (Patterson et al. 2005), and is consistent with the M_2-P_{orb} finding. The motivation is as follows.

We seek a reliable proxy for time in CVs. As a CV evolves, q decreases (the secondary loses mass). So a "q distribution" would point in the direction of evolution. But q is only directly measurable via eclipsers, and most CVs do not eclipse. We can still exploit the decreasing mass of the secondary, however, if we look to CVs that show positive superhumps. As M_2 decreases, the secondary's pull on an elliptical disc will decrease. Hence the precession rate should slow, and the corresponding beat period (P_{SH+}) should increase. We define the "fractional superhump period excess" ε:

$$\varepsilon = \frac{P_{SH+} - P_{orb}}{P_{orb}} \tag{1.15}$$

Observations of hundreds of eclipsing H CVs indicate that ε is a valid proxy for q:

$$\varepsilon = 0.18\mathrm{q} + 0.29q^2 \tag{1.16}$$

(Patterson et al. 2005). Most critically: *ε is directly measurable.*

Fig 1.9 shows the $\varepsilon(P_{orb})$ distribution for H CVs, which resembles the distribution of the M_2-P_{orb} diagram of Fig. 1.8. (The points lie below the model line for zero-age main sequence (ZAMS) stars, because such stars in binaries are systematically larger at a given mass, due to the process of mass transfer). Since the mechanism driving period evolution is essentially the same regardless of the presence of superhumps, it is probable that this relation applies to all CVs. Our application of this technique to *helium* CVs will be the topic of Chapter 4.

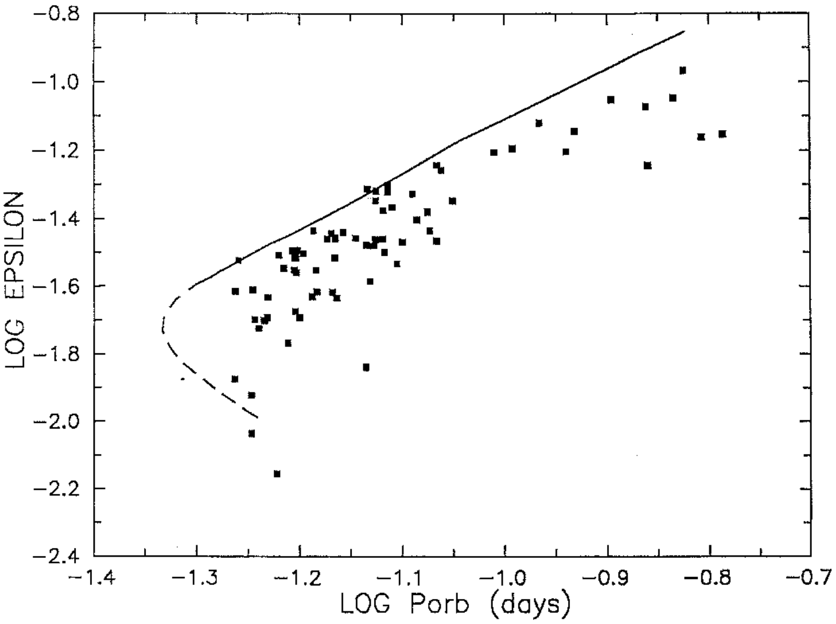

Fig. 1.9: The $\varepsilon(P_{orb})$ relation for hydrogen CVs that display positive superhumps (Patterson et al. 2003). The solid line is the prediction of a model in which the secondary is a "zero-age main sequence star": a star that can be approximated as a non-degenerate main sequence star of solar radius. The dashed line traces the predicted trajectory of CVs with secondaries evolving toward degenerate states and with angular momentum loss governed by GWR.

1.2.8 Related areas

Other important studies of hydrogen CVs include ages, space density, and population synthesis calculations. As these areas do not pertain directly to the studies comprising this thesis, a summary has been placed in Appendix E.

1.2.9 Hydrogen CVs in this dissertation

Studies related to hydrogen CVs will be discussed in Chapters 4 and 7, as follows:

- Chapter 4: an update of the ε(q) relation, which was developed using hydrogen CVs, to study evolutionary history in helium CVs;
- Chapter 7: studies of superorbital periods in H CVs and investigation the viability of the tilted-disc model for accreting binaries with WD primaries.

1.3 Helium CVs

1.3.1 Summary

He CVs are defined by the following criteria:

- Spectra showing strong He lines and essentially no H (He/H by number ~ 10^3-10^4);
- Colors slightly bluer than those of H CVs, appearing faintly in the ultra-violet;
- Periodicities – with stabilities typical of orbital periods – shorter than ~ 70 minutes;
- Signatures of mass transfer, outbursts, and accretion discs analogous to observations in H CVs.

The higher temperatures, orbital speeds, and chemical compositions implicate a CV with a compact geometry, in which the secondary has evolved beyond main-sequence burning.

The first helium CV identified was AM Canum Venaticorum (AM CVn) (e.g. Smak 1967; Patterson & Sterner 1992), which had been discovered by Malmquist (1936). Landau &

Lifshitz (1951) and Kraft et al. (1962) had already suggested that a sufficiently compact binary might present a laboratory in which to examine the effects of GWR. Paczynski (1967) worked out the model for binaries of various mass ratios, and concluded that for systems with sufficiently short orbital periods, GWR can drive their evolution and provide the angular momentum drain required for continuous mass transfer. The basic model of a He CV was worked out by Faulkner (1971) and Faulkner & Flannery (1972). The thermal/tidal instability model for outburst cycles was modified for helium CVs by Tsugawa and Osaki (1997).

Since 1996, the number of known He CVs has increased from 6 to 26 (at least 4 of which are considered candidates), largely from searches for blue objects and the characteristic He-rich and H-deficient spectrum. Many recent discoveries have come from searches of the Sloan Digital Sky Survey's (SDSS) public database, which includes spectra of 240,000 stars (http://www.sdss.org/dr3/products/spectra/index.html).

Due in large part to the small sample size, He CVs are not as well understood as their hydrogen-rich counterparts. Important components of the model are discussed below[6].

1.3.2 Gravitational wave radiation

Earlier we discussed the relationship between angular momentum drain and rate of decrease in orbital separation "a" for a contact binary (Eq 1.16). Substituting P for a via Kepler's law (Eq. 1.8), we obtain:

$$\frac{\dot{P}_{orb}}{P_{orb}} = 3\left[\frac{\dot{J}}{J} - \frac{\dot{M}_2}{M_2}(1-q)\right] \tag{1.17}$$

---

[6] For the reader interested in details beyond the scope of this dissertation: an overview of "ultra-compact binaries", a classification that includes He CVs and XBs, can be found in Nelemans (2009). In addition, any of that author's numerous theoretical and observational publications on He CVs – dating to ~ 2000 – are clear and well-written. Finally, a comprehensive review of He CVs, including observations, simulations, theory, and notes on individual systems, was compiled by Solheim (2010).

where the mass-radius relation of the secondary is contained in the $\frac{\dot{M}_2}{M_2}$ term. The right side of Eq. 1.17 can be regarded as a tug-of-war contest, in which the $\frac{\dot{J}}{J}$ term tends to shorten P_{orb}, while the $\frac{\dot{M}_2}{M_2}(1-q)$ term (which describes the secondary's response to mass loss) will begin to lengthen P_{orb} as a significant fraction of the secondary's matter settles into a degenerate state (supported increasingly by eleectron degeneracy pressure rather than thermal motions). Mass loss will lift degeneracy pressure, and hence a degenerate object will increase in radius as it loses mass. This relation will be explored within the context of AM CVn's orbital period evolution (Chapter 5).

Now, General Relativity gives the following relation for angular momentum drain due to GWR ($\dot{J}_{GR}$):

$$\frac{\dot{J}_{GR}}{J_{orb}} = -\frac{32}{5}\frac{G^3}{c^5}\frac{M_1 M_2 \dot{M}}{a^4} \qquad 1.18$$

(Landau & Lifshitz 1951). The rate of orbital period change due to GWR for binaries of varying orbital period was worked out by Paczynski (1967). Using typical P_{orb} and mass ratios of He CVs, Warner (1995) showed that these objects should be the strongest GWR emission line sources in the 0.7-2.0 mHz range – far out of LIGO's ~ 10^3 Hz range.

1.3.3 The nature of the secondary

In this thesis, we will characterize the nature of the secondary star (its composition, evolutionary history, and current stage of evolution) primarily in terms of its mass-radius ($M_2(R_2)$) relation. For the H CVs, approximating the secondary as a main-sequence star enabled us to tightly constrain relationships among M_2, R_2, ρ_2, a, and P_{orb}. For He CVs, the range of possible degrees of degeneracy renders these relations highly uncertain. Chapter 4 will describe the range of possible He CV evolutionary trajectories set by two limiting cases:

fully-degenerate and partially-degenerate secondaries, where the latter classification is defined by the M (R) relation of a ~ one-solar-mass star near core He exhaustion.

1.3.4 Long-term evolution

Which term wins the tug-of-war of Eq. 1.17? For all secondaries that fall within the range described above, it is predicted that the expansion of the secondary upon mass loss will dominate evolution. The $\varepsilon(P_{orb})$ study of Chapter 4 is consistent with this prediction. Furthermore, as P_{orb} lengthens, $\dot{M}$ should decrease – a relation illustrated by the two trends in Fig. 1.10, each as a function of M_2. Spectroscopic observations are consistent with Fig. 1.10: He CVs with $P_{orb} < 20$ min show absorption-line spectra (consistent with disc matter in a high state), those with $P_{orb} > 40$ min show emission-line spectra (consistent with a quiescent state), and those with P_{orb} between 20 and 40 minutes alternately display lines in emission and absorption.

There have been, however, just three *direct timings* of orbital period evolution in He CVs. Results of these timings do not support the prediction of lengthening period, and two of three of the timings are consistent with evolution still governed by angular momentum loss due to GWR. That is: they indicate that the secondaries in these two systems are not yet appreciably degenerate to guide long-term evolution to longer period, and hence that the systems have not yet reached a "period minimum." These observations will be the topic of Chapter 5.

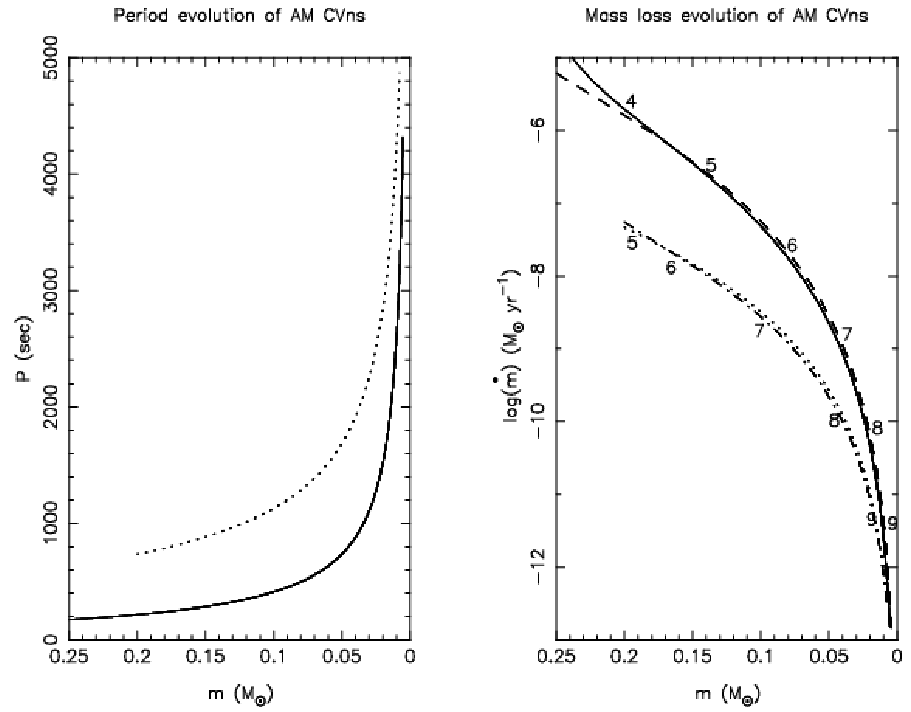

Fig. 1.10: Predictions of the evolution of He CVs (Nelemans et al. 2001). *Left*: P_{orb} as a function of secondary mass. Solid and dashed lines are for white dwarf secondaries of initially 0.25 $M_\odot$ and a primary of initial mass 0.4 and 0.6 $M_\odot$, respectively, assuming efficient coupling between accretor spin and orbital motion. *Right*: $\dot{M}$ as a function of m. Dash-dotted and dotted lines are for a He star secondary, starting when the He star becomes semi-degenerate (m ~ 0.2$M_\odot$); primaries are 0.4 and 0.6M_{sun}. The numbers along the lines indicate the logarithm of the time in years since the beginning of the mass transfer.

1.3.5 Routes to He CV synthesis

The long-term evolution of a He CV is primarily set by its route to birth, which is characterized by the nature of the secondary at the onset of core He burning, and again at Roche lobe overflow (RLOF) (Chapter 5). Theoretically, all birth channels require the survival of *two* CE phases: once during the post-main-sequence evolution of the primary, and again for the secondary – each of which is an unlikely feat of nature. Some spectroscopic analyses of chemical composition have recently shown promise as a method of discriminating among birth channels (Nelemans et al. 2010).

It will often be impossible to distinguish these channels because they are all predicted to lead to the same ultimate secondary: a low-mass degenerate white dwarf. For this reason, it is desirable to find systems that are still evolving to shorter P_{orb}.

1.3.6 Population synthesis

The intrinsic population of He CVs is poorly constrained, due to theoretical uncertainties regarding the probability of survival of a binary through two CE phases without being destroyed by detonations from He accretion onto the primary, and other conditions leading to stable mass transfer. Accounting for the poor theoretical constraints, it still appears likely that observations have undersampled the population. For details, see Appendix H.

1.3.7 Helium CVs in this dissertation

Studies of specific helium CVs will comprise Chapters 3, 4, and 5, as follows:

- Chapter 3: orbital and positive superhump period identifications for CP Eridani;
- Chapter 4: update of the ε-P_{orb} relation for He CVs, to chart evolution;
- Chapter 5: orbital period evolution and disc signals in AM Canum Venaticorum.

REFERENCES

[1] Barros, S. C. C., Marsh, T. R., Dhillon, V. S., et al. 2007, MNRAS, 374, 1334

[2] Chandrasekhar, S. 1939. *An Introduction to the Study of Stellar Structure*. New York: Dover

[3] D'Antona, F., Ventura, P., Teodorescu, A. 2006, ApJ, 653, 1429

[4] Downes, R., Webbink, R., Shara, M., Ritter, H., Kolb, U., Duerbeck, H. 2005, JAD, 11, 2

[5] Faulkner, J. 1971, Ap J, 170, L99

[6] Faulkner, J., Flannery, B. 1972, Ap J, 175, L79

[7] Gänsicke B. T., Dillon M., Southworth J., et al., 2009, MNRAS, 397, 2170

[8] Gianninas A., Bergeron P., Fontaine G., 2006, AJ, 132, 831

[9] Hakala, P, Ramsay, G., Wu, K., Hjalmarsdotter, L., Jarvinen, S., Jarvinen, A., Cropper, M. 2003, MNRAS, 343, L10

[10] Hellier, C. 2001. *Cataclysmic Variable Stars: How and Why They Vary*, Chichester, UK: Springer

[11] Iben, I., Jr., Fujimoto, M. Y., MacDonald, J, 1992, Ap J, 384, 580

[12] Israel, G. L., Covino, S., Dall'Osso, S., et al. 2004, Mem. S.A. It. Suppl., 5, 148

[13] Katz, J.I. 1973, Nature Phys. Sci., 246, 87

[14] Knigge C., 2006, MNRAS, 373, 484

[15] Knigge, C., Hynes, R., Steeghs, D., Long, K., Araujo-Betancor, S., Marsh, T. 2002, Ap J, 580, 151. *Adapted from*: Ishioka, R., Uemura, M., Matsumoto, K., Ohashi, H., Kato, T., Masi, G., Novak, R., Pietz J., artin, B., Starkey, D., Kiyota, S., Okansen, A., Moilanen, M., Cook, L., Kral, L., Hynek, T., Kolasa, M., Vanmunster, T., Richmond, M., Kern, J., Davis, S., Crabtree, D., Beaulieu, K., Davis, T., Aggleton, M., Gazeas, K., Niarchos, P., Yushchenko, A., Mallia, F., Fiaschi, M., Good, G., Boyd, D., Sano, Y., Morikawa, K., Moriyama, M., Mennickent, R., Arenas, J., Ohshima, T., Watanabe, T. 2002, A&A, 381, 41

[16] Knigge C., Baraffe I., Patterson J., 2011, ApJS, 194, 28

[17] Kolb, U., Stehle, R. 1996, MNRAS, 282, 1454

[18] Kolb U., 1993, A&A, 271, 149

[19] Kraft, R., Mathews, J., Greenstein, J. 1962, Ap J, 136, 312

[20] Landau, L., Lifshitz, E., 1951, *The Classical Theory of Fields*, Cambridge: Addison-Wesley

[21] Larwood, J. 1998, MNRAS, 299, 32

[22] Linnell, A. 1949, Sky and Telescope, 8, 166

[23] Lubow, H, Shu, F. 1977, Ap J, 216, 517

[24] Malmquist, K. 1936, Stockholms Observatoriums Annaler, 12, 7

[25] Maloney, P., Begelman, M. 1997, Ap J, 491, L43

[26] Marsh, T.R., Nelemans, G. 2005, MNRAS 363, 581

[27] Murray, J. 2000, MNRAS 314 1

[28] Nelemans, G., Wood, M., Groot, P., Anderson, S., Belczynski, K., Benacquista, M., Charles, P., Cumming, A., Deloye, C., Jonker, P., Kalogera, V., Knigge, C., Marsh, T., Motl, P., Napiwotzki, R., O'Brien, K., Phinney, E. 2009, The Astron. and Astrophys. Decadal Survey, Science White Papers, 221

[29] Nelemans, G., Zwart, S., Verbunt, F., Yungelson, L. 2001, A&A, 368, 939

[30] Osaki, Y., Kato, T., 2012, eprint arXiv:1212.1516

[31] Osaki, Y. 1989, PASP, 41, 1005

[32] Osaki Y., 1974, PASJ, 26, 429

[33] Paczynski, B. 1981, Acta. Astron., 31, 1

[34] Paczynski, B., Sienkiewicz, R. 1981, Ap J, 248, L27

[35] Paczynski, B. 1971, Annual Rev. of Astron. and Astrophys., 9, 183

[36] Paczynski, B. 1967, Acta Astron., 17, 287

[37] Patterson, J., Kemp, J., Harvey, D., Fried, R., Rea, R., Monard, B., Cook, L., Skillman, D., Vanmunster, T., Bolt, G., Armstrong, E., McCormick, J., Krajci, T., Jensen, L., Gunn, J., Butterworth, N., Foote, J., Bos, M., Masi, G., Warhurst, P. 2005, PASP, 117, 1204

[38] Patterson, J., Thorstensen, J., Kemp, J., Skillman, D., Vanmunster, T., Harvey, D., Fried, R., Jensen, L., Cook, L., Rea, R., Monard, B., McCormick, J., Velthuis, F., Walker, S., Martin, B., Bolt, G., Pavlenko, E., O'Donoghue, D., Gunn, J., Novak, R.,

Masi, G., Garradd, G., Butterworth, N., Krajci, T., Foote, J., Beshore, E. 2003, PASP, 115, 1308

[39] Patterson, J., Masi, G., Richmond, M., Martin, B., Beshore, E., Skillman, D., Kemp,J., Vanmunster, T., Rea, R., Allen, W., Davis, S., Davis, T., Henden, A., Starkey, D., Foote, J., Oksanen, A., Cook, L., Fried, R., Husar, D., Nova´k, R., Campbell, T., Robertson, J., Krajci, T., Pavlenko, E., Mirabal, N., Niarchos, P., Brettman, O., Walker, S. 2002, PASP, 114, 721

[40] Patterson, J. 1999, Disc Instabilities in Close Binary Systems Conf., 61P

[41] Patterson, J., Jablonski, F., Koen, C., O'Donoghue, D., Skillman, D. 1995, PASP, 107, 1183

[42] Patterson, J., Sterner, E., 1992, ApJ, 384, 234

[43] Petterson, J.A., 1977, Ap J, 218, 783

[44] Poe, E. A., 1849, *The Bells.* New York: Sartain's Union Magazine

[45] Pretorius, M., Knigge, C., O'Donoghue, D., Henry, J., Gioia, I., Mullis, C. 2007a, MNRAS, 382, 1279

[46] Pretorius, M., Knigge, C., Kolb, U., 2007b, MNRAS, 374, 1495

[47] Pringle, J. 1981, American Rev. Astron. Astrophys., 19, 137

[48] Pringle, J. 1996, MNRAS, 281, 357

[49] Ramsay, G., Hakala, P., Wu, K., et al. 2005, MNRAS, 357, 49

[50] Reinsch, K., Steiper, J., Dreizler, S. 2007, in ASP Conf. Ser. 372, 15th European Workshop on White Dwarfs, ed. R. Napiwotzki, & M. R. Burleigh, (San Francisco: ASP), 419

[51] Ritter H., Kolb U., 2010, VizieR Online Data Catalog, 1, 2018

[52] Roelofs, G. H. A., Rau, A., Marsh, T., et al. 2010, ApJ, 711, L138

[53] Rutten, R., Kuulkers, E., Vogt, N., van Paradijs, J. 1992, A&A, 265, 159

[54] Savonije, G., de Kool, M., Van den Heuvel, E., 1986, Astron. Astrophys., 155, 51

[55] Schwartzschild, M., 1958. *The Structure and Evolution of the Stars*. New York: Dover

[56] Shu, F., Lubow, S., Anderson, L. 1976, Ap J, 209, 536

[57] Skinner, J., Thorstensen, J., Armstrong, E., Brady, S. 2011, PASP, 123, 259

[58] Smak, J. 1991, Acta Astron., 41, 269

[59] Solheim, J. 2010, PASP, 122, 1133

[60] Strohmayer, T. 2004, ApJ, 610, 416

[61] Tsugawa, M., Osaki, Y. 1997, PASJ, 49, 75

[62] Uthas, H. 2010, *Observational Studies of Highly Evolved Cataclysmic Variables*, PhD Thesis, University of Southampton, UK

[63] Vogt, N. 1983, Astron. Astrophys., 118, 95

[64] Walker M. F., 1956, ApJ, 123, 68

[65] Walker, M. 1954, PASP, 66, 230

[66] Warner, B. 1995. *Cataclysmic Variable Stars*. Cambridge: Cambridge University Press

[67] Warner B., Woudt P. A., 2008, in Amer. Inst. of Phys. Conf. Ser., edited by M. Axelsson, vol. 1054, 101–110

[68] Warner B., 2004, PASP, 116, 115

[69] Warner B.,Woudt P. A., 2002, MNRAS, 335, 84

[70] Warner B., van Zyl L., 1998, *New Eyes to See Inside the Sun and Stars*, edited by F.-L.Deubner, J. Christensen-Dalsgaard, &D. Kurtz, vol. 185 of IAU Symposium, 321

[71] Whitehurst, R. 1988, MNRAS, 232, 35

[72] Wijers, R., Pringle, J. 1999, MNRAS, 308, 207

[73] Wood, M., Still, M., Howell, S., Cannizzo, J., Smale, A. 2011, Ap J, 741, 105

[74] Yaron O., Prialnik D., Shara M. M., Kovetz A., 2005, ApJ, 623, 398

[75] Yonehara, A., Mineshige, S. 1997, Ap J, 486, 388

[76] Zapolsky, H., Salpeter, E. 1969, ApJ 158, 809

2 Observing and Analyzing Light from CVs

"Yet the ear it fully knows,
By the twanging,
And the clanging,
How the danger ebbs and flows:
Yet the ear distinctly tells,
In the jangling,
And the wrangling,
How the danger sinks and swells,
By the sinking or the swelling in the anger of the bells ...
In the clamor and the clangor of the bells!"
Poe; *The Bells* (1848)

2.1 Resources

Data used in this dissertation came from the Michigan-Dartmouth-MIT Observatory (MDM) 2.4-meter and 1.3-meter telescopes at Kitt Peak National Observatory, Arizona, and from the Center for Backyard Astrophysics (CBA). The CBA is a worldwide network of professional and amateur astronomers using ~ 0.3-1.0-meter telescopes. CBA members can collectively monitor a star continually over long baselines, and individual nightly light curves can be spliced to create time series that span decades. Such long baselines are necessary for characterizing outburst behavior and for capturing the secular evolution of orbital periods. In addition, obtaining observations from various longitudes also suppresses aliasing in the power spectra of light curves.

The CBA and MDM instruments use a charge-coupled device (CCD) camera: an array of capacitors that convert light to an electrical signal. A charge amplifier converts the signals to voltages, which can be digitized. For details of the CBA instrumentation and observing procedure, see Skillman (1981), (1993), and Skillman & Patterson (1993).

2.2 Light from a CV

The magnitude scale

It is common practice in astronomy to collapse the flux range to the logarithmic scale of magnitudes. For two stars with fluxes F_1 and F_2, the difference in their apparent magnitudes m_1 and m_2 is defined as:

$$m_2 - m_1 = -2.5 log \frac{F_2}{F_1} \tag{2.1}$$

Then a flux ratio of 100 corresponds to a magnitude ("mag") difference of 5, and a difference of 1 mag corresponds to a difference in flux by a factor of about 2.512.

The optical range (~ 3500-8000 Å) is divided into five bandbasses: U (blue), B, V, R, and I (red). The effective wavelength of a star on a CCD image (λ_{eff}) is a function of the star's peak wavelength, filter sensitivity, and CCD sensitivity. For CVs, λ_{eff} corresponds to a V mag (~ 5000-5900 Å), with helium CVs slightly bluer than hydrogen CVs. We observe CVs with either a clear filter – to maximize counts, or a V – to maximize contribution from the disc and to minimize extinction of blue light by the atmosphere. Observing in V light also facilitates comparison with other observations, as it is the most commonly-used filter among CV observers. For our purposes, the choice of filter is not critical, as the behavior of signals we are examining do not depend strongly on wavelength (within the optical bandwidth).

The disc

Except for the least luminous CVs, disc emission dominates the light at all visible wavelengths. Spectroscopically, the disc appears as a black body continuum with broad lines superimposed, either in emission or absorption. Line profiles in most emission-line systems appear double-peaked, and are attributed to Doppler broadening due to rotation (§2.9.2).

The primary

The white dwarf, with a surface temperature around 60,000 K (Urban & Sion 2006), is usually obscured by the disc light in high-state systems (e.g. Townsley & Bildsten 2002), but can sometimes be observed in the ultra-violet during quiescence. Some periodicities on the order of 1-100 seconds that are observed only in quiescent CVs have been interpreted as white dwarf spin periods (see Appendix A).

The secondary

Even with a low temperature between ~ 3,000 – 5,000 K (Knigge 2006; Knigge et al. 2011), the secondary is usually observable faintly in the infrared, due to its large surface area. It appears as a black body continuum superimposed with absorption lines of complex structure, attributed to molecules in the atmosphere. Sometimes the secondary is detectable weakly at optical wavelengths, probably due to reflected radiation from the side that faces the disc and white dwarf.

The bright spot

In non-eclipsing systems, modulation at the orbital period is attributed to the bright spot: the area of enhanced luminosity where the mass transfer stream impacts the disc.

H versus He CVs

Spectra of H CVs mainly show lines corresponding to low excitation states of the Hydrogen Balmer and Lyman series and the first ionization state of helium. In H CVs with long-duration states of high accretion, higher-ionization states of He are often present. He CVs show spectra characterized primarily by their lack of hydrogen and strong lines of ionized helium ($\frac{\mathrm{He}}{\mathrm{H}}$ by number ~ $10^{3\text{-}4}$). Carbon, nitrogen, oxygen, magnesium, and silicon are also detected in some He CVs. He CVs are systematically bluer than H CVs, and those with P_{orb} < 11 minutes appear weakly in X-rays.

For a comprehensive discussion of observations corresponding to each constituent of a CV, see Warner (1995).

2.3 Observing

Preparations for observing include continuously maintaining the CCD camera at low temperature to minimize thermal noise, and opening the dome sufficiently early to allow the air to equilibrate to ambient conditions. To minimize CCD readout time (which, for the full unbinned chip, is ~ 30 seconds), we bin the chip 2 x 2 and use a quarter of the area. This results in a field of view of ~ 5 x 5 arcminutes (or an angular resolution of ~ 1 arcsecond) and reduces deadtime to ~ 5 seconds. Typical integration times for science images are 5 – 120 seconds, depending on CV magnitude, its periods of variability, and ambient conditions.

2.3.1 Calibrations

Each pixel on a CCD chip carries a fixed “bias” voltage, which we account for by taking a series of zero-second exposures (“biases”) and subtracting their average from each science image. Within the instrument, thermally-generated electrons create noise (“dark current”) that builds up in the instrument during each exposure. To account for it, one takes a series of “darks” with the same exposure time as that of the science images but with the shutter closed, and subtracts their average from each science image.

Because the sensitivity of each filter to incoming light varies across a filter, and to account for vignetting (uneven distribution of light as it falls upon the filter), we take flat field exposures (“flats”) on a twilight sky, and divide each science image by an average master flat. If the sky is not clear, flats can be taken via manual illumination of a white screen in the dome.

2.3.2 The target field

To fine-tune the telescope alignment, we use a guider camera that has a wider field of view (several degrees) than the CCD, to identify the coordinates of a bright star. We also use the guider to maintain tracking when taking the actual science time series, by using a “guide star” that can survive light clouds. Otherwise, the telescope cannot maintain a pointing to within several arcseconds for longer than several minutes.

To identify the desired field of view, we refer to the atlas of Downes et al. (2005). The field must contain a star that is suitable to be used as a “comparison”: a star of known stable magnitude (Δmag $< 10^{-4}$). The CV light curve will be a plot of differential magnitude with respect to the comparison. Ideally, we choose a comparison that is:

- of comparable brightness to the CV, to avoid saturation of either star’s light;
- of comparable color to the CV, to minimize differential extinction across wavelengths;
- not near an edge of the field, in the event that the guide star is lost and the telescope drifts. The CCD is more sensitive than the guider, and the CV and comparison can sometimes survive mild clouds and wind. Thus if drift occurs for fewer than ~ minutes, usually the comparison can be kept in the field and the image can still be used.

If a record of a previous comparison has been kept, for consistency we use the same comparison.

Finally, the focus must be monitored and sometimes adjusted during the time series, as the concavity of the mirrors depends mildly on ambient conditions.

Figure 2.1 shows an image before and after processing. The top left panel shows the Downes et al. (2005) chart for DQ Herculis, a CV surrounded by a faint nova shell. The top right panel shows the corresponding region of sky observed with the 1.3-meter MDM telescope, via a broadband Hσ filter (λ_{eff}=6565A; $\Delta\lambda \approx 47$A). The nova shell is not visible on this image. The middle left and bottom panels are the master flat and bias, respectively. The middle right panel is the science image after processing, in which the nova shell is now visible.

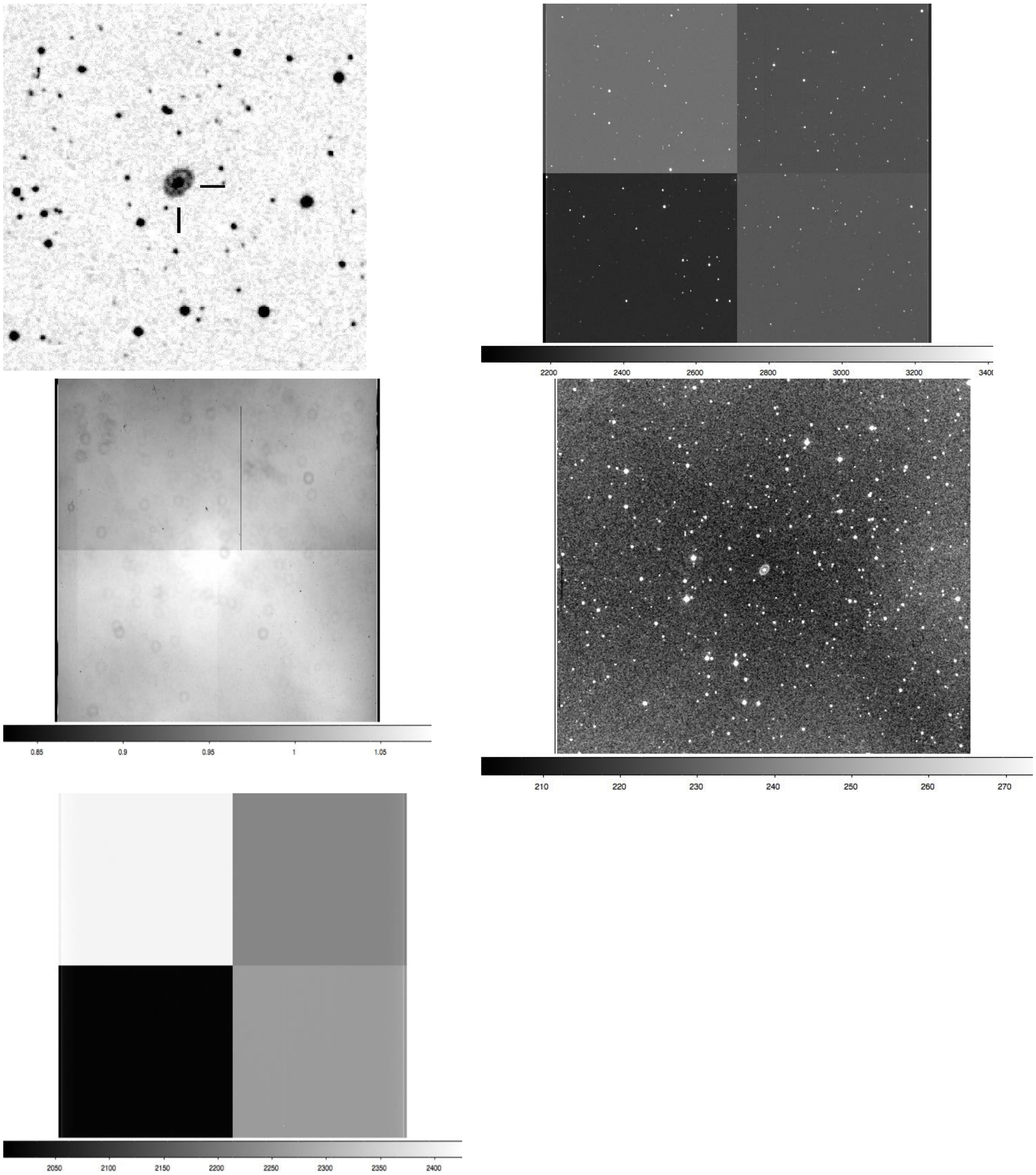

Fig 2.1: *Top left*: 5’x5’ field of view of DQ Herculis (Downes et al. 2005). *Top right*: Raw image (30 sec), using the MDM 4K detector on the 1.3-meter MDM telescope. The field is comprised of four CCD images, each with a different bias *Middle left*: Master flat of broadband Hσ filter: λ_{max}=6565A; $\Delta\lambda \approx$47A”. *Middle right:* Science image after processing. *Bottom*: Master bias. (Uthas 2012; private communication).

2.4 The light curve

On each processed science image, we center circular apertures on the CV and comparison, and adjust the radius of each aperture to achieve reasonable signal-to-noise (S/N) for each star. We make a standard heliocentric time correction, transforming our record of the arrival time of light by accounting for the difference between the distance of Earth versus distance of the Sun to the object, which is a function of the date of observation. Sometimes the barycentric correction, which references the center of mass of the Solar System, is used. For the objects studied in this dissertation, the difference is negligible. Finally, because the sine waves that we are about to fit for the purposes of Fourier analysis must have a mean value of zero, we subtract the mean nightly magnitude from each image.

2.4.1 Splicing light curves

The frequency resolution of a power spectrum depends strongly on the total baseline of observations: empirically, the error in frequency of a feature in a power spectrum is ~ 0.1/N cycles per day (c d^{-1}), where N is the total baseline in days (§2.5.3.2). Hence, to obtain period estimates, we splice numerous nights of good quality[1].

2.4.2 Practices avoided

Detrending

Occasionally a night's light curve shows a trend of increasing or decreasing average magnitude that is likely to be a contaminating effect, such as sky brightening toward sunrise. Observers sometimes account for this by "detrending" the light curve. I chose not to detrend

---

[1] When searching for signals with periods longer than several hours, it is important to splice nights prior to subtracting the mean – as subtracting mean magnitudes from individual nights would erase variability occurring on a period longer than a day.

any data that are presented in this dissertation, for two reasons. First: one can never be certain that the "trend" is not intrinsic to the CV. Secondly: it is not possible to remove an artifact from a data set without unintentionally introducing another.

Zeroing of data

"Zeroing data" means: to assign a value of zero magnitude within gaps in a baseline of observations. To zero data is to assume that during a time span when no data were obtained, the object emitted zero energy. This assumption is patently incorrect, and the power spectrum of a zeroed light curve will misrepresent the object's behavior. There exist analysis algorithms that require evenly-spaced data as input and thus force the user to zero gaps between observing windows. One great advantage of the technique employed in this dissertation – the Lomb-Scargle technique (§2.5.3) – is its facility in handling data that are unevenly-spaced in time.

2.5 The power spectrum

A power spectrum should always be considered within the context of a by-eye examination of the light curve, as the light curve's appearance gives an important first impression of the CV's behavior. It will usually reveal whether eclipses are present, and will indicate the outburst state. To determine precise values of periods, however, we look to the power spectrum.

2.5.1 The Fourier transform

We represent a time series as a sum of sine and cosine terms over a range of frequency, via the Fourier transform. The Fourier transform maps a time series into a series of frequencies that compose it, and is expressed as:

$$f(\nu) = \int_{-\infty}^{\infty} f(t) e^{-2\pi i\nu t}\, dt \qquad 2.1$$

(Fourier 1822), where the f(t)'s are the data in time space and f(ν)'s are the data in frequency space. The value $[f(\nu)]^2$ is the "power spectrum" or "spectral density" of f(t). It is a useful quantity because it can be easily plotted over a range of frequencies. The values f(ν) are difficult to plot because they are complex numbers.

2.5.2 The discrete Fourier transform and the periodogram

A *discrete* Fourier transform (DFT) is a modification of the continuous case, for handling data that are not continuously distributed in time. It goes as follows.

We define a set of data that have sampled a variable X at a set of times $\{t_i\}$ as:

$$\{X(t_i), i = 1,2,3, \ldots N_0\} \qquad 2.2$$

We assume that each measurement will be a sum of a signal X_s and random error R (or "noise"). We then define the DFT for an arbitrarily sampled data set as:

$$FT_X(\omega) = \sum_{j=1}^{N_0} X(t_j) e^{-i\omega t_j} \qquad 2.3$$

Conventionally the *periodogram* is then defined as:

$$P_X(\omega) = \frac{1}{N_0} |FT_X(\omega)|^2 \qquad 2.4$$

$$= \frac{1}{N_0}\left[\left(\sum_j X_j cos\omega t_j\right)^2 + \left(\sum_j X_j\, sin\omega t_j\right)^2\right] \qquad 2.5$$

(Schuster (1898), Thomson (1971), and Deeming (1975)). This expression can be evaluated at any frequency and interpreted as follows. If X_j contains a sinusoidal component with frequency ω_0, then at or near $\omega = \omega_0$, the factors X(t) and $e^{-i\omega t}$ are in phase and make a large contribution to $P_X(\omega)$. At other values of ω, the terms are randomly positive and negative, and do not contribute significantly. Thus, a plot of ω versus $P_X(\omega)$ will indicate frequencies of high significance relative to the noise. Furthermore, if the sample times are *evenly spaced*, then the sine and cosine terms in Eq. 2.5 are orthogonal, yielding a power spectrum with independent variables $P(\omega_n)$. The assumption of evenly-spaced data is rarely valid for time series photometry of CVs, and is not valid for any data discussed in this dissertation.

2.5.3 The Lomb-Scargle Periodogram

2.5.3.1 Handling unevenly-spaced data

Lomb (1976) and Scargle (1982) modified the periodogram to optimize it for use upon a time series that has been unevenly sampled in time. The redefinition is:

$$P_X(\omega) = \left\{\frac{\left[\sum_j X_j cos\omega(t_j - \tau)\right]^2}{\sum_j cos^2\omega(t_j - \tau)} + \frac{\left[\sum_j X_j sin\omega(t_j - \tau)\right]^2}{\sum_j sin^2\omega(t_j - \tau)}\right\} \qquad 2.6$$

where τ is defined by:

$$\tan(2\omega\tau) = \frac{\sum_j \sin 2\omega t_j}{\sum_j \cos 2\omega t_j} \qquad 2.7$$

This form is preferred for unevenly-sampled data because it is equivalent to least-squares fitting of sine waves to data, thanks to the introduction of tau. As noted above, the problem with using Eq. 2.4 & 2.5 for data that have been unevenly sampled in time is that the sine and cosine terms are no longer orthogonal – and hence the powers at each frequency ($P(\omega_n)$) are no longer independent variables. One way to restore orthogonality is to transform to basis functions that mix frequencies. This feat is difficult to achieve without mixing frequencies to the extent that the purpose of spectral analysis is defeated. The formulation of Eq. 2.6 and 2.7 restores orthogonality with minimum frequency mixing, to yield a set of *approximately* independent random variables $P(\omega_n)$.

2.5.3.2 Statistical behavior

Significance

The formulation of Eq. 2.7 renders simple the problem of determining the statistical significance of a peak in a power spectrum of unevenly-sampled data. It allows us to define a power level P_0 such that if we claim the detection of a signal of power P where $P > P_0$, we will be wrong a small fraction p_0 of the time. This detection threshold is:

$$P_0 = -\ln[1 - (1 - p_0)^{\frac{1}{N}}] \tag{2.8}$$

which reduces to

$$P_o \approx \ln\left(\frac{N}{p_0}\right) \tag{2.9}$$

if p_0 is small (Scargle 1982).

Error

We apply standard definitions of error to the Lomb-Scargle periodogram. The standard deviation σ is defined as:

$$\sigma = \sqrt{\sum_{i=1}^{N} \frac{(x_i - \bar{x})^2}{N}} \tag{2.10}$$

where $\bar{x}$ is the mean value and N is the number of data points. The 1σ error range corresponds to ~ 68% of the area in a Gaussian distribution[2]. The error on the mean value derived from a distribution of measurements is σ/√N.

It is common practice in astronomy to take the error in a signal on a power spectrum

---

[2] The Gaussian distribution is defined by the probability density function:

$$f(x) = \frac{1}{\sqrt{2\pi\sigma^2}} e^{\frac{-(x-\bar{x})^2}{2\sigma^2}}$$

from the width – in frequency units – of the horizontal line drawn across the feature that corresponds to the 1σ confidence interval. For CV observing, this definition of error should be considered within the context of empirical findings that the error in cycle count Δν of a feature in a power spectrum scales inversely with the total observations baseline N, where N is measured in days:

$$\Delta\nu = \frac{0.1}{N}\ c\ d^{-1} \qquad 2.11$$

(e.g. Patterson et al. 2003)[3].

2.5.3.3 Limitations of the technique

Noise

A level of noise will always be present in time series data, and the corresponding power spectrum will be noisier than the data it represents. The amplitude of the noise in a power spectrum will not diminish as more data are obtained, and the Lomb-Scargle technique does not offer a means to improve this problem. With increasing sample size, however, the S/N of statistically significant signals will increase. Thus, long and dense observations baselines are the means of minimizing the noise problem.

Spectral leakage

Determining the statistical significance of a feature in a power spectrum is necessary but not sufficient to establishing whether the feature is a characteristic of the CV. For a time series comprised of a finite amount of data, and containing a sinusoid of frequency ω_0, the

---

[3] There is approximately a 2σ uncertainty in this estimate. For waveforms that are well approximated as pure sinusoids, the error is more like 0.03/N, and even lower for a powerful signal. For highly non-sinusoidal waveforms, the frequencies of their harmonics do not agree exactly; this contributes significantly to the uncertainty. Such is the case for most orbital waveforms.

power in the periodogram will appear at ω_0 but also will leak to other frequencies. This can occur due to both the finite total observations baseline and the finite separation in time between individual samples. This second form of leakage is often called “aliasing.”

Alaising is created by the sampling rate and windowing pattern of an observation. Fig. 2.2 shows how aliasing occurs if the frequency of a signal is faster than the rate at which it is sampled. The samples are the black dots, and can be fit by various sinusoids – each of which will appear as a feature in the power spectrum, along with the actual signal. It can be difficult to identify the signal in a forest of aliases.

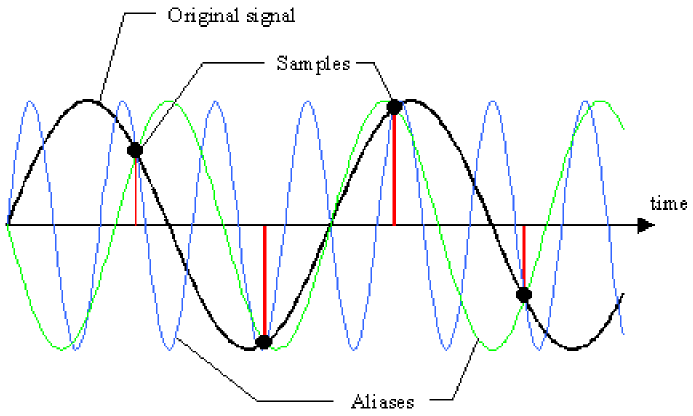

Fig. 2.2: Aliases created as a result of sampling a wave at a rate slower than the wave’s frequency of oscillation (http://www.edi.lv/media/uploads/UserFiles/dasp-web/sec-5.htm).

“One-day aliases” are a common feature in power spectra of time series light curves, and result from sampling an object over several days during approximately the same window each night, from a single longitude. They create a Gaussian pattern of peaks centered on that signal, separated by 1 c d^{-1}. Fig. 2.3 shows an example, which is taken from Chapter 3. One advantage of using a globally-distributed network of observers is that the observing windows within a 24-hour period can be staggered – and suppress aliasing.

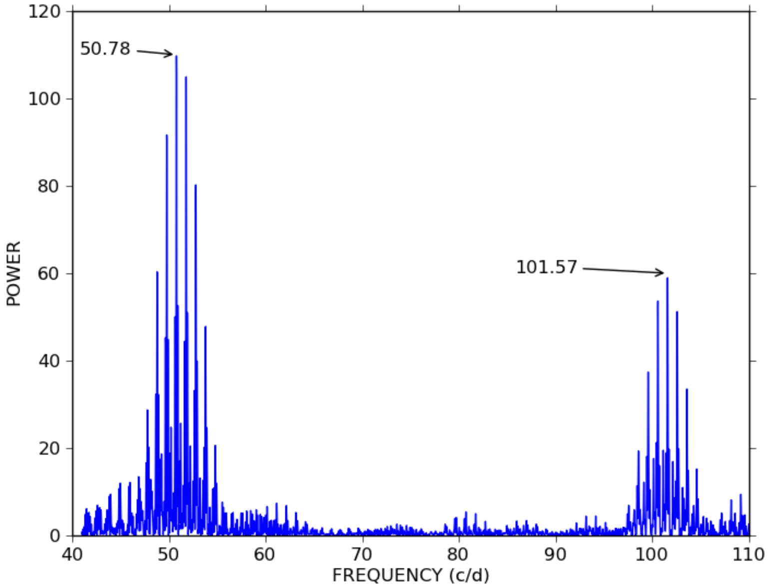

Fig. 2.3: The power spectrum of an 11-night light curve of the CV CP Eridani (reproduced from Chapter 3 of this dissertation). Two peaks (at 50.78 and 101.57 c d^{-1}) are surrounded by Gaussian patterns of "one-day aliases" that are separated by 0.1 c d^{-1}. This alias structure is typical of the power spectrum of a light curve taken from one location on Earth, and which is composed of approximately-evenly-spaced observing windows within successive 24-hour periods.

Aliases will also appear if a signal is close to the Nyquist frequency, defined as one half the value of the shortest frequency that is detectable in a data set, where the shortest frequency is set by the exposure time of a single observation. This was not a problem for the objects discussed in this thesis.

2.5.3.4 Thwarting alias structure

Mean nightly power spectrum

We can often identify the signal in a forest of aliases by creating a mean nightly power spectrum: dividing the light curve into sections and averaging their individual power spectra. Aliases will appear at different locations in each power spectrum, and will be averaged out in the composite.

Spectral window

Sometimes we wish to determine whether a feature in a power spectrum is part of the alias structure of a second feature, where the second feature has already been established as a signal. To make this determination, we take the spectral window of the second feature: we create a model sine wave and sample it using the sampling rate and windowing pattern of the original data. The spectral window is the power spectrum of this model light curve, and will contain only the signal and its alias structure – for comparison with the real power spectrum.

2.5.3.5 Finding multiple periods

Often a signal dominates a power spectrum to the extent that it competes with or obscures other signals of interest. Using the Lomb-Scargle technique recursively, we can examine and subtract each signal of successively lower power, to obtain a clearer view of weaker features. Specifically: our algorithm creates the Lomb-Scargle periodogram of a light curve, performs a least-squares fit of a user-defined signal in the power spectrum, and subtracts that signal from the light curve to create a residuals light curve. The user can perform the process recursively, on the residuals, until all signals of interest have been examined. For the executable program and documentation, see Michelsen (2012).

2.5.4 Determining persistence

The studies presented in this dissertation focus on persistent signals in CVs. To determine a signal's persistence over a baseline of observations, one can usually divide the time series into sections and examine the power spectrum of each section. The technique fails for periods so long that they constitute a significant fraction of the total baseline. This problem cast some doubt upon the identifications of superorbital periods discussed in Chapter 6.

2.6 Folding light curves

The waveform of a signal in a power spectrum is a fold of the light curve upon the period of that signal. Waveforms are important diagnostic tools. Orbital waveforms in eclipsing systems are generally highly non-sinusoidal, which is reflected in their power spectra by harmonics of the orbital frequency. The strong modulation of positive superhumps shortly after a superoutburst, on the other hand, tend to be approximate sinusoids, with a "sawtooth" appearance (see Chapter 3).

2.7 Pulse timing

We can measure the evolution of a period by means of an "observed-minus-calculated" (O-C) diagram: a measure of the accumulated discrepancy in phase (where "phase" is a fraction of one cycle), over time, between the *observed* period and a *calculated* ("test") period of constant value.

The plot is a series of timings of the arrival of maximum (or minimum) light of the waveform, over a series of light curves, each of which is of sufficient duration to yield a waveform of distinct shape. The timing from the first light curve serves as the zero point (t_0) to which all subsequent timings refer. For each light curve in the series, one calculates the number of cycles that a wave with $P = P_{test}$ would have gone through since t_0. (the "C" value), and compares it to the number of cycles that the observed periodicity went through since t_0 (the "O" value). Each light curve yields one point on a phase-versus-time plot. The trend of points reflects the degree to which the observed period deviates from P_{test}. The uncertainty is well reflected by the scatter on the diagram.

The formula is:

$$(O - C) \equiv \frac{1}{2}\frac{\dot{P}}{P}(\Delta t)^2 \qquad 2.12$$

where Δt is the observations baseline.

Possible results are:

- straight line of zero slope: $\dot{P}$= 0; P = P_{test}
- straight line of positive slope: $\dot{P}$= 0; P > P_{test}
- straight line of negative slope: $\dot{P}$= 0; P < P_{test}
- curve, concave-up: $\dot{P} > 0$
- curve, concave-down: $\dot{P} < 0$.

The O-C diagram will be used to detect evolution in orbital and superhump periods in Chapter 5.

2.8 Correlation coefficient

The Pearson correlation coefficient “r” is a measure of the linear correlation between two variables. The value of r ranges from -1 to 1 (for exact negative and positive linear correlations, respectively), and is defined as:

$$r = \frac{1}{n-1}\sum_{i=1}^{n}\left(\frac{X_i - \bar{X}}{s_X}\right)\left(\frac{Y_i - \bar{Y}}{s_Y}\right) \tag{2.13}$$

where $\bar{X}$ and s_X are the mean and standard deviation, respectively, of the distribution of X_i, and similarly for Y_i.

The Pearson correlation coefficient was used to determine the significance of correlations among trends in periodicities studied in Chapter 5.

2.9 Other techniques

Spectroscopic studies and eclipse mapping are not discussed directly in this thesis, but they comprise a significant part of the foundation upon which the model of CVs rests. Hence they merit a short summary.

2.9.1 Spectroscopic orbital periods

Orbital periods can be found spectroscopically from measurements of radial velocities of matter in the disc. For systems that do not eclipse, this measurement is preferred over the photometric measurement because it is unambiguous (unless eclipses are present, one can never be *certain* that a signal in a power spectrum is orbital in nature). The technique employs a plot of emission line profiles as a function of time. Due to Doppler shifts, the motion of gas orbiting the primary will generate lines that follow an "s" shape. One creates a superposition of all such s curves over all radii in the disc. The line center is found as a function of time, which yields a sinusoidal radial velocity curve with a period equal to P_{orb}. In this dissertation, this technique was used to find an orbital period in IM Eridani (Chapter 6).

2.9.2 Resolving line profiles

"Double-peaked" line profiles, which most CVs display, constitute strong evidence for a disc structure. The top panel of Fig. 2.4 shows the emission line spectrum of V2051 Ophiuchi after superoutburst (Papadaki et a. 2008), in which every labeled line appears double-peaked. The bottom panel shows the correspondence of regions in a double-peaked emission line profile with areas within the disc (Horne & Marsh 1986).

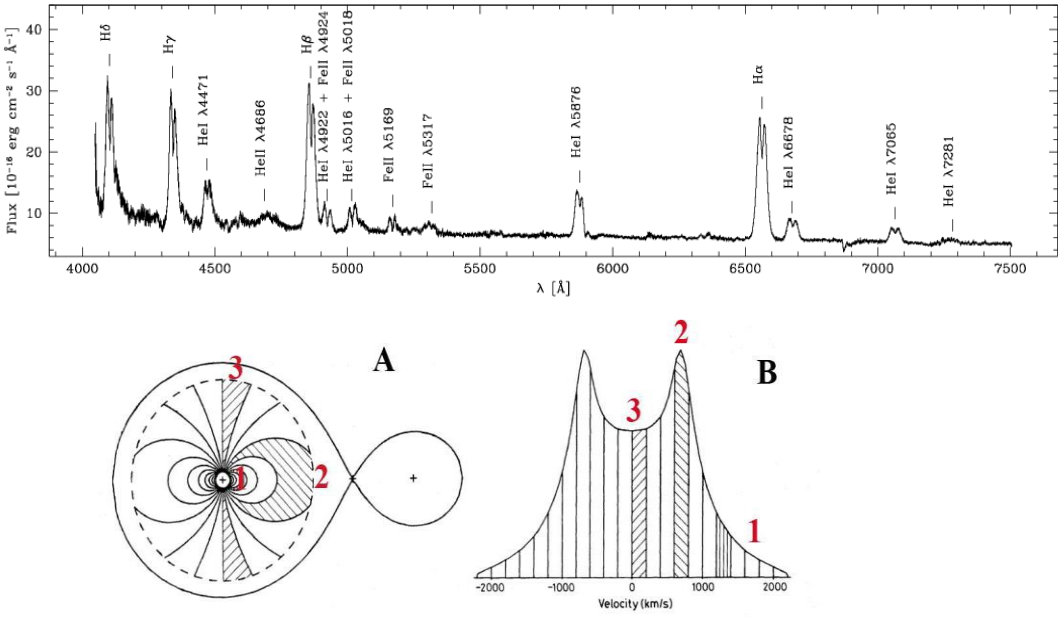

Fig. 2.4: *Top panel:* Spectrum of V2051 Ophiuchi after superoutburst, showing double-peaked line profiles (Papadaki et al. 2008). *Bottom*: an illustration showing the correspondence of regions in an emission line profile with areas of an accretion disc (Horne & Marsh 1986).

2.9.3 Eclipse mapping

Eclipse mapping is a technique applied to an eclipsing light curve to constrain mass ratio and the size of the disc and secondary star. For a review, see Baptista (2004).

REFERENCES

[1] Baptista, R. 2004, *What can we learn from accretion disc eclipse mapping experiments?.* Astron. Nachr., 325: 181–184

[2] Deeming, T.J. 1975, Ap. Space Sci., 36, 137; erratum Ap. Space Sci., 42, 257

[3] Downes, R., Webbink, R., Shara, M., Ritter, H., Kolb, U., Duerbeck, H. 2005, JAD, 11, 2

[4] Fourier, J. B. Joseph, *Théorie Analytique de la Chaleur*, Paris: Chez Firmin Didot, père et fils, 1822

[5] Horne, K., Marsh, T.R. 1986, MNRAS, 218, 761

[6] Knigge C., Baraffe I., Patterson J., 2011, ApJS, 194, 28

[7] Knigge C., 2006, MNRAS, 373, 484

[8] Lomb N. R., 1976, Ap&SS, 39, 447

[9] Michelsen, E. 2012. http://physics.ucsd.edu/~emichels/lightcurve.pdf. Accessed: 2013 Mar 29.

[10] Papadaki, C., Boffin, H., Steeghs, D., Schmidtobreick, L. 2008, A&A, 487, 611

[11] Poe, E.A., 1849, *The Bells.* New York: Sartain’s Union Magazine

[12] Scargle, J., 1982, Ap J, 263, 835

[13] Schuster, A. 1898, Terrestrial Magnetism (now J.G.R.), 3, 13

[14] Skillman, D.R., 1993, S&T, 85, 83

[15] Skillman, D.R., 1981, S&T, 61, 71

[16] Skillman, D.R., Patterson, J., 1993, ApJ, 417, 298S

[17] Solheim, J. 2010, PASP, 122, 1133

[18] Thomson, R.O.R.Y. 1971, IEEE Trans., GE-9, 107

[19] Townsley D. M., Bildsten L., 2002, ApJ, 565, L35

[20] Urban J. A., Sion E. M., 2006, ApJ, 642, 1029

[21] Warner, B. 1995. *Cataclysmic Variable Stars*. Cambridge: Cambridge University Press

[22] Warner B., Woudt P. A., 2008, in American Institute of Physics Conference Series, edited by M. Axelsson, vol. 1054 of American Institute of Physics Conference Series, 101–110

3 Positive superhump and orbital modulations in the helium CV: CP Eridani: *a case study illustrating our period-finding technique*

> **"... and thus the waltzers perforce ceased their evolutions ... and, while the chimes of the clock yet rang, it was observed that the giddiest grew pale"**
> Poe; *The Masque of the Red Death* (1850)

3.1 Summary of project

To probe He CV evolutionary history, we are particularly interested in systems that display positive superhumps during high states. The relation between positive superhump and orbital period in these systems can serve as a proxy for the direction of evolution, and thus produce a distribution of orbital periods versus time. This technique has been used extensively for hydrogen CVs. In this chapter we describe a case study (CP Eridani) that illustrates the process of identifying superhump and orbital signals in a CV.

CP Eridani (CP Eri) was one of the first confirmed helium CVs. We chose it for this study because of its long (~ 70-year) reputation for episodic eruptive behavior – and hence high likelihood of obtaining a superhump detection. Prior to this study, CP Eri had one photometric detection of a period around 28 minutes.

This chapter contains a report of photometric periodicities in CP Eri of 1716.2 ± 0.2 s and 1701.4 ± 0.2 s, obtained while the system was in quiescence. From a second observation obtained during superoutburst, we interpret the 1716-s signal as a superhump period (P_{sh}) and the 1701-s signal as P_{orb}. These calculations will enable us to place CP Eri on a plot of $\varepsilon(P_{orb})$, to trace the evolutionary history of He CVs (Chapter 4).

3.2 Introduction

CP Eri was identified as a blue variable object by Luyten & Haro (1959), who reported it at V = 17, ~ 2.5 mag brighter than it appears on the Palomar Observatory Sky Survey plates. Szkody et al. (1989) observed it at V ~ 17.8 and later at 19.7, at which time they detected a periodicity around 28 minutes (Howell et al. 1991.) Abbott et al. (1992) resolved the periodicity photometrically as 28.73 m (1724 ± 4s.) They also obtained two spectra separated in time by two months, showing weak He I in emission during the first observation and absorption during the second; neither showed hydrogen. Subsequent spectroscopic studies have been consistent with these findings (Groot et al. 2001; Sion et al. 2006). These spectral data and short period together place CP Eri in the helium-rich family of CVs. CP Eri has since been observed in high and low states, with corresponding helium lines in absorption or emission, respectively. This alternating behavior is characteristic of helium CVs in the orbital period range of 20-40 minutes.

Estimates of P_{orb} and P_{sh} for CVs are valuable because they are directly-measurable parameters and can narrate evolutionary history.

3.3 Observations

We observed CP Eri three times, several months apart, in 1998 with the 1.3-meter MDM telescope; see §2.3 for the observing procedure. We used a clear filter to maximize count rate, and a comparison star of V = 15.54. Exposure times were generally 5 – 20 seconds. Each run consisted of ~ 4.5-hour windows with ~ 19.5-hour gaps. Table 3.1 is the summary observing log. The log for the third run is condensed for brevity, because it is long (22 days) and we did not use it for period determination.

Table 3.1: CP Eri observations at the 1.3-meter MDM Observatory in 1998

Run #	*Date*	*Hours*	*Average* m_V	*Comment*
1	Jan 1	3.05	16.5	Superoutburst (SO)
	Jan 2	4.49	16.6	SO
	Jan 6	4.21	18.7 – 18.3	SO
	Jan 7	5.22	18.0 – 17.7	SO
2	Sep 17	1.58	19.5	Quiescence
	Sep 18	4.62	19.7	“
	Sep 19	4.53	19.8	“
	Sep 20	4.96	19.9 – 19.8	“
	Sep 24	4.27	20.1	“
	Sep 25	4.44	20.0	“
	Sep 26	4.97	20.0	“
	Sep 27	3.65	20.1	“
3	Dec 10-31	100.24	N/A	Varying (see Fig. 3.3)

During the 11-night run, CP Eri was highly stable and near quiescence. Average magnitude was V ~ 19.9, with a trend of decreasing brightness of 3%. Figure 3.1 (top left) shows the mean-subtracted light curve of one representative night.

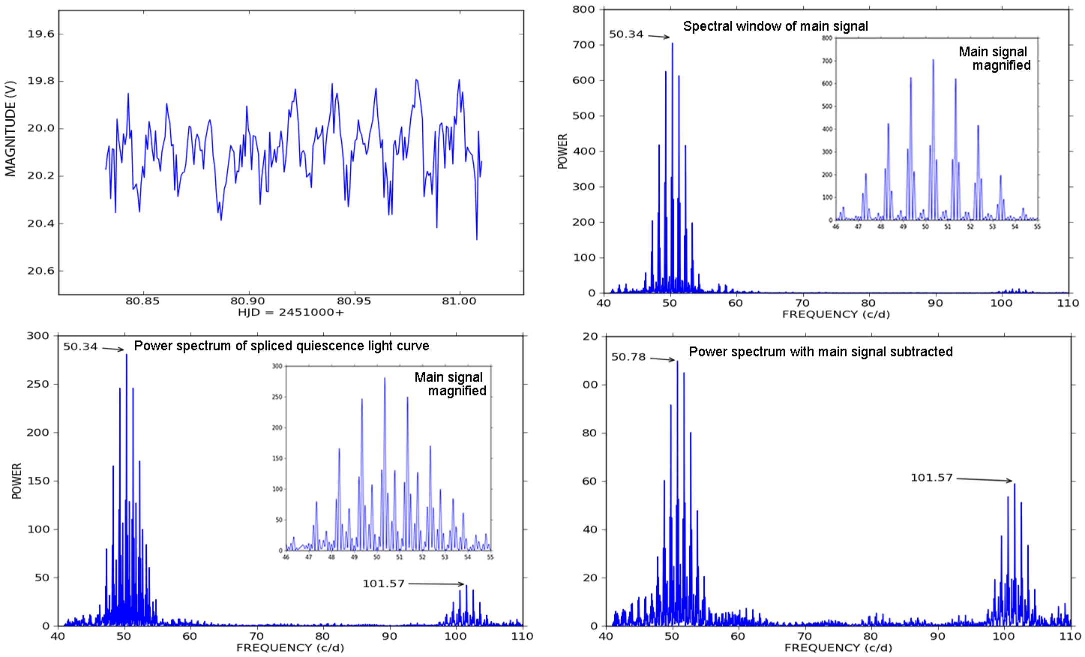

Fig. 3.1. *Top left*: Light curve of CP Eri in V light on 1998 Sep 24. The mv of the comparison star is 15.54. The error in translating from our 3500-8000 Angstrom bandpass to V mag is < 0.3 mag. *Bottom left*: Power spectrum with a baseline of eleven days, formed by splicing eight nights, each with ~ 5 hr time series. Significant features are marked with frequencies in cycles per day (c/d.) *Inset*: magnification of the main signal. *Top right*: Spectral window of the main signal, for comparison. The magnification suggests that a second independent signal may be buried in the main signal. *Bottom right*: Power spectrum of the full eleven-night baseline, with main signal subtracted.

A second observation caught CP Eri in decline from superoutburst. Figure 3.2 (top) is the light curve from Jan 2; it shows the sawtooth-shaped modulation that characterizes a positive superhump. Differential extinction is the likely cause of the slight decrease in brightness toward the end of the night. The first two nights of superoutburst data look like this, with V ~ 16.5. On the last two nights, the system was fainter and brightening (V = 18.5 and 17.8, respectively.)

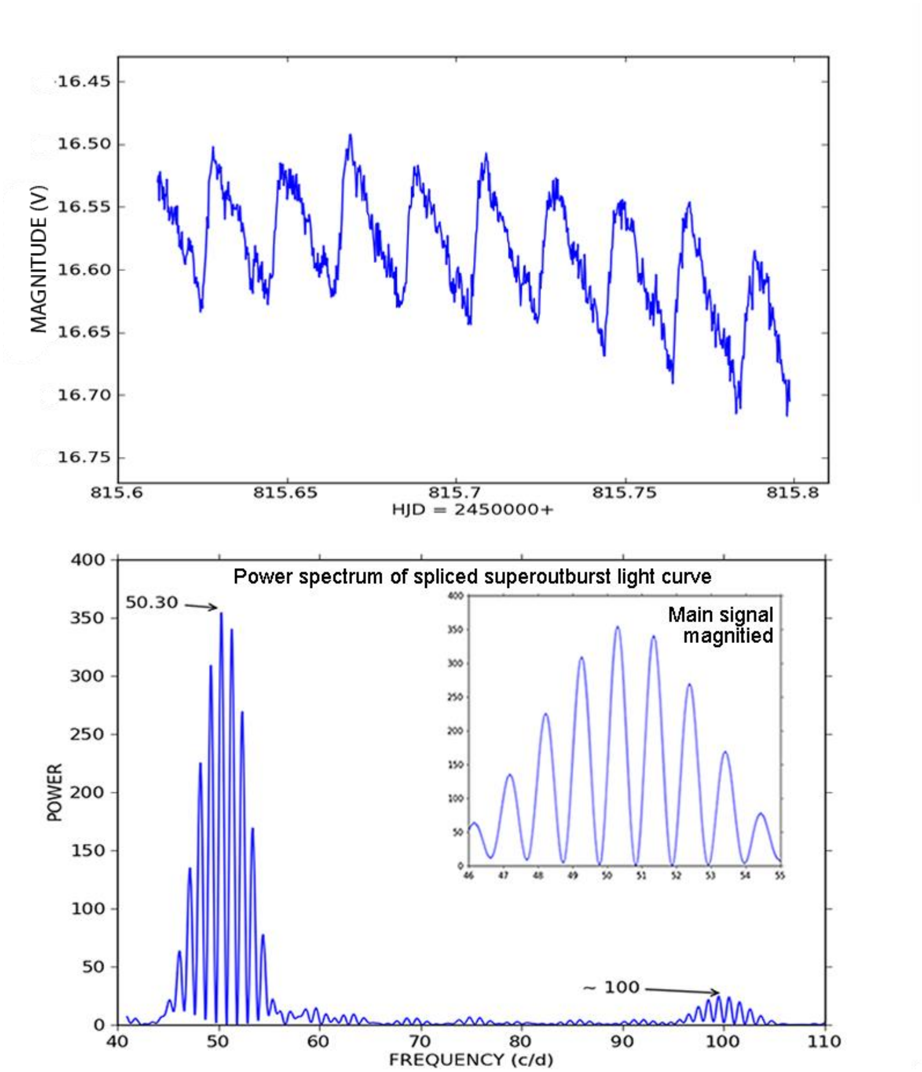

Fig. 3.2: *Top*: Light curve of CP Eri in V light on 1998 Jan 2. The mv of the comparison star is 15.54. The fading toward the end of the night is likely due to differential extinction. The error in translating from our 3500-8000 Angstrom bandpass to V mag is < 0.3 mag. *Bottom*: Nightly power spectrum, formed by splicing two consecutive nights with ~ 5 hr time series. Significant features are marked with frequencies in cycles per day. *Inset*: magnification of the main signal.

Finally, a 22-night December run caught CP Eri during a state characterized by multiple large-amplitude variations in magnitude. Figure 3.3 shows the full light curve. It would be uninformative to create a power spectrum by splicing nights during which the object displayed highly variable behavior; such a process would merely average out the variability. For each day of reasonable quality, however, the power spectrum did show a poorly-resolved period around 50 c d^{-1}, demonstrating likelihood that the main periodicity found in the quiescent data (to be discussed in §3.4.1) persists during these volatile episodes.

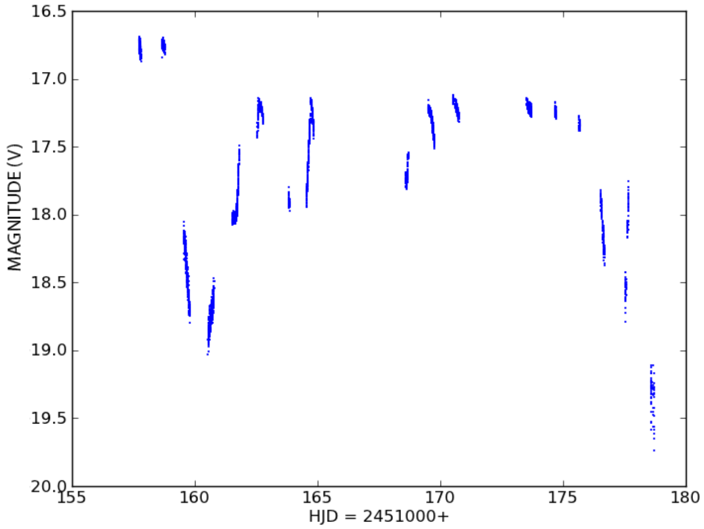

Fig. 3.3: Light curve of CP Eri in V light on 1998 Dec 10-31.

3.4 Analysis

3.4.1 Period estimation

We derived period estimates from our observations of CP Eri in quiescence, because these data comprise the longest baseline in time and are most stable in magnitude.

After subtracting the mean magnitude from each night's observations, we created a spliced light curve of the full 11-day baseline. Figure 3.1 (bottom left) shows the power spectrum with the following peaks noted: a strong signal around 50.34 cycles per day (c d^{-1}) and a weaker feature around 101.57 c d^{-1}. A fold of the light curve on a period corresponding to that frequency (50.344 c d^{-1}) yielded the waveform of Figure 3.4 (top), which shows a relatively clear sinusoidal modulation, and which also attains the best signal subtraction. The period is 1716.2 ± 0.2 s, where the error is determined from the 1σ width, in frequency units, of the signal in the power spectrum.

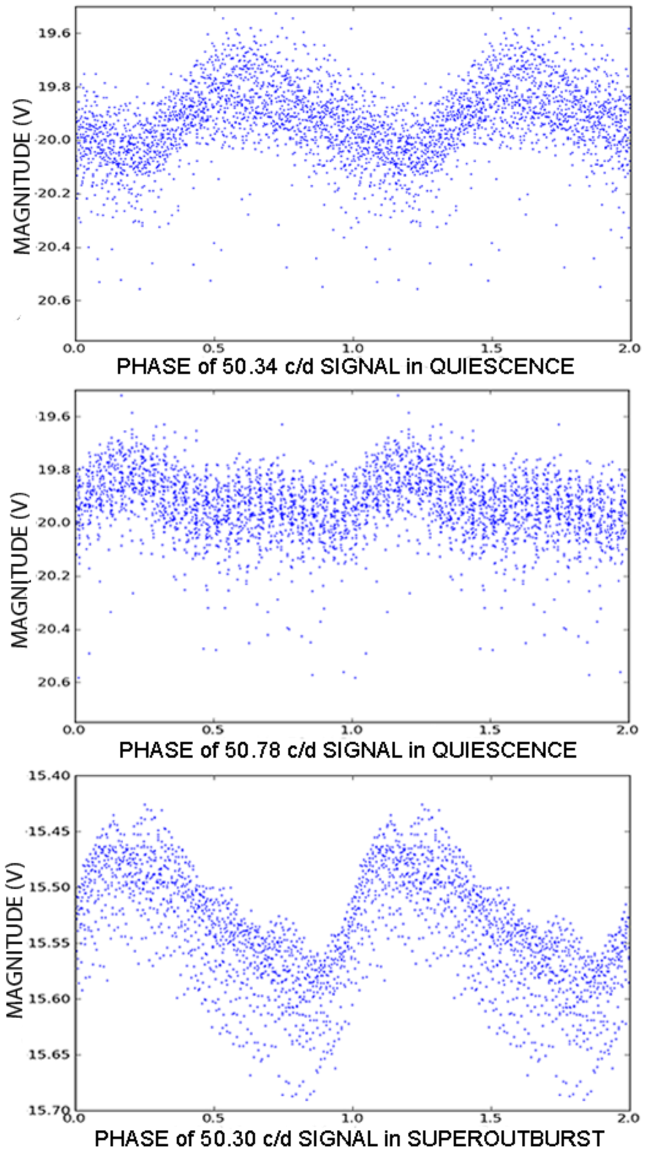

Fig. 3.4: *Top*: Quiescent light curve folded over a period of 1716.2 s. *Middle*: Quiescent light curve with main signal subtracted, folded over a period of 1701.4 s. *Bottom*: Superoutburst light curve folded over a period of 1717.6 s. The error in translating from our 3500-8000 Angstrom bandpass to V mag is < 0.3 mag.

We subtracted the main signal from the time series, which resulted in the power spectrum of Figure 3.1 (bottom right). It shows peaks at 50.78 and 101.57 c d^{-1}. A comparison with the spectral window of the main signal, Figure 3.1 (top right), indicates that these two peaks are independent of the main signal's alias structure. We interpret the latter as the second harmonic (first overtone) of the former. The waveform of the 50.78 c d^{-1} signal, Figure 3.4 (middle) is not a sinusoid, which indicates that there is significant power in harmonic structure. The period is 1701.4 ± 0.2 s.

3.4.2 Physical interpretation

For the superoutburst data, our most informative power spectrum hails from a splice of just the first two nights of observation; at this time, CP Eri was brightest and most stable (V ~ 16.5.) Figure 3.2 (bottom) shows a main signal at 50.30 c d^{-1}, a small peak around 100 c d^{-1}, and none near 50.8 c d^{-1}. Figure 3.4 (bottom) is the waveform obtained by folding the light curve over a 50.303 c d^{-1} frequency (1717.7 ± 1.2 s). A strong sawtooth-shaped modulation, characteristic of superhumps, is present. Subtraction of this main signal reveals no significant secondary features. The presence of this 50.30 c d^{-1} signal and absence of the 50.78 c d^{-1} signal leads us to interpret the former as the superhump (P_{sh}) and latter as the orbital period (P_{orb}) of CP Eri. Table 3.2 summarizes results for the quiescent and superoutburst runs.

Table 3.2: Signal frequency and corresponding period determinations for CP Eri.

Observing run	ω_{sh} *(c/d)*	P_{sh} *(s)*	ω_{orb} *(c/d)*	P_{orb} *(s)*
Quiescence (11 days)	50.344 ± 0.005	1716.2 ± 0.2	50.781 ± 0.005	1701.4 ± 0.2
Superoutburst (2 days)	50.303 ± 0.035	1717.7 ± 1.2	...	...

Having identified P_{sh}, we returned to our 11-night-baseline of quiescent data to study superhump drift via the nightly timings of minimum light of the superhump waveform. We did not find evidence for period evolution.

3.4.3 The rapid magnitude variations

Finally, during the 22-day observing run, CP Eri exhibited volatile behavior, sharply rising and falling multiple times between V ~ 16.6 and 19.5 (Figure. 3.3). Our most informative power spectrum derives from a splice of seven nights near the end of the run. It shows a poorly-resolved peak near 50.3 c d^{-1} and a possible feature around 102 c d^{-1} – demonstrating likelihood that the main periodicity found in the quiescent data persists during these episodes. The most pertinent use of these data is as a record of CP Eri's proclivity toward this erratic behavior, which appears to be a characteristic of helium CVs in the period range of 20-40 minutes. CR Boo and V803 Cen have shown similar behavior (Kato et al. 2000, Patterson et al. 2000, respectively), and most of the He CVs in this period range have been observed in both high and low states (Solheim 2010).

3.5 Discussion

The superoutburst of a CV is a rapid rise in brightness by ~ 2 – 10 mag that persists for days to weeks. At the onset of superoutburst, a CV usually develops a positive superhump that fades in the weeks following maximum light, and which occasionally persists into quiescence. The positive superhump is interpreted as a beat between P_{orb} and apsidal precession period of a disc that has gone elliptical due to the gravitational perturbation of the secondary. A resonance between the orbit of the disc material and the orbit of the secondary – most likely the 3:1 resonance – can cause the disc to grow sufficiently elliptical such that it precesses, and tidal stresses on the disc material periodically dissipate energy, which produces the observable modulation (Whitehurst 1988, Osaki 1989). For He CVs, superhumps (and all high-state behaviors) are unique to systems with $P_{orb} < 40$ minutes (e.g. Solheim 2010).

Our primary justification for our period interpretations, then, hails from our short superoutburst observation. Superhumps characteristically have a repeatable waveform of fast rise and slow decay, with a modulation of ~ 0.2 – 0.3 mag – an apparent feature of the superoutburst light curve we obtained of CP Eri. The one period present in the corresponding power spectrum is 1717.7 seconds. Therefore, this observation confers additional credentials upon the 1717-s signal for a superhump interpretation. Furthermore, the superoutburst data do not show the ~ 1701-second period that was observed during quiescence. It is common during superoutburst for the superhump to overpower an orbital signal (Warner 1995).

Why the disparity from the previous observation of CP Eri with one main periodicity of 1724 ± 4s (Abbott et al. 2002)? We attribute it largely to the difference in CP Eri's stability between our respective runs. Since Abbott et al. detected just one period, it is likely that they observed the system closer to superoutburst – that is, while P_{orb} was obscured by the superhump luminosity.

We do not, however, imply that we expect future observations to confirm our value of P_{sh} to within our derived errors. On the contrary, longer time series observations are likely to detect a drift in the superhump period, which is the characteristic behavior of these signals. Furthermore, we did not catch any portion of CP Eri's rise to superoutburst and thus cannot reference a time of maximum light.

3.6 Acknowledgements

Chapter 3 is, in part, a reproduction of material as it appears in Monthly Notices of the Royal Astronomical Society: Armstrong, E., Patterson, J., Kemp, J. 2012, MNRAS, 421, 2310. This dissertation author was the primary investigator and author of this paper.

REFERENCES

[1] Abbott, T. M. C., Robinson, E.L., Hill, G.J., Haswell, C.A. 1992, ApJ, 399, 680

[2] Groot, P. J., Nelemans, G., Steeghs, D., Marsh, T. R. 2001, ApJ, 558, 123

[3] Howell, S.B., Dobrzycka, D., Szkody, P., Kreidl, T.J. 1991, PASP, 103, 300

[4] Kato, T., Nogami, D., Baba, H., Hanson, G., Poyner, G. 2000, MNRAS 315, 140

[5] Luyten, W.J., Haro, G. 1959, PASP, 71, 469

[6] Patterson, J. 2001, PASP, 113, 736

[7] Patterson, J. 2000, PASP, 112, 625

[8] Poe, E.A., 1850, *The Masque of the Red Death*. Philadelphia: Graham’s Lady’s and Gentleman’s Magazine

[9] Sion, E.M., Solheim, J., Szkody, P., Gaensicke, B.T., Howell, S.B. 2006, ApJ, 636, 125

[10] Solheim, J.E. 2010, PASP, 122, 1133

[11] Szkody, P., Howell, S.B., Mateo, M., Kreidl, T.J. 1989, PASP, 101, 899

[12] Warner, B. 1995, Ap&SS, 225, 249

4 The ε(P_{orb}) diagram: *charting evolution in helium CVs*

"By a route obscure and lonely ... I have reached these lands."
Poe; *Dream-land* (1844)

4.1 Summary of project

The evolutionary model for helium CVs is not nearly as well developed as that for their hydrogen-rich counterparts. To probe our incomplete picture of these objects, we are applying a technique that was developed for hydrogen CVs, which is detailed in a series of papers beginning in 1998 (e.g. Patterson et al 2002, 2005). The technique uses observations of systems with positive superhumps, in which the fractional superhump period excess ε is defined according to Eq. 1.15, as:

$$\varepsilon = \frac{P_{SH+} - P_{orb}}{P_{orb}}$$

where P_{SH+} is the positive superhump period. The motivation for defining this quantity is as follows.

While for any particular CV, the direction of mass ratio q points in the direction of evolution, q is difficult to measure for non-eclipsers. For CVs showing positive superhumps, however, ε is expected to decrease with q – a prediction that has been confirmed empirically – and *ε is directly measurable*. Thus, a plot of ε versus P_{orb} has the potential to chart evolution. Measurements of several hundred hydrogen CVs with positive superhump detections indicate a trend of evolution toward shorter P_{orb} (Fig 1.9).

Our update of the $\varepsilon(P_{orb})$ diagram for helium CVs that was created by Patterson et al. (2002) includes three modifications:

1. three additional CVs and one corrected measurement (including the measurements of CP Eri from Chapter 3), for a total of 10;
2. a refined empirical $\varepsilon(q)$ relation;
3. the addition of a shaded error region for each of two model CVs: those containing fully- and partially-degenerate secondaries, respectively. For each model, the shaded region corresponds to a range of masses for the primary: $0.6 < M_1 < M_{sun}$.

Ten is a small sample size, but the result tentatively indicates that He CVs are evolving toward longer orbital period, and that the secondaries are well described as partially-degenerate objects.

4.2 Justification for using ε as a proxy of q

Positive superhumps in CVs are interpreted within the context of the superoutburst mechanism described in §1.2.3, where a disc of sufficiently large R_{outer} is driven elliptical by the tidal pull of the secondary. As the secondary loses mass, its pull on the disc weakens, ellipticity decreases, the precession rate slows – and the corresponding beat (P_{SH+}) should quicken. Formally, this goes as follows.

For a binary with a Roche lobe-filling secondary, the frequency of apsidal precession ω_{prec} can be expressed as:

$$\omega_{prec} \approx \omega_{orb} \frac{q}{\sqrt{1+q}} \left(\frac{R_{disc}}{0.46a}\right)^{2/3} \tag{4.1}$$

(Murray 2000), where ω_{orb} is the orbital frequency, R_{disc} is the outer disc radius, and ω_{prec} is related to the positive superhump frequency by Eq. 1.1:

$$\frac{1}{P_{SH+}} = \frac{1}{P_{orb}} - \frac{1}{P_{prec}}$$

Thus we should find that over the lifetime of a particular CV, ω_{prec} slows (while the superhump frequency accelerates) – and ε decreases.[1] Empirical confirmation comes from a study of several hundred hydrogen CVs, which yielded Eq. 1.16:

$$\varepsilon = 0.18q + 0.29q^2$$

(Patterson et al. 2005), where in most cases q was determined from eclipsing systems. Note: Eq. 1.16 is an update of the relation used to create the initial version of the $\varepsilon(P_{orb})$ diagram for He CVs (Fig. 6 of Patterson et al. 2002). At that time, the best-fit empirical relation was: ε(q) = 0.216q.

4.3 Method

For any contact binary, Kepler's law combined with the requirement for Roche lobe overflow gives:

$$P_{orb}\ [\mathrm{hr}] = 8.75(M_2/R_2^3)^{-1/2} \qquad 4.2$$

(Faulkner 1972), with M_2 and R_2 in solar units. We expect a mass-radius relation for the secondary that falls between two limits: M(R) for a zero-temperature (fully-degenerate) helium/carbon white dwarf of low mass:

$$R_2 = 0.0155M_2^{-0.212} \qquad 4.3$$

(Zapolsky & Salpeter 1969), and M(R) for a partially-degenerate helium star secondary (a star that was undergoing core He burning at RLOF):

$$R_2 = 0.029M_2^{-0.19} \qquad 4.4$$

(Savonije et al. 1986). For the fully-degenerate case, Eq. 4.2 and 4.3 yield:

$$M_2 = 0.0069P_{orb}^{-1.22}. \qquad 4.5$$

For the partially-degenerate case, Eq. 4.2 and 4.4 yield:

$$M_2 = 0.018P_{orb}^{-1.27}. \qquad 4.6$$

Coupling Eq. 1.16 with Eq. 4.5 and 4.6, respectively, we get $\varepsilon(P_{orb})$ for each case. A plot of $\varepsilon(P_{orb})$ can concisely illustrate several interrelated properties of these systems. For details of the calculations leading to Eq. 4.5 and 4.6 and the model curves, see Appendix I. The theory of degenerate matter as it applies to CV secondaries will be explored in Chapter 5.

4.4 Result

Figure 4.1 shows ε-vs-P_{orb} for 10 helium CVs. It is an update of Figure 6 from Patterson et al. (2002). Table 4.1 contains the relevant data. Eight of the points were found via our period-finding technique. The two right-most points were plotted via spectroscopic determinations of q (Marsh 1999; Ruiz 2001, respectively) and an ε determination according to Eq. 1.16. The solid curves at bottom and top represent the M(R) relations of, respectively, a fully-degenerate (Eq. 4.3) and partially-degenerate secondary (Eq. 4.4), assuming $M_1 = 0.75M_\odot$, which is typical of He CVs (Knigge 2006). In this context, “fully degenerate” describes a star that was comprised of fully-degenerate matter of low atomic number (He/C/O) at RLOF. “Partially degenerate” describes a secondary that was still undergoing core He burning at RLOF. These models will be discussed in Chapter 5. Finally, the shaded region over each solid line represents, for each model, the range: $0.6 < M_1 < 1.0$.

---

[1] This relation is useful *iff* the spread of possible values of q for a given P_{orb} is small – which is satisfied by the requirement that the secondary be of appropriate size for its Roche lobe.

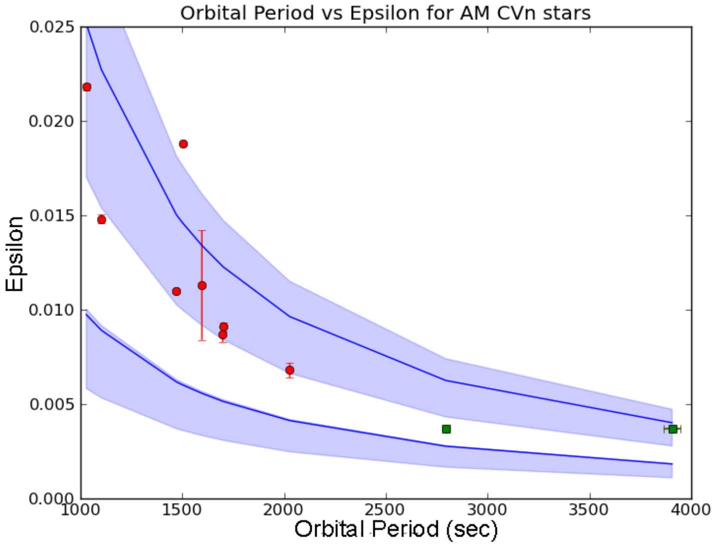

Fig. 4.1. Fractional superhump period excess ε versus Porb for 10 He CVs. Table 4.1 contains the relevant data. Eight of these points were found via our period-finding technique. The two right-most points were plotted via spectroscopic determinations of q (Marsh 1999, Ruiz 2001, respectively) and an ε determination according to Eq. 1.16. The solid curves at bottom and top represent the mass-radius relations of, respectively, a fully-degenerate secondary (Eq. 4.3), and a partially-degenerate He-star secondary (Eq. 4.4), assuming M1 = $0.75M_\odot$. The shaded region over each solid line represents, for each model, the range: 0.6 < M1 < $M_\odot$.

Table 4.1: Orbital and Superhump Periods in Helium CVs

Star	P_o	P_{sh}	ε	*q from* ε	*q (other)*	*Ref*
AM CVn	1028.7332 (3)	1051.2 (2)	0.0218 (2)	0.1038 (8)	0.18 (1)[a]	2, 3
HP Lib	1102.70 (6)	1119.0 (2)	0.0148 (2)	0.0735 (9)	...	4, 5
CR Boo	1471.30 (5)	1487.29 (2)	0.01087 (5)	0.0554 (2)	...	6, 7
KL Dra	1501.8 (1)	1530.852 (6)	0.01934 (2)	0.09339 (9)	...	8, 9
V803 Cen	1596.4 (12)	1614.5 (35)	0.011 (3)	0.06 (1)	...	5, 10
SDSS J092638+36	1698.6 (6)	1713.4 (1)	0.0087 (4)	0.045 (2)	0.041 (2)[b]	11, 12
CP Eri	1701.4 (2)	1716.2 (2)	0.0091 (5)[c]	0.047 (2)	...	1
V406 Hya	2027.8 (5)	2041.5 (3)	0.0068 (4)	0.035 (2)	...	13, 14
GP Com	2794.05 (20)	None	...	...	<0.02	15, 16
CE 315	3906 (42)	None	...	...	<0.02	17

Notes:

[a] "Other q" for AM CVn comes from doppler tomography (Roelofs et al 2006b.)

[b] "Other q" for SDSS J092638+36 comes from eclipse timing (Copperwheat et al 2011.)

[c] Value of ε for CP Eri was calculated as described in this paper, and *not* from tabulated P_{orb} and P_{sh}.

References: (1) This paper; (2) Skillman et al. 1999; (3) Provencal et al. 1995; (4) Patterson et al. 2002; (5) Roelofs et al. 2007a; (6) Patterson et al. 1997; (7) Provencal et al. 1997; (8) Wood et al. 2002; (9) Ramsay et al. 2010; (10) Patterson et al. 2000; (11) Copperwheat et al. 2011; (12) Anderson 2005; (13) Woudt & Warner 2003; (14) Roelofs 2006a; (15) Nather et al. 1981; (16) Marsh 1999; (17) Ruiz et al. 2001.

We stress two points regarding Figure 4.1. First, 9 stars fall between the two model curves, which indicates that the donors can be modeled as partially-degenerate objects. Secondly, the points trace a decreasing slope, indicating evolution toward longer P_{orb}. The reader might find it interesting to compare this plot with Fig. 4.2, from Tsugawa & Osaki (1997). They plot $\dot{M}$ as a function of P_{orb} for 6 He CVs, for each of the two secondary star models described above. The 6 systems fall upon a model line for which the secondaries are partially-degenerate He stars. In addition, $\dot{M}$ falls off with increasing P_{orb}, as expected.

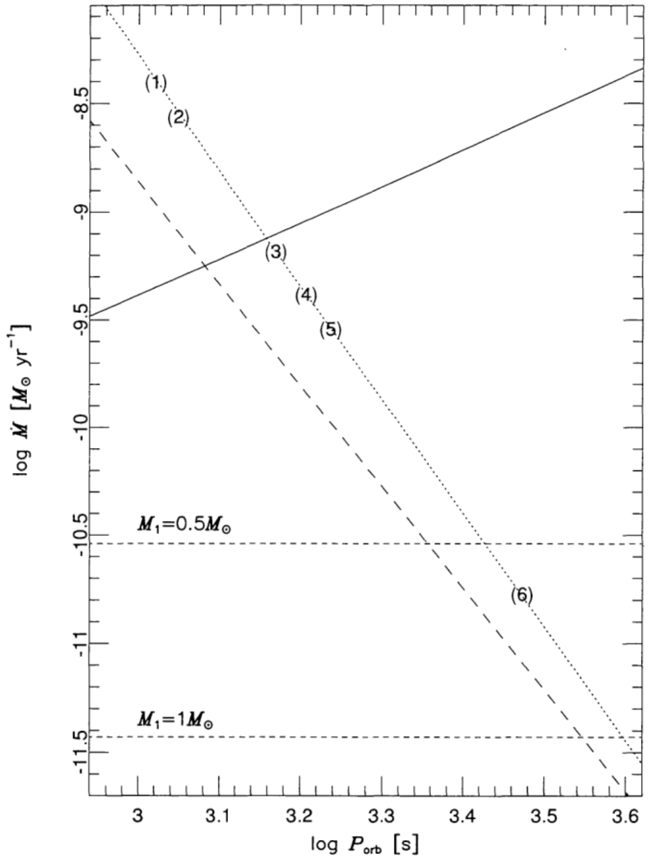

Fig. 4.2: He CVs on the P_{orb}-$\dot{M}$ plane. The solid curve shows $\dot{M}_{crit,hot}$ above which He discs are thermally stable in a high state. The short dashed lines show $\dot{M}_{crit,cool}$ below which the discs are thermally stable in a cool state, for two different masses of the primary ($1M_{sun}$ and $0.5M_{sun}$). The dotted line shows the mass-transfer rate estimated from the binary evolutionary scenario in which mass transfer is driven by GWR, and in which the secondary is a partially-degenerate He star out of thermal equilibrium. The long dashed line shows the mass transfer rate in the case of a completely degenerate secondary in thermal equilibrium. The numbers in the figure indicate the orbital periods and the mass accretion rates thus estimated for 6 He Vs: 1) AM CVn, 2) EC 15330-1403, 3) CR Boo, 4) V803 Cen, 5) CP Eri, 6) GP Com.

4.5 Placing CP Eri onto ε-P_{orb} space

Based on the results presented in Chapter 3, we twice calculated ε for CP Eri: once using the value of P_{SH+} from the quiescent run, and again using the value from superoutburst (SO). These yield values that are consistent within their errors: ε = 0.0087 ± 0.0002 and ε = 0.0095 ± 0.0008, for quiescence and SO, respectively.

The ε-P_{orb} technique of Patterson et al. takes a single value of P_{SH+} as representative of a given CV. Because superhump periods tend to drift toward longer values in the weeks following SO (e.g. Warner 1975), Patterson et al. consistently use P_{SH+} at four days after maximum superoutburst light: after the most unstable magnitude variation has passed but before most of the energy driving the superhump has radiated away. For CP Eri, neither of the two values references a time of SO maximum. In this situation we generally prefer the value obtained during SO to the value obtained during quiescence. But in this case, our quiescent run was longer by a factor of three and hence yielded a better error. Ultimately we decided to take their average: $\varepsilon = 0.0091 \pm 0.0005$. Obviously, this is a coarse estimate, but it will suffice for now because, for reasons just stated, a meaningful correction will come not from an appropriately-weighted average, but rather from a future observation of CP Eri that catches the time of SO maximum. Our main finding is that both values of ε place CP Eri in ε-P_{orb} space within the region bordered by a fully-degenerate white dwarf and partially-degenerate helium star secondary (fourth point from left, within shaded region.)

From the ε(q) relation, we obtain $q = 0.047$ for CP Eri. Taking $\langle M_1 \rangle = 0.75M_{sun}$ (Smith & Dhillon 1998; Knigge 2006), we estimate $M_2 = 0.035M_{sun}$. CP Eri's location in ε-P_{orb} space indicates that the secondary star is partially degenerate. Again, the term "partially degenerate" will be examined in Chapter 5.

4.6 Discussion of specific systems

Six of the 10 objects on the diagram merit a discussion.

AM CVn

AM CVn is the only helium CV with a dynamical determination of q from spectroscopy: $q_{sp} = 0.18 \pm 0.01$ (Roelofs et al. 2006b). This value represents an upper limit obtained from Doppler tomography on two features in the spectrum: the modulation commonly attributed to the the hot spot, and a second which is a bit mysterious: a "central spike" in the profiles of spectral lines. A central spike is seen in some quiescent systems like GP Com, and is believed to originate from the primary white dwarf. But with this identification, it is difficult to explain its appearance in AM CVn's spectrum.

The spectroscopic value of q ("$q_{\mathrm{dynamical}}$") is significantly different from the empirical value based on ε ("q_ε" = 0.101). Is this worrisome? We recognize that the ε(q) relation was established using hydrogen-rich systems only. Roelofs et al. (2006b) and Pearson (2007) have raised concern that the relation may not be valid for He discs because of the enhanced role of pressure forces. We agree that the validity of the empirical relation for He-rich systems needs observational confirmation. But the relation is likely to be at least a valuable *estimate* for He-rich systems, as the gravitational perturbation of the secondary is the main cause of disc ellipticity, and effects of gravity are not likely to depend sensitively on disc material. Tsugawa & Osaki (1997) modeled thermal and tidal instabilities for a helium disc, which is essentially the same as those for hydrogen discs (Osaki 1989), only shifted to higher temperatures. Using this model, they successfully reproduced the observed cycling state of CR Boo. (For comparison, it would be a worthwhile project to do the same for the third observation of CP Eri that was discussed in §3.3). Still, further data are needed to determine the validity of the empirical ε(q) relation for He discs. Since AM CVn is just one data point, however, at this stage an interpretation of the discrepancy between the two q values would be speculative.

KL Dra

KL Dra is the one outlier in ε(P_{orb}) space, falling far outside the distribution for a system with a partially-degenerate secondary. At the same time, KL Dra possesses the *best*-constrained value of ε of all the superhumping He CVs. It is possible that the photometric period of 1501.8 s that is interpreted as P_{orb} (Wood et al. 2002; Ramsay 2010) is really a superhump period, and that we have yet to find P_{orb}. Such a misinterpretation has occurred with several He CVs, including AM CVn itself. A ~ 2-week baseline of photometry should be sufficiently powerful to probe this possibility, using the method described for CP Eri in Chapter 3 (that is: by subtracting the 1501.8-s signal from the light curve and examining the power spectrum of the residuals for a possible underlying signal).

V803 Cen

The large error bars on V803 Cen merit a mention. We have seen many periods in this object that are not stable over long timescales. As with CP Eri, V803 Cen displays frequent cycling states (which are neither stably low or stably high). Relatively short-lived periods of 1646 (cycling state), 1622 (high state), and 1611 s (low state) have been observed photometrically (Patterson 2000). The 1611s signal was originally interpreted as P_{orb}. More recently, however, tomography has revealed a spectroscopic periodicity of 1596.4 ± 1.2s (Roelofs 2007a).

To place V803 Cen in $\varepsilon(P_{orb})$ space, we have taken the spectroscopic value of 1596.4 s as P_{orb}. For P_{sh}, we took a generous range that includes the 1622-s period that Patterson observed only during the high state, and the 1611-s period observed only during the low state. The former is more desirable in principle, since a superhump is defined by its appearance during outburst. But superhumps are known to persist into quiescence, especially in systems experiencing frequent outbursts.

SDSS J092638+362402

This system is the only known eclipsing helium CV, and in 2010 it became the one such system with a q value determined from eclipse timing. We note good agreement with the empirical $\varepsilon(q)$ relation: $q_{eclipse} = 0.041$ (2) (Copperwheat et al. 2011); $q_{\varepsilon} = 0.045$ (2).

GP Com & CE 315

These two systems have been observed only in quiescence and thus have no empirically-determined q values. They each have a spectroscopically-determined upper limit on q that is based on estimates of the effective surface temperature of the secondary (T_{eff}).

4.7 Summary and future work

Our updated diagram enhances a tentative pattern that helium CVs are evolving toward longer orbital period at a rate consistent with a model in which their secondaries are partially-degenerate Helium-stars: stars that were still undergoing core He burning at the onset of RLOF. There are roughly seven other He CVs that are likely candidates for superhumps, based on orbital periods shorter than 40 minutes and absorption spectra. A more complete $\varepsilon(P_{orb})$ diagram may illuminate the relative contributions of the proposed birth channels to the observed population.

4.8 Acknowledgements

Chapter 4 is, in part, a reproduction of material as it appears in Monthly Notices of the Royal Astronomical Society: Armstrong, E., Patterson, J., Kemp, J. 2012, MNRAS, 421, 2310. This dissertation author was the primary investigator and author of this paper.

REFERENCES

[1] Anderson, S. 2005, ApJ, 130, 2230

[2] Copperwheat, C. M., Marsh, T. R., Littlefair, S. P., et al. 2011, MNRAS, 410, 1113

[3] Faulkner 1972 – Faulkner & Flannery?

[4] Faulkner, J., Flannery, B. 1972, ApJ, 175, 79

[5] Knigge, C. 2006, MNRAS, 373, 484

[6] Marsh, T. R. 1999, MNRAS, 304, 443

[7] Murray, J. 2000, MNRAS, 314, L1

[8] Nather, R. E., Robinson, E. L., Stover, R. J. 1981, ApJ, 244, 269

[9] Nelemans, G., Yungelson, L. R., van der Sluys, M. V., Tout, C.A. 2010, MNRAS, 401, 1347

[10] Osaki, Y. 1989, PASJ, 41, 1005

[11] Patterson, J., Kemp, J., Harvey, D.A., et al. 2005, PASP, 117, 1204

[12] Patterson, J., Fried, R.E., Rea, R., et al. 2002, PASP, 114, 65

[13] Patterson, J. 2001, PASP, 113, 736

[14] Patterson, J. 2000, PASP, 112, 625

[15] Patterson, J., Kemp, J., Shambrook, A., et al. 1997, PASP, 109, 1100

[16] Pearson, K.J. 2007, MNRAS, 379, 183

[17] Poe, E.A., 1844, *Dream-land*. Philadelphia: Graham’s Lady’s and Gentleman’s Magazine

[18] Provencal, J. L., Winget, D. E., Nather, R. E., et al. 1997, ApJ, 480, 383

[19] Provencal, J.L., Winget, D. E., Nather, R. E, et al. 1995, ApJ, 445, 927

[20] Ramsay, G., Kotko, I., Barclay, T., et al. 2010, MNRAS, 407, 1819

[21] Roelofs, G.H.A., Groot, P.J., Marsh, T.R., Steeghs, D., Nelemans, G. 2006a, MNRAS, 365, 1109

[22] Roelofs, G. H. A., Groot, P. J., Nelemans, G., Marsh, T. R., Steeghs, D. 2006b, MNRAS, 371, 1231

[23] Roelofs, G. H. A., Groot, P. J., Nelemans, G., Marsh, T. R., Steeghs, D. 2007, MNRAS, 379, 176

[24] Ruiz, M. T., Rojo, P. M., Garay, G., Maza, J. 2001, ApJ, 552, 679

[25] Skillman, D.R., Patterson, J.P., Kemp, J., et al. 1999, PASP, 111, 1281

[26] Savonije, G., de Kool, M., Van Den Heuvel, E. 1986, Astron. Astrophys., 155, 51

[27] Smith, D.A., Dhillon, V.S. 1998, MNRAS, 301, 767

[28] Tsugawa, M., Osaki, Y. 1997, PASJ, 49, 75.

[29] Warner, B. 1975, MNRAS, 170, 219

[30] Wood, M.A., Casey, M.J., Garnavich, P.M., Haag, B. 2002, MNRAS, 334, 87

[31] Woudt, P. A., Warner, B. 2003, MNRAS, 345, 1266

[32] Zapolsky, H.S., Salpeter, E.E. 1969, ApJ, 158, 809

5 Pulse timing of the orbital period in AM CVn: *probing evolution in helium CVs*

"From the remotest period of antiquity to which the archives have reference, the hours have been regularly struck by the big bell ... Never was such a place for keeping the true time."

Poe; *The Devil in the Belfry* (1839)

5.1 Summary of project

We have monitored the helium CV AM Canum Venaticorum (AM CVn) over a 34-year baseline of photometry, to measure orbital period change ($\dot{\mathrm{P}}$) – with the aim of probing long-term evolution and hence the nature of the secondary in this system.

AM CVn was the first object identified as a helium CV. It has an orbital period around 18 minutes and appears to be in a continuous state of high mass accretion. A preliminary result, from the last 18 years of the light curve, does not indicate a lengthening P_{orb}, and might be consistent with evolution toward shorter P_{orb} governed by angular momentum loss due to GWR ($\dot{J}_{GWR}$). Possible interpretations of the result are: 1) AM CVn is still evolving toward a period minimum – and has a secondary that is not yet sufficiently degenerate to drive evolution in the opposite direction; 2) our baseline has not captured the secular evolution of P_{orb}.

We will explore possible problems with both our data and evolutionary models of He CVs.

5.2 AM CVn: the first-identified He CV

AM CVn is a blue object that was identified by Malmquist (1936) and Humanson & Zwicky (1947), who reported it at V = 14. It is extremely stable in magnitude (V = 14.15 ± 0.05 since discovery), and displays three persistent fundamental periodicities of 1011, 1028, and 1051s. Its spectrum shows strong helium lines in emission and no hydrogen.

Upon its discovery, a binary interpretation was not obvious. The most prominent signal in the power spectrum has a period of 525.6 s (hereafter “P_{525}”), and a harmonic at 1051 s (“P_{1051}”) is also present (Smak 1967). Solheim et al. (1984) found a second independent and persistent periodicity at 1011 s (“P_{1011}”). Two models were suggested: a binary system or pulsating white dwarf (Patterson & Sterner 1992). Both P_{1051} and P_{1011} were possible orbital periods in the binary scenario, but their lack of long-term stability rendered them unlikely candidates. Patterson & Sterner (1992) compiled and reviewed evidence for and against each model, including metal lines that implicated a binary. Those authors favored the binary scenario and, given AM CVn’s extremely stable magnitude, suggested that the system is experiencing a long-term high state.

When a weak and highly stable third periodicity of 1028 s was confirmed as P_{orb} (Harvey et al. 1998), the 1051s signal was subsequently interpreted as a beat between P_{orb} and the apsidal precession period of the disc (Skillman et al. 1999, hereafter “Sk99”). Strong evidence for this interpretation is the detection of the 13.4-hour apsidal precession period itself (Patterson et al. 1993). Sk99 further suggested that P_{1011} is a beat between P_{orb} and the retrograde precession period of a disc tilted with respect to the orbital plane.

Evidence for the binary nature of AM CVn continues to compile (e.g. Nelemans et al. 2001, Pearson et al. 2003, Roelofs et al. 2006, Wade et al. 2007), and the identification of the 1028-s signal as P_{orb} is firm. The interpretation of P_{1051} as a beat between P_{orb} and apsidal precession is strong, in light of the observed apsidal precession period and the fact that elliptical discs and superhumps have a history of association with high-state systems. The proposed interpretation of P_{1011} as a nodal superhump is not as convincing, both because the tilted-disc model is somewhat problematic for CVs, and because a retrograde precession period has not been detected in AM CVn above an amplitude upper limit of 0.04 mag (Patterson et al. 1993).

For simplicity, throughout this chapter we shall sometimes refer to the 525, 1011, 1028, and 1051-second signals as P_{525}, P_{1011}, P_{1028}, and P_{1051}, respectively.

5.3 Observations

Due to uncertainties in some of the early timings, we used only the last 18 years of the light curve (1992 – 2012) to find $\dot{P}$. Table 5.1 is the observing log of 1998 – 2012. Roughly 80% of the data were obtained by the CBA, in unfiltered light (~ 4000 – 9000 Å), which is acceptable when the star's signal does not show strong wavelength-dependent effects – as is the case for AM CVn (Krzeminski 1971). The remaining ~ 20% of the data were obtained at the 1.3-meter telescope at MDM, with a V filter. Integration times for CBA and MDM data ranged from 5 – 120 seconds, with a typical value of 57 seconds. Differential magnitudes were computed via circular apertures of 5 – 8 arcsecond radius.

Table 5.1: Observing log of AM CVn photometry over 13 years

Dates
1998 Mar 29 – Jun 25
1999 Feb 1 – Jun 9
2002 Mar 15 – Apr 8
2004 Apr 6 – May 3
2006 Mar 5 – Apr 22
2007 Jan 3 – Mar 31
2008 Feb 2 – Mar 25
2010 Mar 3 – Apr 13
2011 Jan 3 – Jun 15

Note: nightly hours of coverage averaged 4-5.

Observing seasons varied in density and duration. The years of best coverage were 1998, 1999, and 2011. Fig. 5.1 shows a typical run, consisting of nine nights during 2011, with 4 – 5-hour windows (over several longitudes) and ~ 10 – 20-hour gaps. Inset is a magnification of one window (~ 4.3 hours), which depicts AM CVn’s characteristic steady low-amplitude modulation.

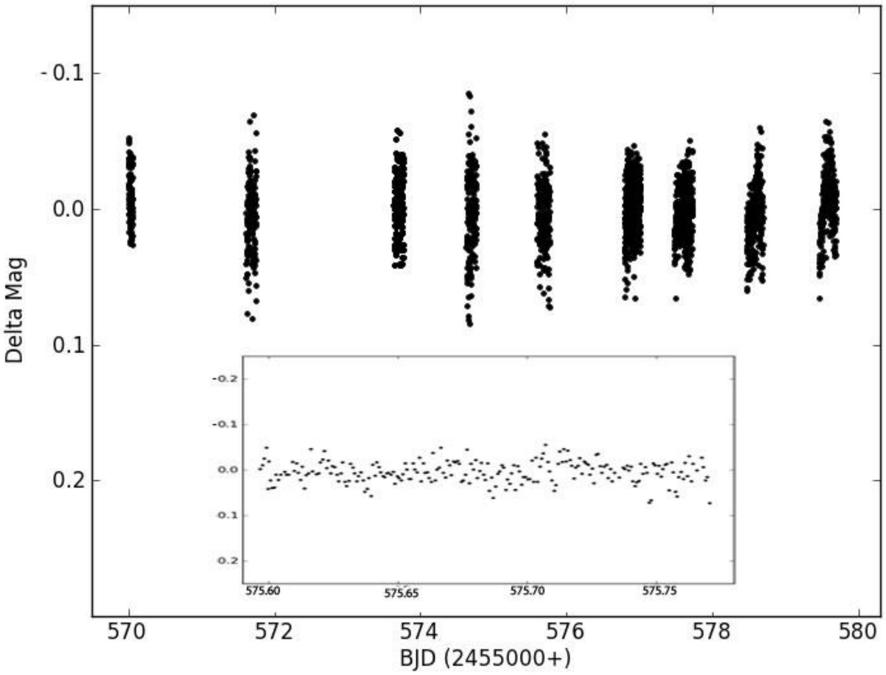

Fig. 5.1: Light curve of AM CVn during a run of nine nights during 2011. The time series is comprised of nine 4-5-hour windows sampled from different longitudes, separated by ~ 10-20-hour gaps. *Inset*: a magnification of one window of ~ 4.3 hours, which shows AM CVn’s characteristic steady modulation.

5.4 Analysis

5.4.1 The power spectrum

AM CVn's power spectrum was relatively constant over the 13-year baseline. The two orbital sidebands, P_{525} (the first harmonic of P_{1051}) and P_{1011}, were consistently present, and the latter rendered tedious the process of timing the orbital signal.

The top panel of Fig. 5.2 shows the power spectrum of the 9-day light curve of Fig. 5.1, which is representative of the power spectra used for the pulse timing study. Features of interest are noted. The strongest is P_{525}. Its amplitude throughout observations in all years was 0.010 (2) mag. The middle panel of Fig. 5.2 is the prewhitened power spectrum after removal of P_{525} from the light curve. The feature at ~ 85.4 c d^{-1} (1011.4 s) remains. The bottom panel is the power spectrum after the subsequent removal of the best-fit to P_{1011} from the first residuals light curve.

The P_{1011} feature was consistently weaker and less stable in amplitude than P_{525}, varying from 0.002 to 0.01 mag. We found P_{1011} to be almost always present, and typically at about half the amplitude of P_{525}. The orbital signal was also always present, with an amplitude that varied roughly within the same range as that of P_{1011}.

In order to view the orbital signal in the power spectrum, we usually had to subtract the sideband corresponding to P_{1011}. This process was often complicated by heavy aliasing: to obtain sufficient frequency resolution for separating P_{1011} from the orbital signal, we needed light curves of at least 5 days – and these baselines frequently included large gaps. The fundamental P_{1051} did not interfere: it was weaker and usually buried under P_{1011} and the orbital signal. Other harmonics were detected, but we shall not discuss them in this paper.

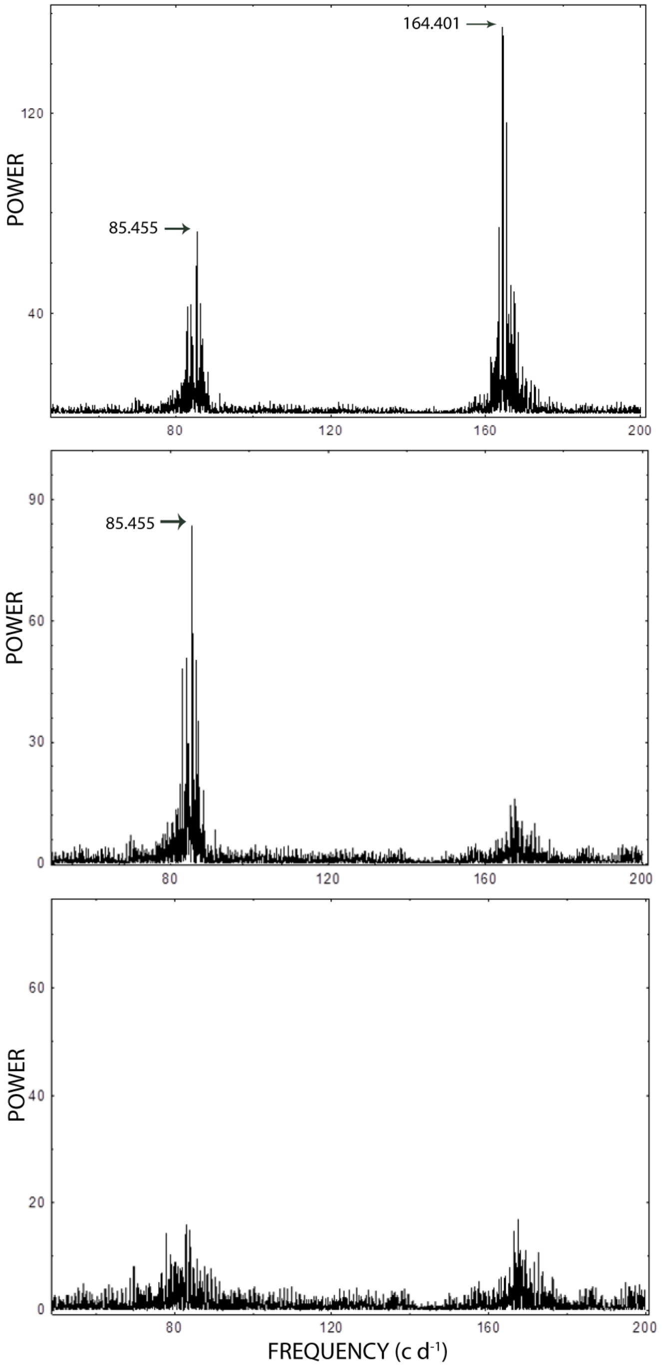

Fig. 5.2: *Top panel*: Power spectrum of the 9-day light curve of 2011, which is representative of the power spectra used for pulse timings. The signal around 164 c d^{-1} (525 s) is clear; a second feature appears around 85.4 c d^{-1} (1011 s). *Middle*: Prewhitened power spectrum after removal of the 525-s signal from the light curve, using the best-fit frequency of 164.401 c d^{-1}. *Bottom*: Power spectrum after subsequent removal of the 1011-s signal from the residuals, using the best-fit frequency of 85.455 c d^{-1}.

5.4.2 Pulse timing

We measured $\dot{P}$ via timings (§2.7) of minimum light of the orbital waveform relative to a test period of 1028.7322 sec, and plotting the accumulated discrepancy in phase over time.

Result

Table 5.2 shows the timings of minimum light of the orbital waveform over the 18-year baseline; Fig. 5.3 presents the O-C diagram based on these timings. The image is shown twice: once without models overlaid – so that the reader may examine the data with unbiased eyes, and once with linear (dotted) and two-degree polynomial least-squares (solid) fits. The latter, a shallow concave-down parabola, indicates *shortening* period: $\dot{P}$ = -3.8 x 10^{-13}.

Table 5.2: Timings of minimum light of the orbital waveform

HJD = 2,400,000+

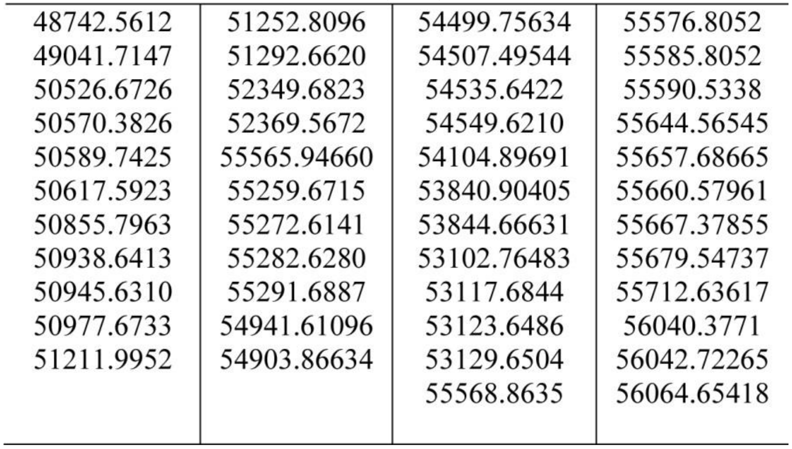

48742.5612	51252.8096	54499.75634	55576.8052
49041.7147	51292.6620	54507.49544	55585.8052
50526.6726	52349.6823	54535.6422	55590.5338
50570.3826	52369.5672	54549.6210	55644.56545
50589.7425	55565.94660	54104.89691	55657.68665
50617.5923	55259.6715	53840.90405	55660.57961
50855.7963	55272.6141	53844.66631	55667.37855
50938.6413	55282.6280	53102.76483	55679.54737
50945.6310	55291.6887	53117.6844	55712.63617
50977.6733	54941.61096	53123.6486	56040.3771
51211.9952	54903.86634	53129.6504	56042.72265
		55568.8635	56064.65418

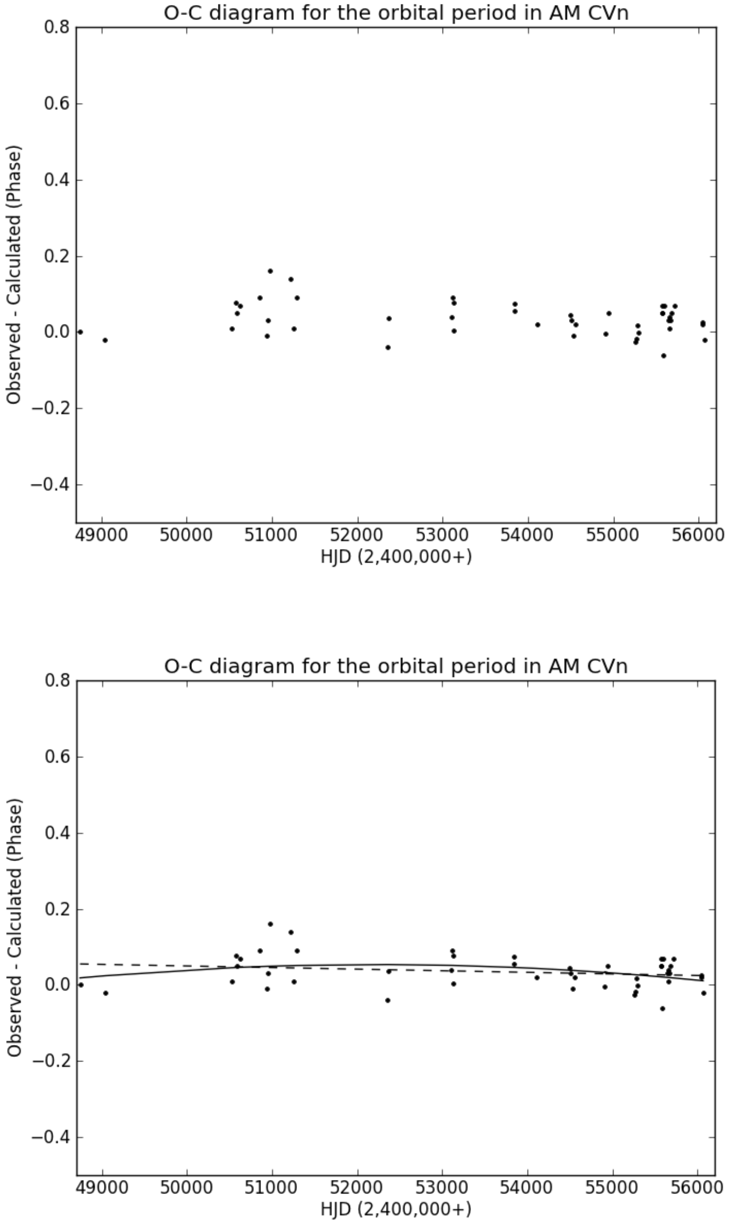

Fig. 5.3: O-C diagram for the orbital signal in AM CVn. *Top*: the data. *Bottom*: the data with linear (dotted) and two-degree polynomial least-squares (solid) fits. The quadratic fit yields: $\dot{P} = -3.8 \times 10^{-13}$.

Errors and uncertainty

The uncertainty in the data is best-represented by the scatter on the diagram. Errors on the points have not yet been placed, but they generally fall between ±0.04 – 0.08 in phase units, depending on the density and baseline of the lightcurve used for each timing. The low errors – yet relatively high scatter – reflect the impurity of our analysis process: battling alias structure and modeling the orbital sideband as a sinusoid. Thus, each point should be considered an average value and must be interpreted within the context of the entire distribution. Prior to setting errors on the points, we plan to repeat the sideband subtractions using fits to non-sinusoids, and determine whether this adjustment significantly changes the result.

To help the reader interpret this preliminary $\dot{P}$ estimate of ~ -10^{-12-13}, we offer a note for comparison: a concave-down parabola that allows for highest scatter (one that intersects the point highest on the y-axis, around HJD 51,000) yields: $\dot{P} = -4.0 \times 10^{-12}$ – one order of magnitude higher than the best-fit value. On the other hand, the best-fit parabola is discernible from the linear fit; or: a $\dot{P}$ value of -10^{-12-13} is significantly different from zero.

5.5 Discussion

5.5.1 Interpretation of the AM CVn observation

Does the value of $\dot{P} \sim -10^{-12-13}$ (from the quadratic fit) represent the secular evolution of orbital period? Perhaps instead we have witnessed a transient evolutionary stage of a secondary that is settling unsmoothly into a degenerate state, with outer layers still burning. We shall not claim otherwise, especially in light of the scatter on the O-C diagram. We note, however, that a value of $\dot{P}$ around this value appears to be consistent with evolution governed by $\dot{J}_{GWR}$, for a system with a P_{orb} of 10^3 seconds (Paczynski 1967). Perhaps the most important outcome of this O-C diagram is a reminder that the commonly-accepted picture that He CVs contain degenerate secondaries merits an examination.

5.5.2 Timings of $\dot{P}$ in two other He CVs

Before examining the evolutionary models, we consider the AM CVn P_{orb} timing in light of previous measurements. Direct timings of $\dot{P}$ have been made for two[1] other helium CVs. One is ES Ceti ($P_{orb} \sim 10.3$ min; (Espaillat et al. 2005)), for which a 9-year photometry baseline demonstrated no evidence for period evolution ($|\dot{P}| \cong 10^{-11}$; Copperwheat et al. 2011). The second object, HM Cancri (HM Cnc), has the shortest orbital period of a helium CV: ~ 5.4 min. Several independent photometry campaigns, each of 3-4-year duration, have yielded a negative value for $\dot{P}$ in HM Cnc, around -10^{-11} (Hakala et al. 2003; Israel et al. 2004). As is the case for our AM CVn result, the value for HM Cnc appears to be consistent[2] with orbital period shortening governed by $\dot{J}_{GWR}$ (for a system with $P_{orb} \sim 10^2$ sec (Paczynski 1967)). (Some observers consider the identification of HM Cnc as a He CV to be problematic. For details, see Appendix G).

5.5.3 What should we expect?

Birth channels

If we take as our clues a helium-rich spectrum and short P_{orb} (and accept the general model of an accreting binary via RLOF), then what might we expect the secondaries in He CVs be? There is a range of possibilities here, which is primarily set by the system's "birth

---

[1] A third object, V407 Vulpeculae (V407 Vul), has been identified as a He CV with $P_{orb} \sim 9$ minutes and $\dot{P} \sim -10^{-11}$ (Strohmayer 2004, Ramsay et al. 2005) – which is a value consistent with evolution via $\dot{J}_{GWR}$ at this orbital period. V407 Vul's credentials as a He CV, however, are lacking. Most critically: its spectrum is featureless. For details, see Appendix G.

[2] The "appears to be" qualifier acknowledges that Paczynski's (1967) estimates of $\dot{P}$ for a binary at a given P_{orb} are systematically two orders of magnitude faster than those found for AM CVn and HM Cnc, given their orbital periods. That is: for $P_{orb} \sim 10^3$ s (AM CVn), $\dot{P} \sim -10^{-11}$, and for $P_{orb} \sim 10^2$ s (HM Cnc), $\dot{P} \sim -10^{-9}$. But these estimates do not account for the competing effect of mass transfer, and they assume that each component of the binary is ~ 1 solar mass. The general picture is of strengthening GWR effects as a system's orbit decays.

channel": the mass and evolutionary state of the secondary at core He ignition, and again at RLOF.

Birth channels that have been identified include: "white dwarf channel" and "He star channel" (e.g. Nelemans et al. 2001a). In the former picture, the secondary is already fully-degenerate at RLOF. This class then includes i) secondaries that were never sufficiently massive to ignite He and were fully-degenerate "He WDs" at RLOF; ii) secondaries that had completed core He burning and become fully-degenerate He/C WDs at RLOF. Within this picture, however, it might be difficult to explain the observed rates of mass transfer. That is: if a degenerate object can be regarded as a solid without an appreciable atmosphere, then why are the $\dot{M}$s so high? In the "He star channel", the secondary is at some (unspecified) stage of He burning at RLOF.

A third channel, the "H star channel", has been proposed, in which a late-stage H CV evolves into a He CV (Podsiadlowski et al. 2003). This does not appear to be a likely trajectory. For details of each channel, see Appendix F.

All three categories are broad: they must permit a range of initial secondary masses, compositions, and core temperatures, mass transfer rates, P_{orb}s, and times between core He ignition and RLOF. The extent of burning in outer layers and the mass transfer process itself are also likely to affect evolution in all cases. Finally, the first two routes appear to require the survival of two CE phases.

We note recent indications that spectroscopic analysis of chemical composition might provide a method of discrimination among these birth channels in individual systems (Nelemans et al. 2010). This work shows promise of indicating the relative contributions from each channel to the observed population.

Do **degenerate stars expand upon mass loss?**

Does there exist convincing observational evidence that the theory of degenerate matter can describe the behavior of stars? Yes, it appears so. The distribution in mass-radius space of isolated white dwarfs with known parallaxes is consistent with the prediction that a sphere of degenerate matter will increase in radius upon mass loss (e.g. Bergeron et al. 1990).

Is the secondary in an He CV degenerate?

From their spectra, He CV secondaries have evolved beyond main-sequence burning – a picture that is supported by the short P_{orb}s of the systems, which indicate secondary masses systematically lower than solar ($< \sim 0.3M_{\odot}$). It remains to be demonstrated, however, that such an object can be characterized as degenerate.

5.5.4 Evolutionary models

The period-minimum estimate of 10 minutes

Savonije et al. (1986) calculated a period minimum of 10 minutes for He CVs born via the "He star" channel. The derivation goes as follows.

From the requirement that the rate of change of R_2 equal the rate of change of the average Roche lobe radius of the secondary, and with Kepler's law, we obtain a simple relationship between the average density of the secondary $<\rho_2>$ and P_{orb}:

$$\langle\rho_2\rangle \sim \frac{M_2}{(R_2)^3} \sim \frac{1}{P_{orb}^2} \qquad 5.1$$

(Paczynski 1967). Then, using considerations of Roche geometry and angular momentum (derived in §1.2.6.2 and §1.2.6.3, respectively):

$$\frac{\dot{P}}{P} = \frac{3\zeta - 1}{2}\frac{\dot{M}_2}{M_2} \qquad 5.2$$

where $\zeta = \frac{\mathrm{dln(R2)}}{\mathrm{dln(M2)}}$ and $\dot{\mathrm{J}}$ is contained in the $\dot{\mathrm{M}}_2$ term. A turnaround in the direction of P occurs at $\zeta = 1/3$.

This turnaround point occurs sometime after the thermal pressure in the core of the secondary equals the pressure due to degenerate electrons; that is: after the inversion of the secondary's mass-radius relation. Fig. 5.4 shows the trajectory of a secondary with an initial mass of $0.6M_\odot$ as it traverses this point, which is indicated by the straight line (Savonije et al. 1986). The graph is a log-log plot of core density (ρ_c) versus core temperature (T_c) – the defining consideration for degeneracy. The star's mass-radius relation inverts shortly before it reaches $0.3M_\odot$ – around an orbital period of ten minutes.

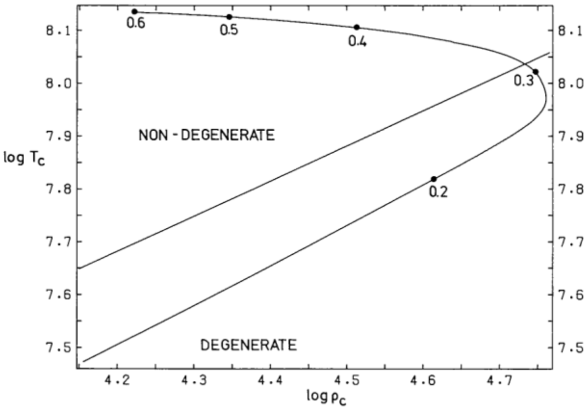

Fig. 5.4: Evolutionary path of secondary in ρ_{core}-T_{core} space, with mass in solar units. *Straight line*: "turnaround" of $M_2(R_2)$, where the pressure of degenerate electrons equals the thermal (Maxwell-Boltzmann) pressure (*Savonije et al. 1986*).

Estimates of q determined both spectroscopically and via the $\varepsilon(P_{orb})$ relation indicate that the secondary in AM CVn has evolved to about an order of magnitude below this value.

But: *many assumptions* underlie the secondary's trajectory in $\rho_c(T_c)$ space and the location at which it intersects the solid line. The path calculated by Savonije et al. (1986) allowed for no range in initial conditions. Rather, they assumed a single value of secondary mass, composition, core temperature, birth channel, P_{orb}, and mass transfer rate at core He ignition, and the time between core He ignition and RLOF.

The most complete picture to date

It is this author's impression that the model of Deloye et al. (2005) incorporates the most thorough considerations to date. They model evolution based on three timescales:

- τ_{j} = timescale of evolution via angular momentum loss;
- $\tau_{\mathrm{Kelvin-Helmholtz}}$: thermal timescale, which is sensitive to T_{core}, which in turn depends on the CV's formation channel and past evolution;
- τ_{ev} = time since the start of core He burning.

All three timescales depend on the binary's orbital period and the secondary mass, chemical composition, and T_c at the onset of burning and again at Roche lobe overflow (RLOF).

Deloye et al. (2005) charted the M(R) relations of secondaries in He CVs that have evolved via the "He star channel", in terms of initial core temperature (T_c), based on the relative values of these timescales. Fig. 5.5 shows a set of isotherms for their He WD models with $\log(T_c/K)$ between 4.0 and 7.5, at intervals of 0.5. The lower dashed line shows the T=0 Zapolsky & Salpeter (1969) He WD relation; the upper dashed line shows the M(R) relation for the He-star channel used by Nelemans et al. (2001b). The dotted lines show the Roche-lobe-filling solutions at the P_{orb} of the indicated systems.

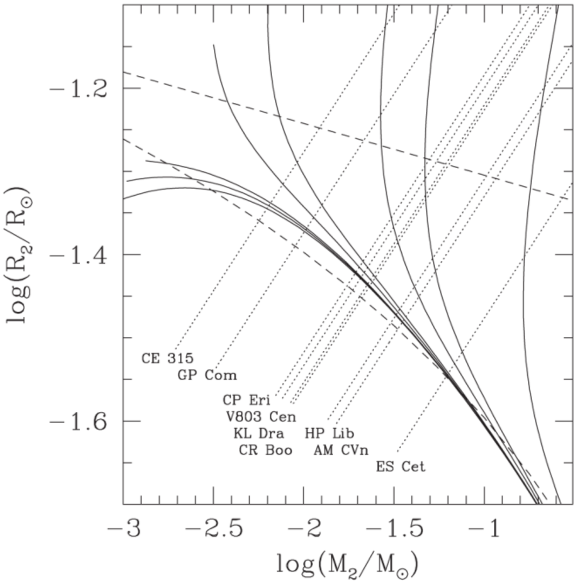

Fig. 5.5: Comparison between the He WD models and the M(R) relations currently used in the literature. Solid lines show a set of isotherms for the He WD models with $\log(T_c/K)$ between 4.0 and 7.5 at intervals of 0.5. The lower dashed line shows the T=0 Zapolsky & Salpeter (1969) He WD relation. The upper dashed line shows the M(R) relation for the He-star channel used by Nelemans et al. (2001b). The dotted lines show the Roche-lobe-filling solutions at the P_{orb} of the indicated systems.

These authors have not applied this analysis to the He WD channel, nor have they allowed for burning of outer layers or the possible lifting of degeneracy pressure due to the mass transfer process. They have also not compared the time-varying strengths of $\dot{J}_{GWR}$ versus angular momentum *gain* via secondary expansion ("$\dot{J}_{\dot{M}}$"), to derive a range of period minima.

For other modeling, see Nelemans et al. (2001b) and Smith & Dhillon (1998).

Double CE?

Finally, we recall that the He-WD and He-star birth channels require the binary to survive two CE phases. There appears to be little agreement in the literature regarding how to reproduce such a feat (e.g. Webbink 2008).

5.6 Summary and future work

The pulse timing of the orbital period in AM CVn does not indicate period lengthening, and a quadratic fit to the data yields a negative value for $\dot{P}$, which appears to be consistent with evolution driven primarily by $\dot{J}_{GWR}$. We suspect that we are seeing the secular evolution of a system that has yet to reach a period minimum. Given the contaminating effects introduced by our analysis (which is reflected by the scatter on the O-C diagram), however, we do not proclaim this conclusion loudly.

We shall continue AM CVn's time series. There also exist earlier timings (from 1978 and 1984) that we have not included in analysis, due to uncertainties in the start times of the observations. A re-examination of these data, however, might still prove valuable. We will also repeat our analysis by fitting non-sinusoids to modulations during the process of signal subtraction. Finally, we will continue light curves on the ~ 4 other He CVs with orbital periods shorter than ~ 26 minutes; each of which requires 6-8 more years of photometry for the purpose of pulse timing.

The greatest value of our timing result for AM CVn may well be simply that it startles us. In light of the $\varepsilon(P_{orb})$ plot of Fig. 4.1 and the general expectation that He CV secondaries are degenerate, it is a surprising result. Yet it incited us to re-examine that expectation – and recognize that it does not rest upon a firm foundation. A complete model will include a range of initial conditions within the secondary, the relative contributions of time-varying $\dot{J}_{GWR}$ and $\dot{J}_{\dot{M}}$, other perturbing effects such as shell burning and mass transfer, and a successful simulation of events leading to birth.

5.7 Acknowledgements

Chapter 5, in part, is being prepared for submission for publication, with the following authors: Armstrong, E., Patterson, J. This dissertation author was the primary investigator and author of the material.

REFERENCES

[1] Bergeron, P., Saffer, R., Liebert, J. 1990, ASPC, 11, 513

[2] Bildsten, L., Chakrabarty, D., Chiu, J., Finger, M., Koh, D., Nelson, R., Prince, T., Rubin, B., et al., 1997, ApJ, 113, 2

[3] Cherepaschuk 2002, Space Sci. Rev., 102, 23

[4] Deeter, J., Crosa, L., Gerend, D., Boynton, P.E., 1976, ApJ, 206, 861

[5] Deloye, C., Bildsten, L., Nelemans, G. 2005, Ap J, 624, 934

[6] Espaillat, C., Patterson, J., Warner, B., Woudt, P. 2005, PASP, 117, 189

[7] Hakala, P, Ramsay, G., Wu, K., Hjalmarsdotter, L., Jarvinen, S., Jarvinen, A., Cropper, M. 2003, MNRAS, 343, L10

[8] Harvey, Skillman, D.R., Kemp, J., Patterson, J., Vanmunster, T., Fried, R.E., Retter, A., 1998, ApJ, 493, L105

[9] Humanson, M.L., Zwicky, F., 1947, ApJ, 105, 85

[10] Iping, R.C., Petterson, J.A., 1990, A&A, 239, 221I

[11] Israel, G. L., Covino, S., Dall'Osso, S., et al. 2004, Mem. S.A. It. Suppl., 5, 148

[12] Jurua, E., Charles, P.A., Still, M., Meintjes, P.J., 2011, MNRAS, 418, 437

[13] Katz, J., 1981, A&A Lett., 95, L15

[14] Kemp, J.C., Barbour, M.S., Arbabi, M., Leibowitz, E.M., Mazeh, T., 1980, ApJ Lett., 238, L133

[15] Kemp, J.C., Henson, G.D., Kraus, D.J., Carroll, L.C., Beardlsey, I.S., 1986, ApJ, 305, 805

[16] Knigge, C., Baraffe, I., Patterson, J. 2011, Ap J S, 194, 28

[17] Kotze, M., Charles, P. 2012, MNRAS, 420, 1575K

[18] Krezeminski, W., 1971, in IAU Colloq. 15, New Directions and New Frontiers in Variable Star Research, ed. W. Strohmeier (Veroff. Remeis-Sternw. Bamberg, Vol. 9, No. 100), 78

[19] Lang, F.L., Levine, A.M., Bautz, M., Hauskins, S.H., Primini, F.A., Lewin, W.H.G., 1981, ApJ, 246, L21

[20] Lubow, S.H., 1992, ApJ, 398, 525

[21] Lubow, S.H., Ogilvie, G.I., 2000, ApJ, 538, 326

[22] Malmquist, K. 1936, Stockholms Observatoriums Annaler, 12, 7

[23] Margon, B., Grandi, S.A., Downes, R.A., 1980, ApJ, 241, 306

[24] Montgomery, M.M., 2009a, MNRAS, 394, 1897 – list of binaries with P-

[25] Montgomery, M.M., 2009b, ApJ, 705, 603

[26] Montgomery, M.M., Martin, E.L., 2010, ApJ, 722, 989

[27] Montgomery, M.M., 2012, ApJ, 745L, 25M

[28] Nelemans, G., Steeghs, D., Groot, P.J., 2001a, MNRAS, 326, 621N

[29] Nelemans, G., Zwart, S., Verbunt, F., Yungelson, L. 2001b, A&A, 368, 949

[30] Nelemans, G., Yungelson, L., van der Sluys, M., Tout, C. 2010, MNRAS, 401, 1347

[31] Ogelman, H., Kahabka, P., Pietsch, W., Trumper, J., Voges, W., 1985, Space Sci. Rev., 40, 347

[32] Ogelman, H., 1987, A&A, 172, 79

[33] Osaki, Y. 1989, PASJ, 41, 1005

[34] Paczynski, B. 1967, Acta Astron., 17, 287

[35] Patterson, J., Sterner, E., 1992, ApJ, 384, 234

[36] Patterson, J., Halpern, J., Shambrook, A., 1993, ApJ, 419, 803

[37] Patterson, J., Kemp, J., Saad, J., Skillman, D.R., Harvey, D., Fried, R., Thorstensen, J., Ashley, R., 1997, PASP, 109, 468

[38] Patterson, J., Thorstensen, J.R., Fried, R., Skillman, D.R., Cook, L.M., Jensen, L., 2001, PASP, 113, 72

[39] Patterson, J., Fenton, W.H., Thorstensen, J.R., Harvey, D.A., Skillman, D.A., Fried, R.E., Monard, B., O'Donoghue, D., Beshore, E., et al., 2002, PASP, 114, 1364

[40] Paul, B., Kitamoto, S., 2002, JApA, 23, 33P

[41] Pearson, K.J. 2003, MNRAS, 346L, 21P

[42] Petterson, J.A., 1977a, ApJ, 214, 550

[43] Petterson, J.A., 1977b, ApJ, 216, 827

[44] Podsiadlowski, P., Han, Z., Rappaport, S., 2003, MNRAS, 340, 1214

[45] Poe, E.A., 1839, *The Devil in the Belfry*. Philadelphia: Saturday Chronicle and Mirror of the Times

[46] Pringle, J.E., 1996, MNRAS, 281, 357

[47] Roelofs, G.H.A., Groot, P.J., Nelemans, G., Marsh, T.R., Steeghs, D., 2006, MNRAS, 371, 1231

[48] Savonije, G., de Kool, M., Van Den Heuvel, E. 1986, Astron. Astrophys. 155, 51

[49] Scargle, J., 1982, ApJ, 263, 835

[50] Schandl, S., Meyer, F., 1994, A&A, 289, 149S

[51] Skillman, D.R., 1981, S&T, 61, 71

[52] Skillman, D.R., 1993, S&T, 85, 83

[53] Skillman, D.R., Patterson, J., 1993, ApJ, 417, 298S

[54] Skillman, D.R., Patterson, J., Kemp, J., Harvey, D.A., Fried, R.E., Retter, A., Lipkin, Y., Vanmunster, T., 1999, PASP, 111, 1281 (Sk99)

[55] Smak, J., 1967, Acta Astron., 17, 255

[56] Smak, J., 2009a, AA, 59, 419

[57] Smak, J., 2009b, AA, 59, 121

[58] Smith, V., Dhillon, D. 1998, MNRAS, 301, 767

[59] Solheim, J.-E., Robinson, E.L., Nather, R.E., Kepler, S.O., 1984, A&A, 135, 1

[60] Vanmunster, T., 1999, PASP, 111, 1281 (Sk99)

[61] Wade, R.A., Eracleous, M., Flohic, H., 2007, AJ, 134, 1740

[62] Webbink, R. 2008, *Short-period Binary Stars: Observations, Analyses, and Results*, ed. E.F. Milone, D.a. Leahy, D.W. Hobbill (New York: Springer), 233

[63] Whitehurst, R. 1988, MNRAS, 232, 35

[64] Wojdowski, P., Clark, G.W., Levine, A.M., 1998, ApJ, 502, 253

[65] Wood, M.A., Burke, C.J., 2007, ApJ, 661, 1042

[66] Wood, M.A.; Still, M.D.; Howell, S.B.; Cannizzo, J.K.; Smale, A.P., 2011, ApJ, 741, 105

6 The orbital sidebands in AM CVn: *examining the behavior of tilted discs*

“The propelling principle, or power, was here ... applied to interrupted surfaces, or vanes, put in revolution.”
Poe; *The Balloon Hoax* (1844)

6.1 Summary of project

As discussed in Chapter 5, AM CVn displays two prominent, persistent sidebands of its orbital signal: one a few percent slower than the orbit (P = 1051 s), and one a few percent faster (P = 1011 s). The first is a positive superhump within the context of §1.2.3. Prior to this study, the origin of the second sideband, a “negative superhump”, had not been firmly identified. We have analyzed these signals to investigate two questions: 1) Is the negative superhump likely to originate in the disc? 2) Is there a correlation between the periods or amplitudes of the positive and negative superhumps?

The answer to question #1, based on the signals’ persistence and stability relative to the established disc signal (P_{1051}), and its lack of long-term period evolution, is most likely: yes. Specifically: the signal may correspond to a beat between the orbit and retrograde precession of the line of nodes of a disc tilted with respect to the orbital plane. The answer to Question #2 is: No, which indicates that behaviors occurring at different radii in the disc are not strongly coupled.

For simplicity, the modulations with periods of 525, 1051, and 1011s will hereafter be denoted: P_{525}, P_{1051}, and P_{1011}, respectively.

6.2 Observations

For the sideband study we used only the final 13 years of the 34-year light curve, due to the higher density of coverage during that period. All of these dates are listed in Table 5.1. For details of observations, see §5.3.

6.3 Analysis

6.3.1 The waveforms and power spectrum

To study the coherence of P_{1011}, we created an O-C diagram (§2.7) for each season. For comparison, we did the same for P_{525}. We used P_{525} as a proxy for the fundamental P_{1051}, because P_{525} is strong and unambiguous, and because our results for 1998 and 1999 are directly comparable to those of Skillman et al. (1999) (hereafter “Sk99”) as a confidence check. The waveforms of both signals, shown in Fig. 6.1, are approximate sinusoids, which justified our method of least-squares fitting using to a two-parameter wave of phase and amplitude, with the period held fixed.

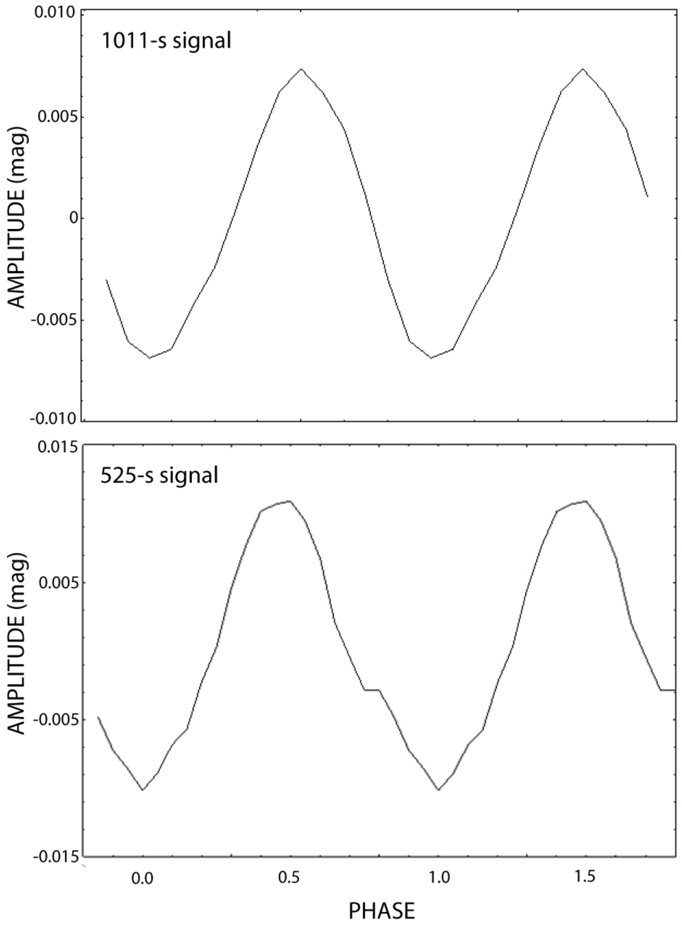

Fig. 6.1: Waveforms from the nine-day 2011 light curve, of a: the 1011-s signal, and b: 525-s signal. Both are approximate sinusoids.

To obtain sufficient points on each O-C diagram to create a discernible pattern, we divided each season's light curve into at least eight subsections. For each short light curve, we timed P_{1011} and P_{525} relative to test periods of 1011.35 s and 525.61s, respectively. The latter value was established by the pulse timings of Sk99. The 1011.35s value was estimated via results of preliminary testing of our data.

Timing P_{525} was a straightforward task. P_{1011}, however, was weaker and sometimes competed with the orbital signal. Thus we subtracted the 525-s signal from the light curve, and sometimes the orbital signal as well, and used the prewhitened power spectrum to time

P_{1011}. During our observations, P_{1051} never appeared strongly enough to require removal. For details of power spectrum analysis, see §5.4.1.

6.3.2 Pulse timing

Caveat: Data quality

For precise measurements such as period determination and waveform characterization, we generally use light curves consisting of at least a 4-day baseline and 20% coverage. The amount of data we accumulated for the AM CVn pulse timing study, however, was at times insufficient to permit adherence to this ideal. To obtain at least eight points on the diagram for each season, we sometimes divided light curves into sections that are too short (~ 2 days) and/or sparse (~ 15% coverage) for the purposes of making precision measurements. Fortunately, a pulse timing study weathers low data quality quite well, as we seek a pattern rather than a single number. Furthermore, the error is well reflected by the degree of scatter in the pattern.

The sacrifice of quality did not significantly affect the strong 525-s signal, but did occasionally cast doubt upon our detection of the weaker 1011-s signal. Hence we required the following condition in order to accept each measurement as a detection of P_{1011}: the amplitude of the best-fit sinusoid must be greater than 0.002 mag.

Results

Tables 6.1 and 6.2 contain the times of maximum light of the waveforms of P_{1011} and P_{525}, respectively. Fig. 6.2 shows the O-C diagrams for all years, which were constructed from the timings via Eq. 2.12. Note that the x-axes are scaled to normalize for baseline of observations. To avoid cycle count errors of ±1 for questionable points, we checked the period values derived from the power spectra themselves.

Table 6.1: Timings of maximum light of the 1011-s signal waveform.

BJD 2,400,000+					
50901.7518	51211.9908	*52366.6589*	53837.7407	54508.4002	55580.7903
50912.7557	51252.8124	*52367.6794*	53842.6089	54512.5102	55585.7893
50915.6252	51262.7749	*52368.6979*	53843.6878	54523.4543	55590.0036
50918.8994	51266.6516	*52369.5833*	53844.6837	54529.6463	55638.5070
50927.6199	51274.5587	53102.7570	53846.6150	*54540.6867*	55647.7787
50932.5488	51285.5132	53102.9443	54104.8926	55259.6691	55660.7848
50939.6195	51294.2566	53104.7713	54105.9119	55266.7628	55664.8449
50943.6216	51295.2630	53112.7771	54106.0286	55272.6160	55665.7120
50944.6749	51297.7694	53119.6245	54171.5260	55275.6712	55667.5739
50947.5550	51327.2558	53120.8771	54174.5227	55282.6237	55668.5800
50948.5385	51331.7744	53123.8161	54177.0052	55287.7509	55669.7967
50949.5453	*52349.6700*	53126.6825	54178.9011	55293.6621	55670.4178
50951.5578	*52357.4608*	53128.3560	54185.6202	55299.4210	55671.4948
50970.6847	*52357.4584*	53829.6430	54188.4322	55565.9793	55712.6291
50975.6724	*52362.3312*	53832.3671	54499.7389	55568.7649	55719.6520
50980.6275	*52364.6698*	53835.7762	54506.4814	55569.9970	55722.7213
					55725.6251

Note: Results for which the amplitude was less than 0.002 mag are italicized; these were not used in constructing the O-C diagram of Fig. 6.2.

Table 6.2: Timings of maximum light of the 525-s signal waveform

BJD 2,400,000+					
50901.7480	51211.9862	52366.6558	53837.7396	54508.4010	55580.7887
50912.7591	51252.8075	52367.6718	53842.6129	54512.5078	55585.7942
50915.6245	51262.7779	52368.7004	53843.6823	54523.4537	55589.9975
50918.8948	51266.6538	52369.5769	53844.6862	54529.6477	55638.5045
50927.6245	51274.5622	53102.7536	53846.6203	54540.6852	55647.7809
50932.5525	51285.5186	53102.9481	54104.8930	55259.6633	55660.7919
50939.6223	51294.2610	53104.7726	54105.9090	55266.7684	55664.8485
50943.6229	51295.2596	53112.7779	54106.0304	55272.6145	55665.7060
50944.6810	51297.7704	53119.6215	54171.5231	55275.6682	55667.5792
50947.5586	51327.2556	53120.8746	54174.5283	55282.6211	55668.5768
50948.5447	51331.7750	53123.8188	54176.9980	55287.7553	55669.7998
50949.5473	52349.6759	53126.6837	54178.9019	55293.6686	55670.4205
50951.5547	52357.4638	53128.3625	54185.6181	55299.4179	55671.4969
50970.6853	52357.4569	53829.6366	54188.4288	55565.9826	55712.6288
50975.6732	52362.3367	53832.3678	54499.7437	55568.7685	55719.6548
50980.6309	52364.6667	53835.7805	54506.4845	55569.9981	55722.7267
					55725.6284

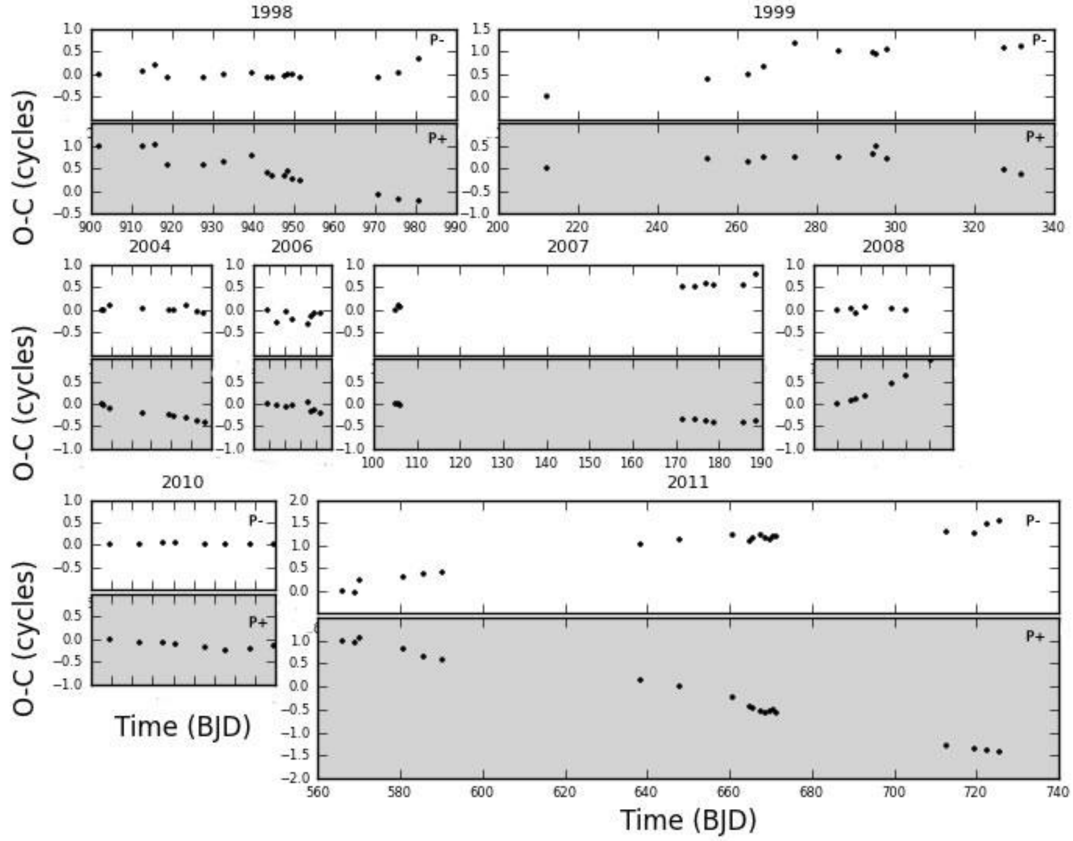

Fig. 6.2: Seasonal O-C diagrams for the 1011-s signal (white cells) and 525-s signal (shaded cells), relative to test periods of 1011.35 s and 525.61 s, respectively.

For P_{1011} and P_{525}, Table 6.3 tabulates seasonal period values from linear fits to the slope on each O-C diagram, and weighted mean period and period variation. The years 1999 and 2011 showed mild evidence for period change, and we calculated $\dot{P}$ from a quadratic fit.

We checked the P_{525} timings of 1998 and 1999 with those of Sk99. Results for 1998 are consistent: our diagram represents roughly the last half of data in Fig. 2 of Sk99. Results of 1999 are inconsistent with Sk99, in which those authors found that $\dot{P}$ changes from positive to negative during the same baseline. One of those authors (Patterson) has suggested that the cycle count of their final few points was erroneous (private communication); however,

Table 6.3: Seasonal period values of P_{1011} and P_{525}, from linear fits to the slope on each O-C diagram, and weighted mean period and period variation.

Year	*Baseline (d)*	*P_{1011} relative to P_{test} of 1011.35 s*				*P_{525} relative to P_{test} of 525.61 s*			
		P (s)	$\dot{P}$	<P> (s)	δP/P	P (s)	$\dot{P}$	<P> (s)	δP/P
1998	79	1011.377	0	1011.428	9 x 10^{-5}	525.562	0	525.587	1.21 x 10^{-4}
1999	120	1011.464	-2.26 x 10^{-8}			525.608	-4.93 x 10^{-9}		
2002	24	-	-			-	-		
2004	26	1011.319	0			525.560	0		
2006	17	1011.298	0			525.570	0		
2007	84	1011.449	0			525.597	0		
2008	30	1011.350	0			525.687	0		
2010	40	1011.356	0			525.600	0		
2011	160	1011.480	-1.12 x 10^{-8}			525.563	0		

that correction would not account for our disagreement. Adjusting the points in question would yield $\dot{P} > 0$ for the Sk99 result. Sk99 used a different test period (525.60 s), but a difference of 0.01 s would not significantly affect the curvature on the diagram. We have been unable to pinpoint the origin of our disagreement.

Regarding our results, we make several notes.

- *Mean values:*

  $\langle P_{1011} \rangle$ = 1011.43s; $\langle P_{525} \rangle$ = 525.59 s.

- *Stability:*

  $\frac{\delta P_{1011}}{P_{1011}} = 9 \times 10^{-5}$; $\frac{\delta P_{525}}{P_{525}} = 1.21 \times 10^{-4}$ over 13 yrs.

- *Period evolution:*

  There is no evidence for long-term period evolution of either signal; rather, they each appear to be wandering about a mean value, which is characteristic of permanent superhumps of disc origin. The only reasonably likely non-zero $\dot{P}$ detections are for the 1999 season: $\dot{P}_{1011}$ = -2.26 x 10^{-8} and $\dot{P}_{525}$ = -4.93 x 10^{-9}, and for 2011: $\dot{P}_{1011}$ = -1.12 x 10^{-8} (and $\dot{P}_{525}$ = 0).

- *Persistence:*

  P_{525} was detected during every observation. The only non-detections of P_{1011} above 0.002 mag occurred during the full 24 days of the 2002 season and final 4 days of the 40-d 2008 season.

6.3.3 Correlations among periods and amplitudes

Period trends

Table 6.4 shows the Spearman rank coefficients (r_s) and p-values for the respective trends on the O-C diagram of each signal's period, in each year. The p-value roughly gives the probability of uncorrelated data sets producing a Spearman relation at least as extreme as the one computed. R_s varies between -0.9 and +0.47 over the 13-year baseline (the weighted mean r_s = -0.39), with no discernible pattern.

Table 6.4: Spearman rank coefficients (r_s) and p-values for the period evolution of the two superhumps (P_{1011} and P_{525}) in each year.

Year	r_s	*p-value*
1998	0.17	0.52
1999	-0.10	0.77
2004	0.47	0.21
2006	-0.26	0.53
2007	-0.80	0.01
2008	-0.09	0.87
2010	-0.26	0.53
2011	-0.92	10^{-8}

Note: The p-value roughly gives the probability of uncorrelated data sets producing a Spearman relation at least as extreme as the one computed.

Amplitude trends

We found no convincing evidence for a correlation between the amplitudes of P_{1011} and P_{525} (r_s 0.21; p-value = 0.38) or the amplitudes of P_{1011} and P_{orb} ($r_s = 0.23$; p-value = 0.34).

6.4 Negative superhump modulations in CVs and LMXBs

Roughly 30 CVs and LMXBs have displayed negative superhumps that have persisted on timescales longer than weeks (see Table 2 of Montgomery 2009b for a comprehensive list). The favored model for their origin invokes an accretion disc that is tilted with respect to the orbital plane. This "tilted-disc model" is fairly well accepted for the few CVs in which the signal displays the low coherence that is characteristic of a disc origin, and in which a superorbital period that can be identified as the underlying precession period has also been detected. This model was developed for LMXBs, where irradiation by the primary neutron star can effect disc tilt. Well-studied examples include Her X-1 and SS 433[1]. This model will be examined in detail in Chapter 7.

6.4.1 Interpreting the 1011-s signal

The 1011-s signal demonstrates no evolution in period, but rather wanders about a mean value – which is characteristic of superhumps originating in the disc. The stability of P_{1011} is comparable to that of the period with a well-established disc origin (P_{525}): in both

---

[1] In Her X-1, superorbital and orbital periods are consistently detected via shifting emission lines, at 35 days and 1.7 d, respectively. Optical photometric variations have shown a 1.62-d period corresponding to an orbital sideband (Deeter et al. 1976; Jurua et al. 2011.) SS 433 shows a persistent superorbital period of 162.5 d, both from shifting emission lines and from a particularly well-resolved power spectrum feature that emanates from relativistic jets (Cherepashchuk 2002). Several photometric periods have been reported that may correspond to sidebands of the 13.1-d orbital period (Kemp et al. 1980, Kemp et al. 1986, Katz 1981.) Other LMXBs with well-studied retrograde precession periods are LMC X-4 (Lang et al. 1981; Paul & Kitamoto 2002) and SMC X-1 (Wojdowski et al. 1998).

cases, $\delta P/P \sim 10^{-4}$. This degree of stability is typical of signals emanating from a disc[2]. Taking the average value of P_{1011} (1011.43 (9) s) with a P_{orb} of 1028.7325 (4) s (Harvey et al. 1998), we obtain an undetected retrograde precession period of 0.69601 (6) d, with $\delta P_{prec}/P_{prec} \sim 10^{-4}$. This value is an order of magnitude higher in stabilities than that of the precession periods in Her X-1 and SS 433[3].

Could the 1011-s period instead originate from the spin of the primary? It is unlikely, given that spin periods tend to be more stable, by several orders of magnitude, than both the stabilities calculated in this paper and for typical precession periods in LMXBs (e.g. Bildsten et al. 1987). A spin-period model was considered for Her X-1, but lost to the tilted-disc model once the low stability of the 35-d signal was established (Ogelman et al. 1985, Ogelman 1987).

What about the magnetic field of either the primary or secondary star as the origin of P_{1011}? From K velocities, Pearson (2003) estimated that the secondary may possess a modest magnetic field of ~ 1 Tesla. The lack of X-ray detections or kilosecond QPOs in AM CVn, however, indicates that magnetic fields are not strong (Patterson et al. 2002). Furthermore, signals originating from magnetic activity tend to display higher stability than signals of disc origin.

We thus consider it reasonably well established that the 1011-s period in AM CVn is attributable to a beat between the orbit and retrograde precession period of a tilted accretion

---

[2] We note that negative superhumps tend to take longer to grow and decay than do the positive superhumps: months as opposed to weeks or days. Simulations have confirmed that tilt growth rate is roughly two orders of magnitude slower than the growth rate of disc eccentricity (Lubow 1992). Thus it seems reasonable to expect a small systematic difference in the stabilities of positive and negative orbital sidebands in CVs that display both signals. This statement is speculative, however, given the few long-term studies performed to date.

[3] The stabilities of the superorbital signals in these systems are: $\delta P/P \sim 10^{-3}$ for Her X-1 (Ogelman et al. 1985) and $\sim 2 \times 10^{-3}$ for SS 433 (Margon 1980).

disc. A reason for our lack of detection of a retrograde precession period may be its intrinsic faintness and our instrumental limitation of ~ 0.002 mag.

6.4.2 Lack of correlations between superhump period values

A spinning body will precess if the moments of inertia about the three axes are not equal and symmetric, or if an external torque is applied. If we approximate a tilted accretion disc as a rigid plane, then we can regard a CV as a three-body problem in which the disc is the perturbed object and the secondary is the perturber. In this scenario, the apsidal and nodal precession periods of the disc should be anti-phased. Such a phenomenon has been noted in the CV V603 Aql (Patterson et al.1997)

In AM CVn, we find no evidence that the period changes of the positive and negative superhump modulations are antiphased. Nor do we find evidence for a correlation between their respective amplitudes. This is not particularly surprising. The three-body problem described above is an oversimplified model for CVs. In a (fluid) accretion disc, properties at neighboring annuli – including temperature, viscosity, and rotational velocity – are not necessarily strongly coupled. Furthermore, the disc is not likely to be planar, but rather is warped to some degree (Petterson 1977a), probably due mainly to asymmetric radiation pressure from the central compact object (Petterson 1977b, Pringle 1996.) Positive and negative superhumps probably arise from different annuli: the former being linked to variation in the disc's outer radius, while the latter is probably attributable to energy dissipation at inner radii – since the matter stream flows over the edge and onto the inner disc if the disc is tilted (theory: e.g. Wood & Burke 2007; observation: e.g. Cherepashchuk 2002).

We do note a recent study that shows a positive correlation – and possible causal relation – between the appearances of positive and negative superhumps in the CV V344 Lyr (Wood et al. 2011). V344 Lyr alternates between high and low states and displays dwarf nova superoutbursts on the order of weeks. Wood et al. show that the onset of positive superhumps in V344 Lyr coincides with a shortening of the negative superhump period. They surmise that the underlying mechanism is change in disc radius: a disc weighted to smaller radii will precess slower, so in a system with a tilted disc, mass from the stream accumulates at small radius and so the retrograde precession period increases. A dwarf nova outburst, while triggering positive superhumps, pushes mass to larger radius – and thus the retrograde precession period – and hence the negative superhump period – shorten as the positive superhump appears.

These results are not terribly illuminating for the case of AM CVn, because AM CVn has demonstrated long-term stable brightness. Hence the cycle of changing disc radius is evidently not operating. There may well be a link between the respective cyclic behaviors of the positive and negative superhumps in AM CVn, but it is likely that observable manifestations of such a connection are overwhelmed by more powerful modulations in the light curve.

6.5 Summary

The 1011-second signal in AM CVn is most likely a negative superhump of disc origin, where the period corresponds to a beat between the orbit and unobserved retrograde disc precession. This conclusion derives from a 13-year baseline of photometry during which the signal demonstrated no period evolution and a stability comparable to that of the 1051-s signal. The inferred stability of the unobserved retrograde precession period is $\delta P_{pr-}/P_{pr-} = 10^{-4}$, which is comparable to the values obtained for two well-studied LMXBs, and is several orders of magnitude higher than values for signals associated with spin or magnetic fields of the stellar components.

We find no evidence that the periods of the 1011-s and 1051-s signals are correlated, an observation in keeping with warped disc models in which behaviors at different annuli are not strongly coupled. As will be examined in Chapter 7, the tilted-disc model for CVs is poorly constrained by observations. For this reason, it is important to conduct long-term monitoring of systems with negative superhumps, to search for retrograde precession signals and to place limits on non-detections of these signals.

6.6 Acknowledgements

Chapter 6, in part, is being prepared for submission for publication, with the following authors: Armstrong, E., Patterson, J. This dissertation author was the primary investigator and author of the material.

REFERENCES

[1] Poe, E. A., 1844, *The Balloon Hoax.* New York: The Sun

For other references, see References of Chapter 5.

7 Superorbital periods in CVs: *evidence for tilted discs*

"The ringing became more distinct ... it continued and gained definitiveness ... It was a *low, dull ... sound – much such as a watch makes when enveloped in cotton*."
Poe; *The Tell-tale Heart* (1843)

7.1 Summary of project

We examined two Hydrogen CVs that have displayed simultaneous superorbital and negative superhump periods such that Eq. 1.2 is satisfied and the superorbital period corresponds to "P_{prec}": the period of retrograde precession of the line of nodes of an accretion disc that is tilted with respect to the orbital plane. Prior to this study, just a few such CVs had been found. The "just a few" description is an accurate characterization of our knowledge at the start of this study, as no list of firm detections had been compiled. The tilted-disc model explains a long history of reliable detections in a few LMXBs, but is a problematic picture for CVs.

We report photometric detections of orbital, superorbital, and negative superhump periods in the H CVs: AQ Mensae (AQ Men) and IM Eridani (IM Eri). Combining these detections with a literature review, we tabulate the CVs that are known to display superorbital signals associated with retrograde disc precession: there are 12. We also find that AQ Men probably exhibits grazing eclipses, which would provide a lab for a detailed examination of tilted-disc geometry.

7.2 Introduction

Superorbital periods associated with accretion disc precession have been reported in well-studied low-mass X-ray binaries (LMXBs) since the first identification of this phenomenon in Hercules X-1 (Katz 1973; Roberts 1974; Petterson 1977). These periods are attributed to the motion of the accretion disc, in which different annuli coordinate their rotation rates to effect one of two types of precession: 1) prograde precession of the line of apsides of an eccentric disc, and 2) retrograde precession of the line of nodes of a disc that has tilted out of the orbital plane. It is the latter of these two types that is discussed in this paper.

Superorbital periods associated with retrograde disc precession are also observed in cataclysmic variables (CVs), although not as commonly: prior to the publication of this paper, only about ten CVs had been known to display them. This small sample size is due at least in part to the relatively few searches that have been conducted for these signals in CVs. Firm detections of such long-period signals require baselines of at least several weeks, for sufficient frequency resolution and for discrimination among the daily aliases that afflict ground-based photometry.

We report detections, in the nova-like CVs AQ Mensae (AQ Men) and IM Eridani (IM Eri), of orbital, superorbital, and negative orbital sideband periods (hereafter "negative superhump periods") obtained via long-term time series photometry. We also report a spectroscopic orbital period for IM Eri. Given the presence of the two faster signals, it is likely that the superorbital signals are due to retrograde disc precession. We also establish AQ Men as an eclipsing CV, an identification that has been difficult to make, due to the high variability of the orbital waveform in the light curve. We shall argue that the variability is likely to arise from *grazing* eclipses of the disc (the disc being the dominant light source), which changes shape with respect to the observer as it precesses. AQ Men thus presents a potential laboratory for probing the model of tilted discs in CVs. That is: it may offer an opportunity to study the disc shape in detail, and as a function of the strengths and phases of other periodicities that are present in the light curve.

A short biography of each object appears in its respective section in this chapter.

7.3 General observations & analysis

All data reported here were obtained by the globally distributed small telescopes of the CBA. We obtained differential photometry of the CV with respect to a comparison star on the same field, and spliced overlapping data from different longitudes by adding small constants to establish a consistent instrumental scale. With an excellent span of longitudes, we essentially eliminated the problem presented by daily aliasing of frequencies in the power spectra. To reach good signal-to-noise with good time resolution, the CBA generally observed in unfiltered light. This practice does, however, eliminate the possibility of transforming to a standard magnitude. The CCD detectors have good response over 4000-9000 Å, which yields $\lambda_{\rm eff} \sim$ 5600 Å for stars with colors typical of cataclysmic variables (B - V ~ 0). Thus the magnitudes correspond roughly to V light, although this cannot be made precise since the comparison star has a different $\lambda_{\rm eff}$ (which varies with color and airmass).

Differential magnitudes were obtained by computing the light within circular apertures of ~ 5 – 10 arcsecond radius. Typical exposure times were 1 minute, with 5 seconds of deadtime between images. After establishing a common magnitude scale, we inspected the spliced light curves for their general appearance. In this case, both stars' light curves looked typical of many nova-like variables. We searched the light curves for periodic signals by calculating Lomb-Scargle power spectra. Where warranted, we performed modeling and subtractions of periodic signals in the light curves via least-squares fitting of three-parameter waves (of frequency, amplitude, and phase). This method works well when the signal in question is approximately sinusoidal.

7.4 AQ Mensae

AQ Men, previously EC0511-7955, was identified as a CV by Chen et al. (2001). Their spectroscopy showed broad double-peaked Balmer emission lines, with profile variations consistent with Doppler broadening in a disc. Radial velocities suggested an orbital period of 3.1 h (7.7 c d^{-1}). The photometry on 9 nights showed no outbursts and no orbital modulation, and mild variability with an average magnitude of B = 15.1, except for one night when they saw a 0.85-mag dip resembling an eclipse (although they did not suggest that eclipses were actually occurring). They tentatively classified the object as a dwarf nova, based on the large-amplitude flickering at low frequency, and a spectrum that they described as one of fairly low excitation with features similar to those of known dwarf novae. But no outbursts or fadings were observed, and the spectrum – with both He II and a CIII/NIII blend in emission - is arguably more reminiscent of a nova-like variable. Thus those authors left open the question of proper classification. We favor the nova-like description, since there is still no record of eruptions.

One other targeted observation has been made of AQ Men, obtained by the Far Ultraviolet Spectroscopic Explorer (Godon et al. 2009), the results of which were consistent with – but less constraining than – those of Chen et al. (2001). They also cited unpublished results of our photometry, which we now present properly.

7.4.1 Photometry

We observed AQ Men for 177 hours on 33 nights over 49 days in 2002; Table 7.1 contains the summary observing log. The top panel of Fig. 7.1 shows the full light curve; at bottom is a representative ~ 0.8-day window showing the variable modulation. The out-of-eclipse brightness remained relatively stable throughout observations, with a mean magnitude of V = 14.6 (2) mag, with a systematic (calibration) error of ~ 0.3 mag. The star showed rapid flickering and possibly one large dip near the end of the light curve in the lower frame.

Table 7.1: Observing log of photometry

Object	*Dates (UT)*	*Dates (JD: 2,450,000+)*	*Hours*
AQ Men	2002 Feb 3 – Mar 24	2309-58	176.8
IM Eri	2002 Sep 20 - 1	2538-9	3.1
	2002 Nov 23 - 7	2602-6	38.4
	2002 Dec 14 - 22	2623-31	49.0
	2011 Dec 28 - 2012 Jan 29	5924-56	144.48

Note: Observing windows averaged 3-5 hours per night.

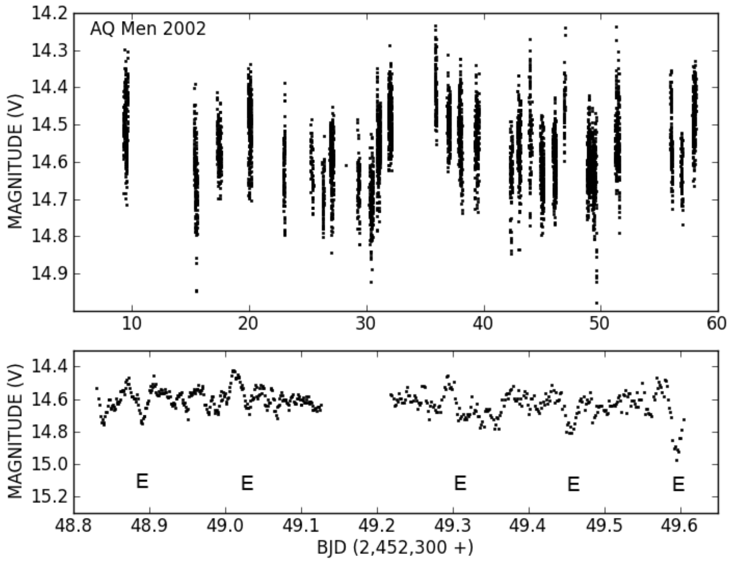

Fig. 7.1: *Top panel:* Full light curve of AQ Men in 2002. *Bottom:* A 0.8-day subset of the light curve, illustrating the variable modulation. E's designate times of eclipses. The V magnitudes have a systematic calibration error of ~ 0.3 mag.

The power spectrum of AQ Men over the 49 nights is shown in the top panel of Fig. 7.2, with features of interest noted. The strongest signal occurs at 0.263 (3) c d^{-1} (inset at right). The other prominent features are five sharp peaks at frequencies that are exact multiples of 7.0686 (3) c d^{-1}, where the error was derived from the dispersion of the five frequency values. These features indicate a strong periodic signal at that fundamental frequency, but apparently with a non-sinusoidal waveform (hence the many harmonics). A fold of the light curve on a period corresponding to this frequency value (7.0686 c d^{-1}) yielded the mean light curve shown in the lower frame. There is also a feature at 7.332 (3) c d^{-1} (inset at left), which will be discussed in §7.4.3. Table 7.2 lists frequencies and amplitudes of the three main features of interest.

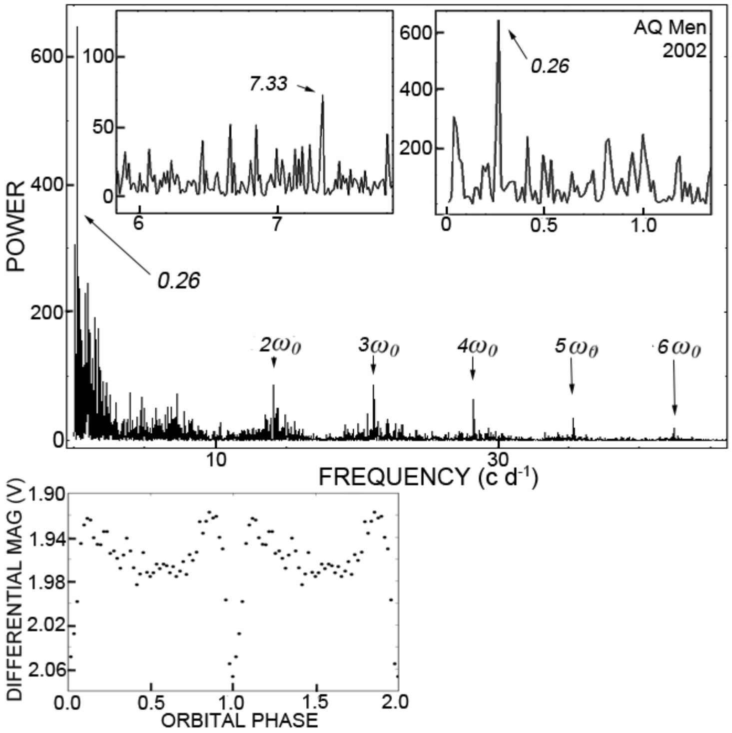

Fig. 7.2: Power spectra of AQ Men in 2002. *Top*: Power spectrum of full light curve, showing the first five harmonics of a fundamental frequency of 7.0686 (3) c d^{-1}; *inset, left*: magnification of the power spectrum showing a weak signal at 7.332 (3) c d^{-1}; *inset, right*: magnification of the full power spectrum showing a strong superorbital signal at 0.263 (3) c d^{-1}. *Bottom*: mean orbital light curve.

Table 7.2: Periodic photometric signals and amplitudes of the three main features of interest, in AQ Men and IM Eri

	orbital signal		superorbital signal		negative superhump	
CV	ω_o *(c* d^{-1}*)*	*Ampl (mag)**	ω *(c* d^{-1}*)*	*Ampl (mag)**	ω*- (c* d^{-1}*)*	*Ampl (mag)**
AQ Men	7.0686 (3)	0.07	0.263 (3)	0.08	7.332 (3)	0.04
IM Eri	6.870 (1)	0.02	0.354 (7)	0.08	7.226 (1)	0.08

*Magnitude uncertainties are ~ 0.01 and 0.002 mag for AQ Men and IM Eri, respectively.

7.4.2 The orbit

The mean orbital light curve (bottom panel of Fig. 7.2) shows a smooth modulation at a frequency of 7.0686 (3) c d^{-1}, with a sharp dip of ~ 0.13 mag lasting ~18 ± 2% of the cycle. The shape and duration of this dip resembles those of most eclipsing nova-like CVs. Thus we suspect that it is an ordinary eclipse of geometric origin, likely arising from the usual cause: the transit of the secondary across the disc face. In this case, however, there are two significant differences. It must be a somewhat *grazing* eclipse, in order to account for the low amplitude. It is also somewhat surprising that this systematic feature in the light curve has never been clearly evident in the nightly coverage. Does it in fact recur every time around?

Yes, probably it does. From the measured precise period and the start time of the time series, we derived an eclipse ephemeris:

Minimum light = BJD 2,452,309.2781 (3) + 0.141471(8) E.

We then examined each section of light curve for the times of scheduled eclipse. Every one shows a dip, though most are heavily masked by the strong flickering. A reason for why these eclipses have been missed during past observations could be as follows: if the disc is tilted and precessing with respect to the orbital cycle, then it will present a slightly different shape to the observer each time the secondary transits. If this reasoning is correct, then a more detailed study of the varying eclipse profile in AQ Men might provide a tool with which to probe theoretical predictions of tilted disc geometry.

Are our results compatible with the results of Chen et al. (2001)? Yes, they are. First, the spectra in that paper showed broad, double-peaked lines, the usual signature of high binary inclination (and especially of eclipsing CVs). Second, their radial-velocity period, though of low accuracy (0.130 (14) d), is consistent with our eclipse period. Third, their report of one isolated dip, which was not apparent on other nights, is compatible with our results. The "E" symbols in Fig. 7.1 show the times of expected eclipse. A dip occurs at each scheduled time, though only one is sufficiently deep to be visually prominent. We thus consider it demonstrated that AQ Men displays eclipses, despite the fact that it required 33 nights of data to identify them.

7.4.3 The negative superhump and superorbital period

We have established the prominence of two basic signals: an orbital frequency (ω_o) and a low frequency, which we designate as N. Only two types of several-day superorbital period have been detected in CVs, and they both typically have frequencies near 0.25 c d^{-1}: the "short outbursts" of ER UMa-type dwarf novae (Robertson et al. 1995), and signals commonly attributed to disc precession (e.g. Patterson et al. 1997). Since no outbursts are seen, there is no evidence that AQ Men is a dwarf nova. We thus reject the former interpretation. As for the latter possibility, roughly ten CVs with negative superhumps are known to display such signals (§7.8). Specifically, the signals present in these systems satisfy the following relation:

$$\omega_o + N = \omega_- \qquad 7.1$$

where ω_- corresponds to the frequency of the negative superhump. For AQ Men, this feature would occur at at $\omega = 7.0686\ (3) + 0.263\ (3) = 7.332\ (3)$ c d^{-1}.

As mentioned above, a feature is apparent weakly in the raw power spectrum at 7.332 (3) c d^{-1} (upper panel of Fig. 7.2, inset at left). Note that the peaks of comparable – but slightly lower – strength are *not* aliases, which we determined by taking the spectral window (Fig. 7.3) of a signal with a frequency of 7.332 c d^{-1} and amplitude of 0.04 mag (derived from a fold of the light curve on a period of $\frac{1}{7.332}$ days). Thus the 7.332 c d^{-1} is indeed as weak as it appears.

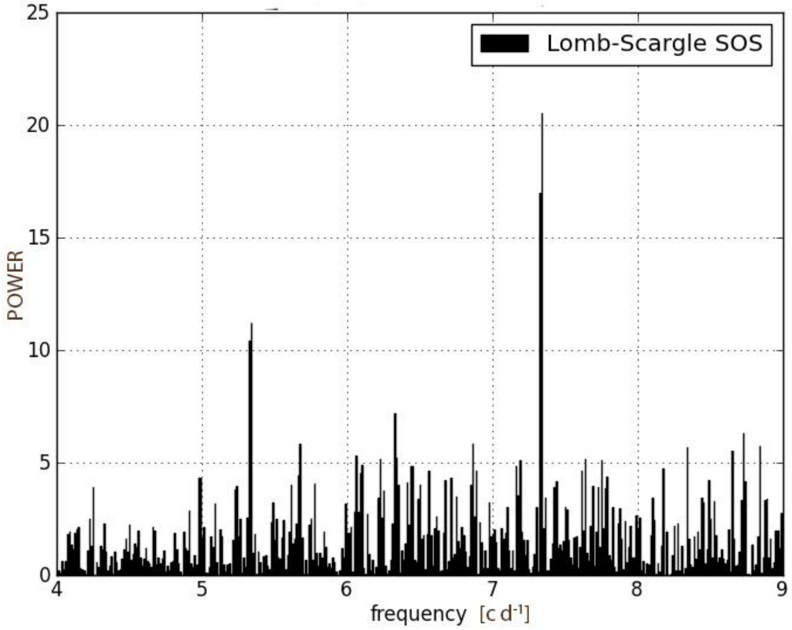

Fig. 7.3: Spectral window of the 7.332 c d^{-1} feature in AQ Men. The peaks of comparable (but lower) power in the upper left panel of Fig. 7.2 are not reproduced.

The feature appears only slightly stronger in the prewhitened power spectrum after removing the sections of light curve with orbital phase in the range 0.9 - 1.11 (the phase range corresponding to the width of the eclipse). Yet a signal at this frequency is expected in light of Eq. 7.1, and the feature persists throughout the observations baseline at roughly the same strength (this was confirmed by examining power spectra of shorter subsets of the light curve). We thus interpret it as a negative superhump.

Waveforms of the superhump and superorbital signals are shown in Fig. 7.4, in the left and right panels, respectively; both are approximate sinusoids. The ephemerides for these signals are:

- Negative superhump: Maximum light = BJD 2,452,309.309 (5) + 0.13646 (7) E
- Superorbital signal: Maximum light = BJD 2,452,309.26 (12) + 3.78 (5) E.

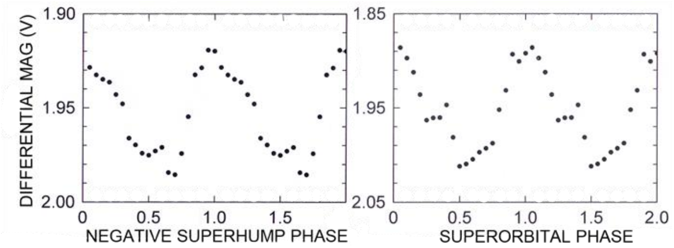

Fig. 7.4: Waveforms present in the light curve of AQ Men: *Left*: negative superhump; *right*: superorbital waveform.

7.5 IM Eridani

IM Eri is a ~ 12th-magnitude object that was identified as a nova-like CV by Chen et al. (2001), who named it EC04224-2014. It has displayed a relatively constant magnitude since its discovery. Spectroscopy by Chen et al. showed shallow H absorptions and an ultraviolet excess – the defining criterion of the Edinburgh-Cape Survey. They found rapid flickering in the photometry and no convincing photometric modulations; however, radial velocity measurements revealed a possible P_{orb} near 4.2 hours. On one night, the star was ~1.2 mag fainter and showed H lines predominantly in emission. These general characteristics suggest a “nova-like” interpretation, although the one-night excursion to a fainter state leaves open the dwarf-nova possibility.

7.5.1 Spectroscopy

Spectroscopic observations of IM Eri were conducted by a collaborator of this author, and yielded an orbital period measurement of 0.1456348(4) d. As this author did not conduct these observations nor write the results for publication, they have been omitted from this dissertation. For the full description of these observations, see the published version of this chapter (Armstrong et al. 2013).

7.5.2 Photometry

We obtained 90.5 hours of photometry on IM Eri during 21 nights that spanned 93 days in 2002, and 144.5 hours during 26 nights that spanned 32 days in 2012. Table 7.1 contains the observing log. Most of the data were obtained in V Light. The mean magnitude was V = 11.4 (2) in 2002 and V = 11.7 (2) in 2012. The visual appearance of the light curves was similar during the two years, and during each night. Because the 2012 coverage was more extensive and better distributed in time, most of our analysis focused on those observations. The top and bottom panels of Fig. 7.5 show the light curves obtained in 2002 and 2012, respectively.

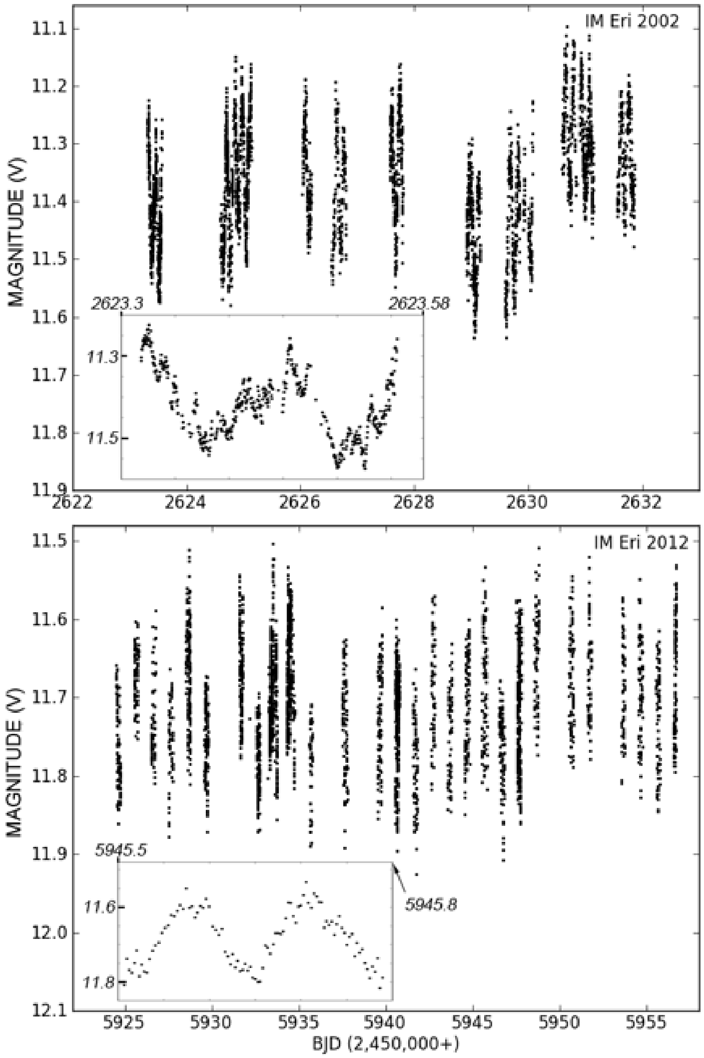

Fig. 7.5: *Top*: Light curve of IM Eri in 2002; *inset:* magnification of a 6.7-hour observations window. *Bottom:* Light curve of IM Eri in 2012; *inset:* magnification of a 7.2-hour observations window. The V magnitudes have a systematic calibration error of ~ 0.3 mag.

7.5.2.1 2012 result

The bottom frame of Fig. 7.5 shows the full 32-day light curve of 2012; inset is a representative ~ 7-hour window. We used the full 32-day light curve to determine period values. The top panel of Fig. 7.6 shows the power spectrum in the frequency range of 5 – 10 c d^{-1}. The power spectrum is dominated by a signal at 7.226 (1) c d^{-1}, which persists at roughly constant amplitude (0.08 (1) mag) over the baseline of observations. The bottom panel of Fig.

7.6 shows the power spectrum of the full light curve in the frequency range: 0 – 2.2 c d^{-1}, in which a feature is present at 0.354 (7) c d^{-1} with an amplitude of 0.08 (1) mag.

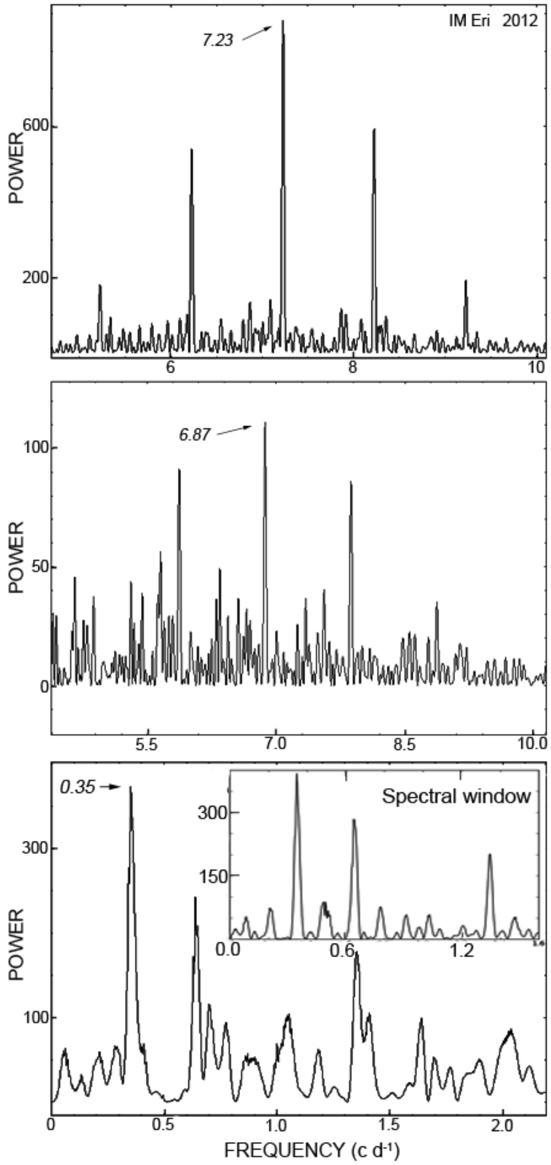

Fig. 7.6: Power spectrum of IM Eri in 2012. *Top*: the frequency range showing the prominent superhump signal at 7.226 (1) c d^{-1}. *Middle*: the same frequency range after the subtraction of the superhump, showing the orbital signal at 6.870 (1) c d^{-1}. *Bottom*: the frequency range of the original power spectrum showing the superorbital signal at 0.354 (7) c d^{-1}.

Both signals are flanked by aliases. The faster signal has merely the familiar ± 1 c d^{-1} structure. But with observations of ~1-day spacing, a low-frequency signal (at $\omega \cong 0.35$ c

d^{-1}) will be aliased with signals at (1- ω) and (1+ ω) c d^{-1}, and possibly also at 1 c d^{-1} if differential extinction is significant. This is important to recognize here, because what appears as “noise” in the low-frequency power spectrum is actually dominated by aliases of the low-frequency signal. The spectral window of the signal at 0.35 c d^{-1} is inset for comparison in the bottom panel of Fig. 7.6.

To search for an orbital signal, we subtracted the superhump from the full light curve and obtained the prewhitened power spectrum, which is shown in the middle panel. A signal is present at 6.870 (1) c d^{-1}, which is consistent with the radial-velocity period. We interpret it as the orbital signal. The best-fit sinusoid has an amplitude of 0.02 mag.

Thus we have a familiar triad of frequencies that satisfies Eq. 7.1: the orbital frequency at 6.86649 (2) c d^{-1}, (the precise radial-velocity period), a negative superhump at 7.226 (1) c d^{-1}, and a superorbital signal at 0.354 (7) c d^{-1}. Fig. 7.7 shows the mean waveforms of these signals. The extrema satisfy the ephemerides:

- Orbit: Minimum light = BJD 2,455,924.522 (2) + 0.1456346 (2) E
- Negative superhump: Maximum light = BJD 2,455,924.532 (2) + 0.13841 (3) E
- Superorbital signal: Maximum light = BJD 2,455,925.85 (7) + 2.809 (15) E.

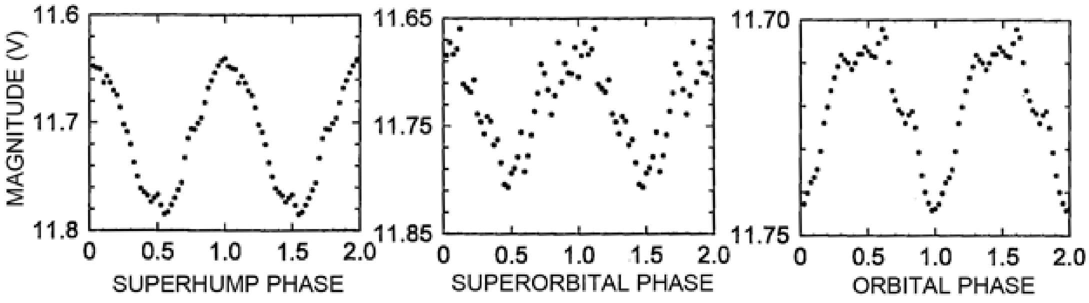

Fig. 7.7: Waveforms present in the light curve of IM Eri in 2012. *Left*: superhump; *middle*: superorbital waveform; *right*: orbital waveform.

7.5.2.2 2002 result

The baseline of observations in 2002 spanned 93 days, but the time coverage was not optimal (truncated JD = 538-9, 602-6, 623-31). The top panel of Fig. 7.5 shows the full light curve and a representative ~ 7-hour window (inset). Only the last nine days were sufficiently calibrated (between telescopes) to search for the superorbital signal. Consequently, the results of this season were more poorly constrained than those of 2012. The power spectrum created from a light curve of the final nine days yielded significant detections at 0.34 (3) and 7.22 (1) c d^{-1}, with amplitudes of 0.05 (2) and 0.09 (2) mag, respectively. To search for an orbital period at the spectroscopic value of 6.87 c d^{-1}, we removed the strong 7.22 c d^{-1} feature from the light curve. The prewhitened power spectrum showed a weak feature at 6.862 (10) c d^{-1}, but its power was only ~ 10% above noise level: too weak to count as a detection of the orbital signal. In summary, all the detections made from these data are consistent with – and less constraining than – the results of the more extensive 2012 analysis.

7.6 Significance tests of the superorbital periods

Sometimes, two periodicities that are present in a light curve can interact so as to produce an artifact in the power spectrum. The artifact can appear significant even though it does not represent a physically meaningful feature of the system. This phenomenon is not usually a problem for orbital and orbital sideband signals, because their periods are short compared to the durations of our photometry campaigns; hence their persistence throughout the baseline can be examined. For the superorbital signals, we performed two tests upon the superorbital periods in AQ Men and IM Eri, to establish their independence from the orbital and superhump signals.

First, for each star we created a light curve comprised of two sinusoids, one representing the orbit and the other the superhump, to determine whether the interaction of these signals alone could reproduce power at the superorbital frequency. We created the model waves using the parameters listed in Table 7.2, sampled them using the observing windows and sampling rates of the real data, and added Gaussian noise to simulate the S/N level in the power spectrum of the real data. As a second test, we subtracted the orbital and superhump signals from the light curve and examined the resulting power spectrum for any feature remaining at the superorbital frequency.

The results of these tests for the 2012 IM Eri data are shown in Figures 7.8 and 7.9, respectively. Fig. 7.8 shows the power spectrum of the real data (top) and the power spectrum of the two sinusoids (bottom): power at the superorbital frequency of 0.354 c d^{-1} is not reproduced by the model.

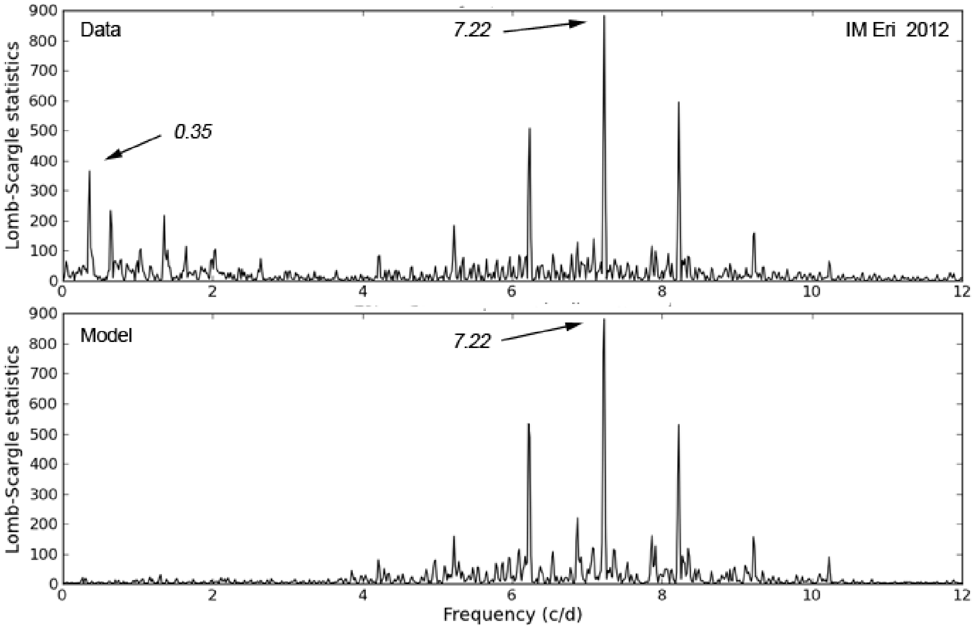

Fig. 7.8: *Top:* power spectrum of IM Eri in 2012, showing the superhump at 7.226 (1) c d^{-1} and superorbital signal at 0.354 (7) c d^{-1}. *Bottom:* power spectrum created from two model sinusoids representing the orbital and superhump signals. No power is present at the superorbital frequency.

Fig. 7.9 shows the result of the second test, comparing the power spectrum of the full light curve (top) to the prewhitened power spectrum (bottom). The superorbital feature remains after the removal of the faster signals.

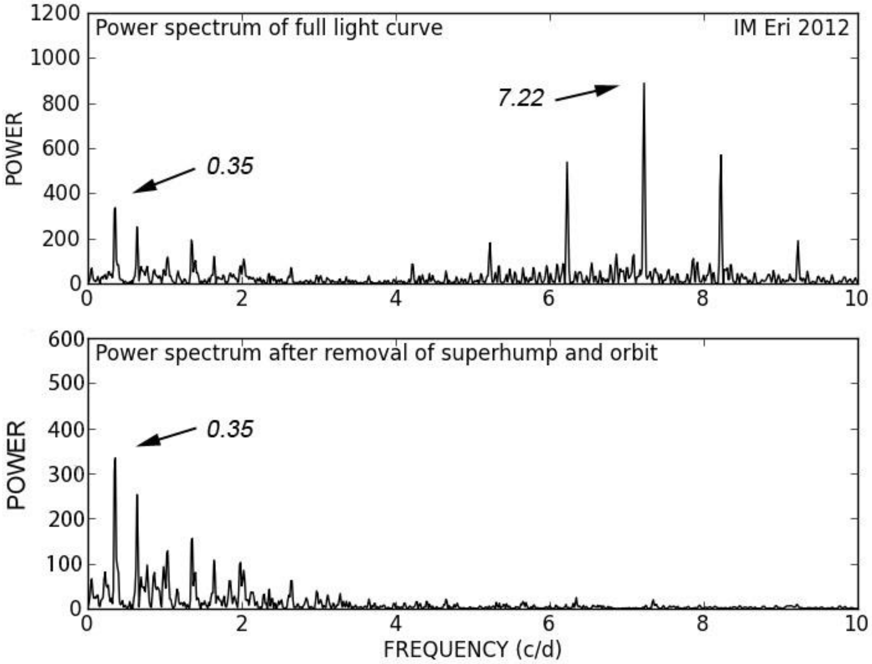

Fig. 7.9: *Top panel*: power spectrum of IM Eri in 2012, showing the superhump and superorbital signals. *Bottom*: prewhitened power spectrum after the removal of the superhump and orbital signals. The statistical significance of the feature at the superorbital frequency slightly increases after the subtraction.

For AQ Men, the test results are shown in Figures 7.10 and 7.11, respectively. Fig. 7.10 shows a comparison between the power spectra of the real 49-day light curve and the modeled data. The first and second panels show the comparison in the frequency range: 6 – 8 c d^{-1}; the third and fourth panels show the frequency range: 0 – 1.6 c d^{-1}. The model does not produce power at the superorbital frequency of 0.263 c d^{-1}.

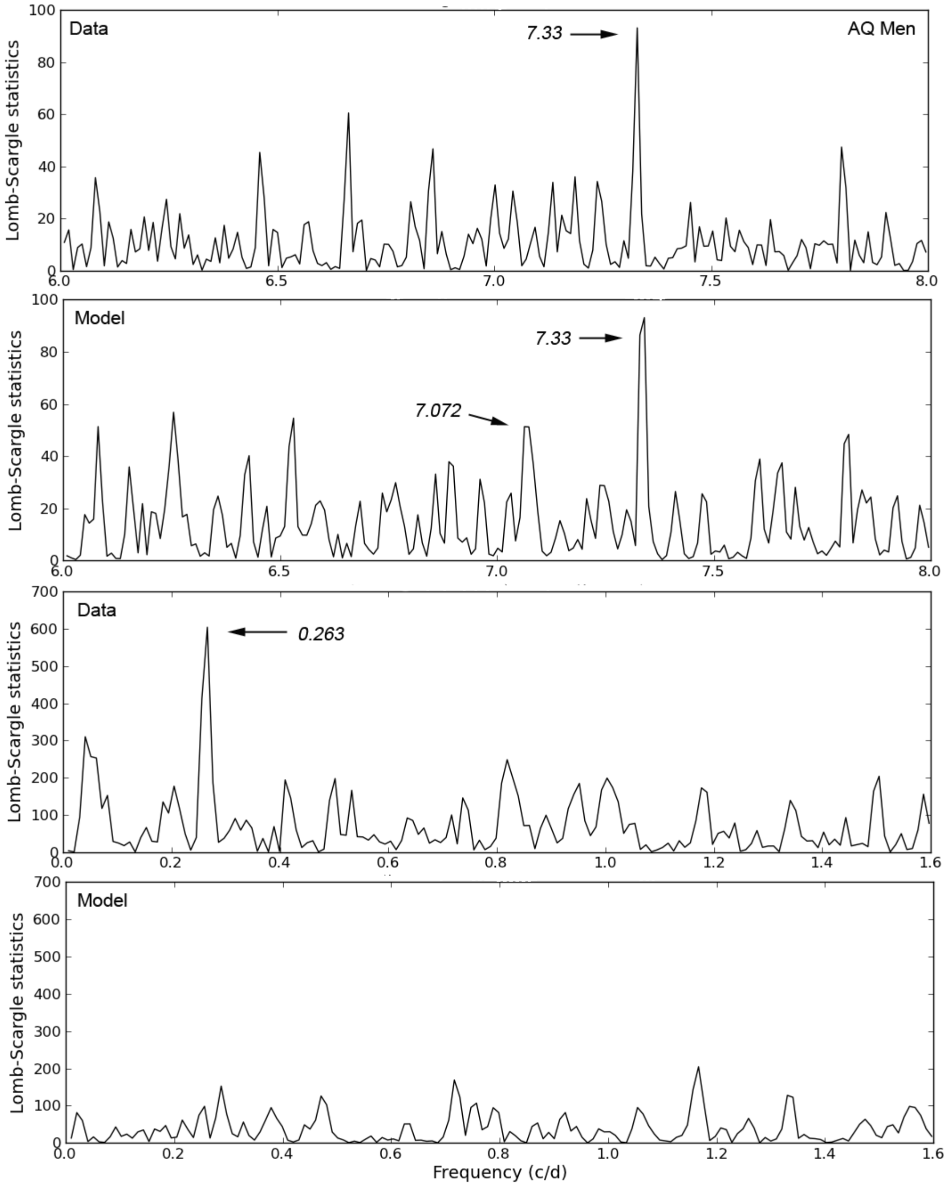

Fig. 7.10: *First panel:* power spectrum of AQ Men in the frequency range showing the superhump at 7.33 c d^{-1}. *Second:* power spectrum in the same frequency range, created from two model sinusoids representing the orbital and superhump signals (with $\omega = 7.072$ and 7.33 c d^{-1}, respectively). *Third:* Power spectrum of AQ Men in the frequency range showing the superorbital signal at 0.263 c d^{-1}. *Fourth*: power spectrum in the same frequency range, of the model light curve, showing no power at the superorbital frequency.

Fig. 7.11 shows the results of the second test for AQ Men, again within the same two sets of frequency ranges. The power at the superorbital frequency remains unaffected after the subtraction.

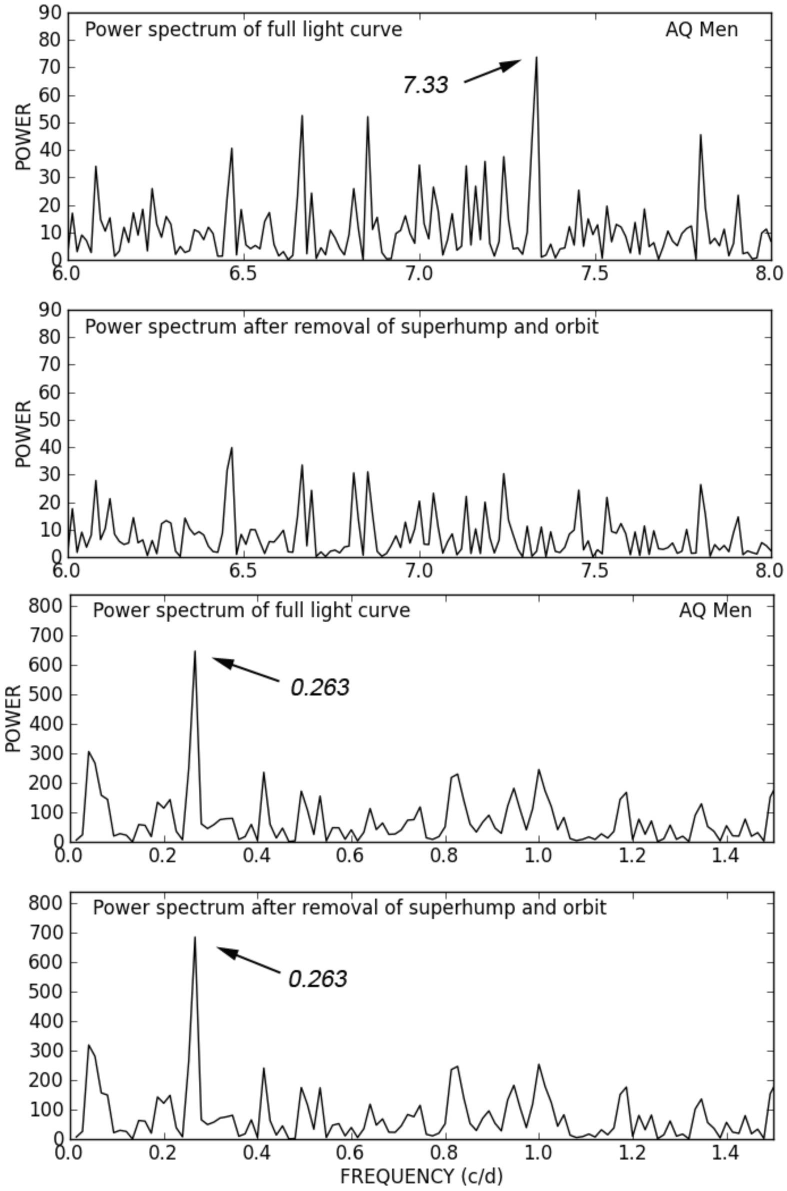

Fig. 7.11: *First panel*: power spectrum of AQ Men in the frequency range showing the superhump at 7.33 c d^{-1}. *Second*: prewhitened power spectrum in the same frequency range, after the removal of the superhump and orbital signals. *Third*: power spectrum in the frequency range showing the superorbital signal at 0.263 c d-1. *Fourth:* prewhitened power spectrum in the same frequency range after the removal of the superhump and orbital signals. The statistical significance of the feature at the superorbital frequency remains unaffected by the subtraction.

7.7 Simultaneous superorbital and negative superhump periods in CVs and LMXBs

7.7.1 Causes of disc tilt

The origin of disc tilt in XBs is likely to be irradiation by the primary compact object (Pringle 1996, Wijers & Pringle 1999, Maloney & Begelman 1997). Pringle (1996) showed that a sufficiently high central radiation pressure force will render an initially flat disc unstable to tilting, and that the primary neutron star in an XB meets this criterion.

In CVs, irradiation by the primary is insufficient to produce tilt (Petterson 1977, Iping & Petterson 1990). Possible mechanisms include:

- *Magnetic activity*. X-ray pulses in a few H CVs are taken as evidence for white dwarf magnetism, and may be the basis for QPOs (see Appendix A). Magnetism of the secondary is also plausible, since they are cool and rapidly-rotating. For a model of magnetically-warped and tilted discs in close binaries, see Murray et al. (2002).
- *Lift*. Simulations have shown that an initially un-tilted disc, after several hundreds of orbits, will begin to tilt via random asymmetries that are reinforced by lift alone – without the aid of irradiation or magnetic fields (theory: Montgomery & Martin 2010; simulation: Montgomery 2012).
- *Coronal wind.* Matter escaping from the system might create a repulsive force upon the disc (Schandl & Meyer 1994).

Another possible source of tilt, which has not been investigated for CVs, might be tidal torque due to the secondary star. For protostellar discs, it has been shown that an initial small tilt perturbation will grow via inclination Lindblad resonances due to the tidal torque of a secondary if the outer disc radius (R_{outer}) is below a critical fraction of orbital separation (Lubow & Ogilvie 2000). The requirement of small R_{outer} can be understood in the context of

Lubow (1992), in which it is demonstrated that horizontal tidal motions are important in stabilizing the disc against tilt. That is: if the horizontal torque of M_2 is sufficiently strong, M_2 will tend to keep the disc in line with the orbital plane – and this stabilizing effect strengthens as the disc fills more of the space between the stellar components.

Can this work on protostellar discs be extended to accretion discs in interacting binaries? The question is unsettled. Lubow & Ogilvie (2000) noted that their work may not apply to LMXB discs; however, Larwood (1998) used a tidal model to fit the long periods in Her X-1, SS 433, SMC X-1, and LMC X-4. This model has not been applied to CVs.

7.7.2 Stability of a tilted disc

Regardless of the cause of tilt, if a minor tilt perturbation on a CV disc can be incited, two reinforcing effects can follow. First, the two hemispheres of the secondary may experience variable asymmetric irradiation by the primary, due to the disc's shadow – which may vary the flux of the mass transfer stream (Smak 2009a and 2009b). Secondly, the stream will have a nonzero vertical velocity component with respect to the tilted disc, and thus will not strike the disc edge-on. Rather, infalling matter will encounter the disc face, imparting greater force upon one side over the other, thus possibly reinforcing tilt. The negative superhump modulation then results from energy dissipation at varying depth of the stream-disc impact point in the potential well of the primary (Smak 2009b).

Hydrodynamic simulations can reproduce negative superhump observations by attributing the observed modulation to the transit of the bright spot across the face of a tilted disc (Wood & Burke 2007; these authors also share elucidating animations: http://astro.fit.edu/wood/visualizations.html). The modulation at the retrograde precession period might be due to varying projected surface area of the disc (Patterson et al. 2002).

7.8 Our observations in context

Our observations of AQ Men and IM Eri bring the number of CVs known to display simultaneous negative superhumps and superorbital periods to 12 – a significant increase in sample size. In Table 7.3 we tabulate these 12 systems, eight of which are reliable detections and four of which are likely. All 12 objects show negative superhump and orbital periods, which, together with the value of the superorbital period, satisfy Eq. 7.1. For each system, there is a one-to-one correspondence between the appearances and disappearances of the negative superhump and superorbital periods. The "likely" four objects, listed with asterisks, have plausible evidence for superorbital signals, usually in the form of a folded light curve, but with no published power spectrum – which is needed to characterize the noise level at such low frequencies. For additional speculations regarding these objects, beyond the scope of §7.9 below, see Appendix J. (In addition to this small group, there are another ~ 15 CVs

Table 7.3: Superorbital Periods Observed in CVs, Derived from Photometry and Accompanied by Negative Superhumps

CV	P_{orb} *(d)*	P_{-} *(d)*	$P_{superorb}$ *(d)*
BK Lyn[1]	0.07494 (1)	0.07279 (1)	2.544 (12)
RX 1643+34[2]	0.12056 (2)	0.11696 (7)	4.05 (13)
V442 Oph	0.12435 (7) [3]	0.12090(8)[2]	4.37 (15) [2]
AH Men[4]	0.12721 (7)	0.1230 (1)	3.68 (3)
TT Ari	0.1375511(1)[5]	0.1328 (2)[6]	3.8 (2)[7]*
AQ Men[8]	0.141471 (6)	0.13639 (5)	3.80 (4)
V1193 Ori[9]	0.1430 (1)	0.1362 (1)	2.98 (8)*
V751Cyg[10]	0.1445 (2)	0.1394(1)	3.94(6)
IM Eri[8]	0.1456348 (4)	0.13839 (2)	2.82 (6)
PX And[11]	0.1463527 (1)	0.1415 (3)	4.8 (4)*
SDSS J0407-06[9—12]	0.17017 (1)	0.166 (1)	5.3 (7)*
TV Col	0.228599 (1)[13]	0.21667 (10)[14]	4.0 (8)[15]

* Period likely but not established beyond doubt.

References: (1) Patterson et al. 2012; (2) Patterson et al. 2002; (3) Hoard et al. 2000; (4) Patterson 1995; (5) Wu et al. 2002; (6) Kraicheva et al. 1999; (7) Udalski 1988; (8) This paper; (9) Ak et al. 2005a; (10) Patterson et al. 2001; (11) Stanishev et al. 2002; (12) Ak et al. 2005b; (13) Augusteijn et al. 1994; (14) Retter et al. 2003; (15) Motch 1981.

that show negative superhump periods, which have been tabulated in Table 2 of Montgomery (2009) – along with *calculated* retrograde precession periods. For almost all of these objects, however, no periodic-signal search at low frequency has been performed. That is: neither the presence of a precession period nor a lower limit on non-detections has been established).

Secondly, we have discovered AQ Men to be a member of this small group of objects – which also shows grazing eclipses. If our interpretation of the variable orbital waveform in AQ Men is correct, that is: if it is a manifestation of the disc's tilt, then detailed study of these shallow eclipses might offer an opportunity to explore the disc geometry. In particular: is the variable shape of the eclipse profile itself periodic? Such a study may be accomplished via more extensive photometry campaigns that can adequately define the shapes of individual eclipses (§7.9).

7.9 Questions

There exist (at least) three open questions that may be illuminated by further detailed photometric studies of superorbital periods in CVs, and by searches of CVs that are likely to display these periods (for example, those that have displayed persistent negative superhump periods).

Are retrograde precession periods more common in LMXBs?

The number of LMXBs that have displayed superorbital periods associated with retrograde disc precession may be as many as 25 (Kotze & Charles 2012) out of about 100 known (Ritter & Kolb 2012). (In addition to Her X-1, other well studied systems are SS 433 (Cherepashchuk 2002), LMC X-4 (Lang et al. 1981; Paul & Kitamoto 2002), and SMC X-1 (Wojdowski et al. 1998)). In contrast, the few hundred CVs that have been searched for superorbital periods have yielded only the twelve of Table 7.3. Why the disparity?

Have LMXB observers merely obtained a head start in terms of time? Perhaps. The 35-day signal in Her X-1 was convincingly identified as a retrograde precession period in a LMXB in the 1970's (Katz 1973, Petterson 1977). The first such observation in a CV, TV Columbae, occurred about ten years later (Bonnet-Bideaut et al. 1985).

Feasibility is likely to be a significant reason. To observe signals with periods of days, one requires dense observations over weeks. While some X-ray telescopes have surveyed the sky continually for years (e.g. the High Energy Astronomy Observatory (HEAO-1), Rossi X-ray Timing Explorer (RXTE)), obtaining sufficient time on ground-based telescopes usually requires the dedicated work of coordinated groups – and the weather's cooperation. Otherwise, the task is only realistic for private owners of telescopes. In fact, a privately-owned telescope at the University of Washington was one source of a detailed study of optical variability on a superorbital timescale in a LMXB (Deeter et al. 1976).

Underlying physics may also be accountable, in two respects. First, it is possible that disc tilt is intrinsically more common in LMXBs, given that a likely tilt mechanism in CVs has yet to be identified. Secondly, the relative strength of a superorbital modulation compared to overall system brightness may differ between LMXBs and CVs. Independent of the likelihood of disc tilt: *if* the disc *does* tilt, will the resulting superorbital modulation be significantly easier to observe in LMXBs? This does not seem likely. In LMXBs, the modulation at the superorbital period is attributed to periodic occultation of the primary by the disc (e.g. Katz 1973), which tends to be a strong feature of the system. In a CV, if the modulation at the superorbital period is due to variable disc surface area that is presented to the observer, this should also be a strong effect, as the disc emission dominates a CV light curve. These possibilities, however, are speculation; they are fascinating issues for future study.

For the record, we note that negative superhumps have been reported in significantly more CVs than LMXBs. The only convincing detections in LMXBs have been in the two best-studied cases: Her X-1 (Deeter et al. 1976; Jurua et al. 2011) and SS 433 (Kemp et al. 1980; Kemp et al. 1986; Katz 1981). This finding is not surprising, as negative superhumps in both types of system are observed at optical wavelengths – which is the default realm of operation for CV observers.

Long-term stability of a tilted disc?

Negative superhumps and superorbital periods associated with retrograde precession are not strictly persistent features of the systems in which they have been detected. Generally, these signals persist throughout an observing season of several months' duration, are not detected a year or so later during an observing season of comparable length, and reappear several years after that (Patterson et al. 1997)[1]. If taken within the context of tilted-disc geometry, then these observations indicate: 1) a disc can remain stably tilted over a timescale of months but probably not years; 2) after the disc has re-aligned with the orbital plane and maintained this alignment for a year or so, it returns to its previous tilted state. Why?

Could a sudden decrease in $\dot{M}$ be responsible? In tilted-disc geometry, the greater the mass transfer rate, the greater the asymmetry in the flux of the mass flow over and under the disc – and hence the greater power supplied to reinforce tilt. A decrease in the extremity of this asymmetry might result in a decrease in tilt angle. It would also lower the rate of gravitational potential energy dissipation, and hence the amplitude of any negative superhump modulation. Observations do not support this suggestion: there is no correlation between

---

[1] There also appears to be no correlation between the longevity of a particular negative superhump or superorbital period and its amplitude during the time it is detected (private communication: Patterson, J).

these signals’ appearances and changes in the overall magnitude of the system.

What about a sudden change in disc radius? As discussed in §7.7.1, Lubow & Ogilvie (2000) showed that for protostellar discs of sufficient size, the horizontal tidal torque of M_2 stabilizes the disc against tilt. In CVs, does the appearance of negative superhump signals correlate with variable disc size? The question has not been investigated. It is possible that a more detailed photometric study of the eclipses in AQ Men might probe this question.

What about varying disc thickness, and its tendency to stabilize a disc against tilt? Should we expect disc thickness to vary with the system’s temperature or disc size? This has not been examined.

Finally, it is possible that phenomena associated with *positive* superhumps play a role (e.g. Wood et al. 2011). More extensive monitoring of these CVs, with denser baselines of observations, may provide tighter constraints on the time frames in question, and possibly address this issue.

Varying tilt of the disc?

The eclipses of AQ Men vary greatly in depth. Even *consecutive* eclipses vary greatly, and this suggests that erratic flickering contributes significantly to the variability. But the shallowness of the average eclipse also requires that the eclipses be grazing, which could produce a large asymmetry in which the back of the disk (where “back” is in reference to the observer) is not eclipsed, while the front is. With a more extensive observational campaign, we might study whether the variable shape of the eclipse profile is itself periodic. Such a study appears to be eminently feasible for this star, and we hope to use it to constrain the disc geometry.

One possible application of studying the varying eclipse profile in AQ Men is a test of simulations done by Montgometry (2012). Specifically: does the orientation of a tilted disc with respect to the mass transfer stream influence the depth of the stream-disc impact point in the potential well of the primary? Montgomery (2012) showed that, for a disc tilted at 5˚ with respect to the orbital plane, the stream flows over the disc rim for ~ half an orbit and then under for ~half an orbit, and that as the disc precesses, the location on the disc rim where the stream transitions from over-the-disc to under-the-disc moves in the retrograde direction. This possibility might be investigated via a study of the superhump strength as a function of the phase of the superorbital signal – since the superhump modulation is thought to be due to varying depth of the stream-disc impact point in the potential well of the primary.

We note that a few detailed optical studies of variability linked to superorbital timescales have been done with LMXBs, and have illuminated questions regarding the systems' geometry. Deeter et al. (1976), for example, found optical modulations in Her X-1 repeating on the 35-day retrograde precession period, and attributed them to the uniformly-changing orientation of luminous parts of the system.

7.10 Summary and future work

AQ Men and IM Eri have displayed orbital, superorbital, and negative superhump signals, which can be understood within the context of a tilted accretion disc. This identification brings the number of CVs that display this phenomenon to 12. Furthermore, AQ Men has been found to display grazing eclipses, which may provide a unique opportunity to study the variable disc geometry in detail.

More long-term time series photometry of CVs that are likely to display superorbital signals may provide constraints on models of tilted accretion discs for this class of object. Worthy targets are CVs that have displayed negative superhumps (Table 2 of Montgomery (2009). A search of the Kepler field might also be a worthy time investment. It contains 21 CVs, none of which have published values of superorbital periods, but two with well-studied negative superhumps: V1504 Cyg (Wood et al. 2013; Osaki & Kato 2013) and V344 Lyr (Wood et al. 2011).

7.11 Acknowledgements

Chapter 7, in part, is a reproduction of material as it appears in Monthly Notices of the Royal Astronomical Society: Armstrong, E., Patterson, J., Michelsen, E., Uthas, H., Vanmunster, T., Hambsch, F.-J., Roberts, G., Dvorak, S. 2013, MNRAS, DOI: 10.1093/mnras/stt1335. This dissertation author was the primary investigator and author of the material.

REFERENCES

[1] Ak, T., Retter, A., Liu, A. 2005b, New Astr, 11, 147

[2] Ak, T., Retter, A., Liu, A., Esenoglu, H.H., 2005b, PASA, 22, 105

[3] Bonnet-Bideaut J., Motch, C., Mouchet, M. 1985, Astron. Astrophys., 143, 313

[4] Augusteijn, T., Heemskerk, M., Zwarthoed, G., van Paradijs, J. 1994, Astron. & Astrophys. Suppl. Ser. 107, 209

[5] Chen, A., O'Donoghue, D., Stobie, R.S., Kilkenny, D., Warner, B., 2001. MNRAS, 325, 89

[6] Cherepashchuk, A. 2002, Space Science Rev., 102, 23

[7] Deeter, J., Crosa, L., Gerend, D. 1976, ApJ, 206, 861

[8] Godon, P., Sion, E.M., Barrett, P.E., Szkody, P., 2009, ApJ, 701, 1091

[9] Hoard, D., Thorstensen, J., Szkody, P. 2000, ApJ, 537, 936

[10] Iping, R.C., Petterson, J.A., 1990, A&A, 239, 221

[11] Jurua, E., Charles, P.A., Still, M., Meintjes, P.J., 2011, MNRAS, 418, 437

[12] Katz, J., 1981, A&A Lett., 95, L15

[13] Katz, J.I. 1973, Nature Phys. Sci., 246, 87

[14] Kemp, J.C., Barbour, M.S., Arbabi, M., Leibowitz, E.M., Mazeh, T., 1980, ApJ Lett., 238, L133

[15] Kemp, J.C., Henson, G.D., Kraus, D.J., Carroll, L.C., Beardlsey, I.S., 1986, ApJ, 305, 805

[16] Knigge, C. 2006, MNRAS, 373, 484

[17] Kotze, M., Charles, P. 2012, MNRAS, 420, 1575

[18] Kraicheva, Z., Stanishev, V., Genkov, V., Iliev, L. 1999, A&A, 351, 607

[19] Lang, F.L., Levine, A.M., Bautz, M., Hauskins, S.H., Primini, F.A., Lewin, W.H.G., 1981, ApJ, 246, L21

[20] Larwood, J. 1998, MNRAS, 299, L32

[21] Lubow, S.H., Ogilvie, G.I., 2000, ApJ, 538, 326

[22] Lubow, S.H. 1992, ApJ, 398, 525

[23] Maloney, P., Begelman, M., 1997, ApJ, 491, L43

[24] Montgomery, M.M., 2012, ApJ, 745, 25

[25] Montgomery, M.M., 2009, MNRAS, 705, 603

[26] Montgomery, M., Martin, E. 2010, ApJ, 722, 989

[27] Motch, C. 1981, A&A, 100, 277

[28] Murray, J., Chakrabarty, D., Wynn, G., Kramer, L., 2002, MNRAS, 335, 247

[29] Osaki, Y., Kato, T. 2013, eprint arXiv:1212.1516

[30] Patterson, J., Uthas, H., Kemp, J., de Miguel, E., Krajci, T., Foote, J., Hambsch, F.-J., Campbell, T., Roberts, G., Cejudo, D., Dvorak, S., Vanmunster, T., Koff, R., Skillman, D., Harvey, D., Martin, B., Rock, J., Boyd, D., Oksanen, A., Morelle, E., Ulowetz, J., Kroes, A., Sabo, R., Jensen, L. 2012, eprint arXiv: 1212.5836

[31] Patterson, J., Fenton, W., Thorstensen, J., Harvey, D., Skillman, D., Fried, R., Monard, B., O’Donoghue, D., Beshore, E. et al., 2002, PASP, 114, 1364

[32] Patterson, J., Thorstensen, J.R., Fried, R., Skillman, D.R., Cook, L.M., Jensen, L., 2001, PASP, 113, 72

[33] Patterson, J., Kemp, J., Saad, J., Skillman, D. R., Harvey, D., Fried, R., Thorstensen, J. R., Ashley, R. 1997, PASP, 109, 468

[34] Patterson, J. 1995, PASP, 107, 657

[35] Petterson, J.A., 1977, Ap J, 218, 783

[36] Paul, B., Kitamoto, S., 2002, JApA, 23, 33

[37] Poe, E.A., 1843, *The Tell-tale Heart*. Philadelphia: The Pioneer, Vol. I, No. I, Drew and Scammell

[38] Pringle, J.E., 1996, MNRAS, 281, 357

[39] Retter, A., Hellier, C., Augusteijn, T., Naylor, T., Bedding, T.R., Bembrick, C., McCormick, J., Velthius, F. 2003, MNRAS, 340, 679

[40] Ritter H., Kolb U. 2003, A&A, 404, 301 (update RKcat7.18, 2012)

[41] Roberts, J.W. 1974, Ap J, 187, 575

[42] Robertson, J., Honeycutt, R., Turner, G. 1995, PASP, 107, 443

[43] Scargle, J., 1982, ApJ, 263, 835

[44] Schandl, S., Meyer, F., 1993, Astron. Astrophys., 289, 149

[45] Schneider, D., Young, P. 1980, ApJ, 238, 946

[46] Shafter, A.W., Szkody, P., 1984, ApJ, 276, 305

[47] Skillman, D.R., Patterson, J., 1993, ApJ, 417, 298S

[48] Smak, J., 2009a, AA, 59, 419

[49] Smak, J., 2009b, AA, 59, 121

[50] Smak, J., 2008, Acta Astron., 58, 55

[51] Stanishev, V., Kraicheva, Z., Boffin, H.M.J., Genkov, V. 2002, A&A, 394, 625

[52] Thorstensen, J. R., Patterson, J., Thomas, G., & Shambrook, A. 1996, PASP, 108, 73

[53] Udalski, A. 1988, Acta Astr., 38, 315

[54] Wijers, R., Pringle, J. 1999, MNRAS, 308, 207

[55] Wojdowski, P., Clark, G.W., Levine, A.M., 1998, ApJ, 502, 253

[56] Wood, M.A., Still, M.D., Howell, S.B., Cannizzo, J.K., Smale, A.P., Ramsay, G., Barclay, T. 2013, American Astron. Soc, AAS Meeting 221, 401.03

[57] Wood, M.A., Still, M., Howell, S., Cannizzo, J., Smale, A. 2011, ApJ, 741, 105

[58] Wood, M.A., Burke, C.J., 2007, ApJ, 661, 1042

[59] Wu, X., Li, Z., Ding, Y., Zhang, Z., Li, Z. 2002, ApJ, 569, 418

[60] Zamko, P., Kato, T., Shugarov, S. 2012, arXiv: 1212.5940

APPENDIX A: Other signals in CVs

Signals that are important to our understanding of CVs, which do not directly relate to the studies in this dissertation, include:

- *"Flickering"* (seconds to minutes): the most prominent feature of a CV light curve. Amplitudes are ~ 5 – 40% of the total brightness, among different CVs. They are low in coherence and believed to originate in the disc (Yonehara & Mineshige 1997).
- *White dwarf spin period* (seconds to minutes): highly coherent, often observed in magnetic systems, interpreted as the period of rotation of the primary (e.g. Walker 1956). The CVs discussed in this dissertation do not possess strong magnetic fields.
- *Dwarf nova oscillations*, or DNOs (seconds): signals of low coherence that appear to follow a period-luminosity relation in CVs that undergo large changes in magnitude (Warner & Woudt 2008; review: Warner 2004).
- *Quasi-periodic oscillations*, or QPOs (minutes): signals of low coherence, often appearing in the high states of some CVs (Warner & Woudt 2008). Origins of DNOs and QPOs might relate to the interaction between the WD's magnetic field and accreting matter (Warner & Woudt 2002).
- *Non-radial pulsations*, or NRPs (minutes): highly periodic, observed in isolated WDs with hydrogen-rich atmospheres (Gianninas et al. 2006) and occasionally in quiescent CVs (Warner & van Zyl 1998).
- *Recurrent novae* (10 – 100 years): explosions more violent than dwarf nova outbursts and superoutbursts, causing brightness changes of up to 19 mag; believed to involve the accretion of matter onto the WD surface.
- *Classical novae* (~ $10^{4\text{-}5}$ years): due to thermonuclear detonation on the WD surface.

Note: Citations are listed in the References section of Chapter 1.

APPENDIX B: Energy considerations

As noted in §1.2.6.1, we can reproduce the observed flux from a CV by invoking radiated gravitational potential energy during infall toward a white dwarf (Eq. 1.3) and approximating the white dwarf as a black body (Eq. 1.4). Combining Eq. 1.3 and 1.4, we obtain:

$$T^4 = \frac{GM_1\dot{M}}{\sigma 4\pi r^3} \qquad \text{B.1}$$

(Hellier 2001). Note that this derivation is an approximation. The total accretion luminosity is given by Eq. 1.3, but only half comes from the disc. The other half is released in a "boundary layer" that lies between the inner disc radius and the white dwarf surface. This energy release occurs because the Keplerian velocity of matter in the disc is ~ ten times faster than that of the white dwarf (~ 10^3 versus 10^2 km s^{-1}), and the excess kinetic energy must be dissipated.

To infer the mass transfer rate $\dot{M}$ from observed magnitudes, we can make approximations of the disc's temperature (T) and size (R_{outer} and R_{inner}) and the mass of the white dwarf (M_1), based on both theory and observation.

- $R_{outer} < \sim 10^8$ m (from the tidal limit from Roche geometry; consistent with eclipse mapping results);
- $R_{inner} \sim 10^7$ m (from models of the interaction of disc material with the WD).
- T at R_{outer}: ~ 100,000 K
- T at R_{inner} ~ 5,000 K
- $\langle M_1 \rangle \sim 0.75 M_\odot$ (Knigge 2006).

From observed magnitudes of hydrogen CVs, the above approximations yield mass accretion rates ($\dot{M}$) of 10^{-8-10} $M_{\odot}$ yr^{-1}, depending on P_{orb}. It is reasonable to expect that such rates can be sustained over the long term without resulting in detonations on the white dwarf surface (Iben et al. 1992).

Note: Citations are listed in the References section of Chapter 1.

APPENDIX C: Evidence for long-term continuous mass accretion in a CV

How do we know that long term (t > 10^8 years) mass accretion is occurring in a CV? We have only been observing these systems for ~ 10^2 years. Could it be that we are glimpsing them in a transient state of mass transfer, in which angular momentum is conserved and the mass transfer will end shortly after we die? I offer two arguments against this suggestion.

First, the observed relationship between a CV secondary's mass M_2 and orbital period (Fig. 1.8) indicate that evolution in M_2 is occurring on the timescale of evolution of P_{orb}., which corresponds to a rate of change in period of one part in 10^{-11-14}.

Secondly, we can estimate the timescale on which the secondary will detach from its Roche lobe under conservation of angular momentum. The density of matter in a stellar atmosphere can be characterized in terms of pressure, where one pressure scale height – between two radii – represents a significant difference in density. In a typical solar model, a Roche lobe radius increase by a factor of e in pressure scale height corresponds to a distance of ~ 1/10,000th of the secondary's radius – which should occur within a few decades.

APPENDIX D: The maximum and minimum orbital periods for hydrogen CVs

Two notable features of the period distribution for H CVs, which do not relate directly to studies in this dissertation, are: a period maximum of ~ 12 hours and a period minimum of ~ 80 minutes.

The period maximum is set by the maximum mass of the primary ($1.4M_\odot$) and the requirement that q not exceed 1.

The period minimum of ~ 80 minutes (Gänsicke et al. 2009) can be understood in terms of competing timescales. For a non-degenerate secondary, there exists a minimum mass below which the mass-transfer timescale is faster than the secondary's thermal timescale (or Kelvin-Helmholtz timescale) τ_{KH}. That is: matter is stripped from the secondary faster than the star has time to adjust its radius accordingly. As a result, the star will expand in response to mass loss. For systems evolving via GWR, the mass transfer timescale becomes on the order of τ_{KH} when the secondary mass is around $0.12M_{sun}$, or $P_{orb} \approx 80$ minutes (Paczynski 1981). Simulations have produced a shorter period minimum around 65 minutes (Kolb 1993). The inconsistency is not understood, but may be due to the low mass transfer rates– and hence intrinsic faintness – of CVs in the region below 80 minutes.

In addition to this effect, as the secondary evolves it will begin to expand upon mass loss due to the nature of degenerate matter. In *helium* CVs, the theoretical period minimum is essentially set entirely by the degeneracy of the secondary.

Note: Citations are listed in the References section of Chapter 1.

APPENDIX E: Related areas of study of hydrogen CVs

The following areas of study are important to our understanding of CVs but do not pertain directly to the topics discussed in this dissertation.

Age of CVs

CVs above the period gap are probably younger than ~ 1.5 x 10^8 years, while those below the period gap are ~ 2 to 3 times as old (3 – 4 x 10^8 years) (Kolb & Stehle 1996). These numbers have been derived from considerations of birthrates and timescales of evolution. (Note: these timescales begin at the onset of continuous stable mass transfer from the secondary to the white dwarf; they do not include the ~ 10^8 years for the primary to evolve from the main sequence).

Space density

Because of the difficulty in obtaining accurate distances to CVs and selection effects of surveys, it is difficult to make a reliable estimate of the galactic space density. Theoretical predictions are an order of magnitude higher than the observed value: ~ $\frac{1}{10^4}$ versus $\frac{1}{10^5}$ per cubic parsec, respectively. For a discussion of observational constraints, see Pretorius et al. (2007a). For a discussion of the difficulty in obtaining accurate observational constraints, see Pretorius et al. (2007b). For an outline of a model for the intrinsic population, see Kolb (1993).

In addition, from timescales of magnetic braking, GWR, and stellar evolution, 99% of hydrogen CVs should have evolved below the period gap, and 70% beyond the period minimum (Kolb 1993). Yet no systems below the period gap have been reliably identified. Kolb (1993) discusses weaknesses in the model used to obtain their estimates, including an assumption of constant CV formation rate over the history of the Galaxy and a poor understanding of the CE phase during the formation of the progenitor.

Note: Citations are listed in the References section of Chapter 1.

APPENDIX F: Three routes to helium CV Synthesis

Three likely routes to birth of a He CV have been identified, defined by the nature of the secondary star at the onset of continuous long-term mass transfer.

1. A helium or hybrid white dwarf

If the secondary is fully degenerate at the onset of Roche lobe overflow (RLOF), then limits on its size and density require that the composition be essentially all helium: a "helium white dwarf", or contain only a small percentage of heavy elements: a "hybrid" (Nelemans et al. 2001). A helium CV with a fully degenerate white dwarf secondary is sometimes called a "double white dwarf"

2. A helium star

A helium *star* is burning He at RLOF. This system initially evolves toward shorter period (due to GWR), and is predicted to reverse direction as degeneracy sets in. Observationally, a He star might be distinguishable from a He white dwarf by showing weak H lines from an outer H shell. Helium burning may continue after the onset of mass transfer and lead to composition changes. When the He is exhausted, the system becomes indistinguishable from the white dwarf channel (Nelemans et al. 2001).

3. An evolved hydrogen star

If a main sequence star fills its Roche lobe and begins mass transfer sufficiently late during its H-burning lifetime, the H-deficient core can be exposed such that the star evolves far below the usual period minimum for H CVs. That is: a hydrogen CV could evolve into a He CV in some cases. Chemical compositions indicate that such cases are rare (Nelemans et al. 2010). For estimates of expected number densities, see Podsiadlowski et al. (2003).

Note: Citations are listed in the References section of Chapter 5.

APPENDIX G: The two fastest helium CVs?

The two objects classified as He CVs with the shortest orbital periods, HM Cnc and V407 Vulpeculae, possess characteristics that are unusual if set within the context of accreting helium-rich binaries. The spectrum of HM Cnc shows faint Balmer transitions of hydrogen, where $0.05 < \mathrm{He/H} < 0.2$ by number (Reinsch et al. 2007): four orders of magnitude lower than typical values for He CVs. A proposed explanation is that HM Cnc still possesses a thick, non-degenerate hydrogen envelope (D'Antona et al. 2006). In addition the spectral lines are not double peaked. Double-peaked lines constitute the primary evidence for an underlying disc structure; however, not *all* CVs show such a signature. Double-peaked structure can be difficult to discern in lines that appear in absorption – as they do for the most rapidly-rotating (and hottest) He CVs.

The identification of V407 Vul is significantly more problematic, as its spectrum is featureless. The continuum is consistent with that of a G star, which may be attributable to a G star that lies along the line of sight (Barros et al. 2007). V407 Vul is classified as a He CV based on a persistent period that is characteristic (in terms of stability) as an orbital period, and its temperature. Yet in light of its lack of spectral features, which are a critical defining characteristic of a CV, this author does not understand why V407 has attained membership in this class of object.

Other models have been proposed to explain the observed periods in HM Cnc and V407 Vul, most commonly: a spin period of the primary white dwarf. This alternative, however, does not strongly predict a consistent negative value of $\dot{P}$ (Marsh & Nelemans 2005).

Note: Citations are listed in the References section of Chapter 1.

APPENDIX H: Population synthesis for helium CVs

The intrinsic population of He CVs is poorly constrained, due to theoretical uncertainties regarding the probability of survival of a binary through two CE phases without being destroyed by detonations from He accretion onto the primary. Other conditions leading to stable mass transfer, including the spin rate of each star, are highly uncertain.

Nelemans et al. (2001) predicted the intrinsic galactic population of He CVs to be 2,400 via the hydrogen star channel and 140,000 via the He white dwarf and He star channels. The observed populations are two orders of magnitude smaller. An under-sampling would not be surprising, given the bias inherent in color- and spectroscopy-based searches. These selection requirements would have missed a few known He CVs that were discovered previously via their variability (Solheim 2010).

Still, Nelemans et al. (2001) acknowledge large uncertainties in their estimates, and inconsistencies among various numerical simulations. Some indicate that the CE serves as a sufficient angular momentum drain to bring the stars close enough for mass transfer to begin, while others show that the envelope merely spins up to co-rotate with the binary, producing no drag.

Note: Citations are listed in the References section of Chapter 1.

APPENDIX I: Creating the model curves on the ε(P_{orb}) diagram

This appendix contains details of calculations used to construct the ε(P_{orb}) diagram for He CVs in Chapter 4.

Mass-radius relation for a cold sphere

For a sphere in hydrostatic equilibrium under its own gravity, there exists at unique M(R) relation. Zapolsky & Salpeter (1969) found, via numerical integration, an analytical formula for M(R) of a zero-temperature sphere as a function of atomic number Z.

The ingredients are:

1) Equations for hydrostatic equilibrium

$$\frac{dP(r)}{dr} = -GM(r)r - 2\rho(r) \tag{I.1}$$

$$\frac{dM(r)}{dr} = 4\pi r\rho(r) \tag{I.2}$$

2) Boundary condition: P(R) = 0;
3) Consideration of the relative strengths of gravity, electrostatics, and Fermi pressure, for a range of masses;
4) A previously-derived ρ(P) relation.

The result, for a fully-degenerate low-mass star of He composition, is Eq. 4.3:

$$R_{zs} = 0.0155{M_2}^{-0.212}$$

Mass-radius relation for a partially-degenerate He star

Savonije et al. (1986) presented evolutionary calculations of a model ultracompact contact binary, consisting initially of a 0.6M_{sun} nondegenerate He star and 1.3M_{sun} primary white dwarf, with a certain initial orbital separation a. The initial orbital separation a governs the time of onset of mass transfer, and hence the state of evolution of the Helium star at this time. Given an initial P_{orb} of 37 min, they find that this model star immediately commences RLOF and mass transfer – while the secondary is still in its core He burning phase. Their model assumes conservative mass transfer and that any angular momentum losses are due to GWR.

They found that this system's evolution is governed by three timescales: t_{ev} (evolutionary timescale), t_g (timescale of angular momentum loss due to GWR), and t_{KH} (the Kelvin-Helmholtz, or thermal, timescale.) GWR causes the system to shrink, while mass transfer to a more massive primary tends to oppose that shrinkage. Eventually the mass loss wins out and the system reaches a period minimum (~ 11 minutes for this system.)

A general M(R) relation for the secondary is:

$$\frac{R_2}{R_{sun}} = \alpha \frac{M_2}{M_{sun}}^{\beta} \tag{I.3}$$

Near the period minimum, the (now partially-degenerate) secondary obeys the above M(R) relation with coefficients $\alpha = 0.029$ and $\beta = -0.19$. Thus for a partially-degenerate secondary, we shall approximate the M(R) relation as:

$$R_2 = 0.029 {M_2}^{-0.19}$$

with R_2 and M_2 in solar units (Savonije et al. 1986) – which is Eq. 4.4.

Because of the extreme under-luminosity of the secondary at this point (caused by severe mass loss), its thermal timescale has grown much longer than a Hubble time. Thus it is expected to remain partially-degenerate for a substantial part of its subsequent life.

Drawing the curves in $\varepsilon(P_{orb})$ space

The two solid lines on the ε-P_{orb} plot (Fig. 4.1) represent He CVs whose secondaries are fully-degenerate white dwarfs (lower line) and partially-degenerate He star (upper line), according to their respective M(R) relations explained above. Each curve represents $M_1 = 0.75M_{sun}$, and each shaded region represents $0.6 < M_1 < M_\odot$, which is a reasonable mass range for a white dwarf in a binary (e.g. Knigge et al. 2006). These lines were constructed according to the following considerations.

First we obtain ε in terms of M_2. From Kepler's law and the approximation that R_2 is the volume-averaged Roche lobe radius for a low-mass star (Eq. 4.2):

$$P_{orb} = 8.75(\frac{{R_2}^3}{M_2})^{\frac{1}{2}}$$

Then, taking Eq. 1.18 and $<M_1> = 0.75M_{sun}$, we obtain: $q = 1.33M_2$. So:

$$\varepsilon = 0.240M_2 + \ 0.513{M_2}^2 \qquad \text{I.4}$$

For a fully-degenerate secondary:

Eq. 4.3 and I.4 yield:

$$M_2 = \frac{0.0069}{{P_{orb}}^{1.22}} \qquad \text{I.5}$$

Eq. 1.18 and I.5 yield:

$$\varepsilon = \frac{0.002}{{P_{orb}}^{1.22}} + \frac{2.44e^{-5}}{{P_{orb}}^{2.44}} \qquad \text{I.6}$$

Eq. I.6 corresponds to the lower solid line on Fig. 4.1.

For a partially-degenerate He star secondary:

Eq. 4.4 and I.4 yield:

$$M_2 = \frac{0.018}{P_{orb}{}^{1.27}} \qquad \text{I.7}$$

Eq. 1.18 and I.7 yield:

$$\varepsilon = \frac{0.004}{P_{orb}{}^{1.27}} + \frac{1.68e^{-4}}{P_{orb}{}^{2.54}} \qquad \text{I.8}$$

Eq. I.8 corresponds to the upper solid line on Fig. 4.1.

Error estimations

The following calculations were performed to obtain errors δε , and δq for each CV.

1) Getting δε from δP_{sh} and δP_{orb}:

$$\frac{\delta\varepsilon}{\varepsilon} = \frac{\delta P_{sh} + \delta P_{orb}}{P_{sh-}P_{orb}} - \frac{\delta P_{orb}}{P_{orb}} \qquad \text{I.9}$$

2) Getting δq from δε:

$$\varepsilon(q) = 0.18q + 0.29q^2$$

So:

$$q = \frac{-.18 + \sqrt{.0324 + 1.16\varepsilon}}{.58}. \qquad \text{I.10}$$

If

$$q = f(\varepsilon)$$

Then

$$\delta q = f'(\varepsilon)\delta\varepsilon$$

and

$$f'(\varepsilon) = \frac{1}{\sqrt{(.0324 + 1.16\varepsilon}} \qquad \text{I.11}$$

Note: Citations are listed in the References section of Chapter 4.

APPENDIX J: Speculations regarding the nature of the 12 CVs of Table 7.3

This section is a speculative discussion of observations regarding the 12 CVs with likely retrograde precession periods (Table 7.3). These 12 objects have had simultaneous detections of negative superhump and superorbital periods, such that the superorbital period can be interpreted as the retrograde precession period of a tilted accretion disc. The following observations shall be considered within the context of the tilted-disc model.

- Most systems with simultaneous superorbital and negative superhump periods have mass ratios less than ~ 0.35.
- Most CVs with superorbital periods experience continuous bright states over timescales of at least months.
- Superorbital and negative superhump periods in CVs persist on timescales of at least weeks to months, and take at least weeks to develop and decay.
- About half of systems that show negative superhumps also show *positive* superhumps.

Most systems with simultaneous superorbital and negative superhump periods have mass ratios less than about 0.35.

This estimation was made using the relation between P_{orb} and secondary mass derived by Knigge (2006); the only two outliers are TV Col and TX Col. This observation is difficult to interpret. It is possible that the apparent requirement of low q is attributable in large part to selection bias. For H CVs, $q < 0.3$ translates to a P_{orb} below or just slightly above the period gap. Possibly because systems in this P_{orb} range were most numerous among the earliest observations of negative superhumps, they are the preferred targets for negative superhump searches. We also note, however, that most of CVs with non-detections of superorbital periods (~ 100) have mass ratios greater than ~ 0.4 (private communication: Joe Patterson).

Most CVs with superorbital periods experience continuous bright states over timescales of at least months.

This observation, that at least an occasional high mass transfer rate appears to be a requirement for the creation of a superorbital period associated with retrograde disc precession in a CV, is consistent with models that attribute enhanced mass transfer to tilted-disc geometry. Superoutbursts of some dwarf novae and other high-state behaviors of CVs have been modeled by invoking irradiation-induced mass outflow (e.g. Smak 2008, Smak 2009a). In this model, a disc that is aligned in the orbital plane will partially shadow the secondary from irradiation by the primary, while a tilted disc may expose the secondary to greater irradiation, thus simultaneously enhancing $\dot{M}$ and the amplitudes of negative superhumps and superorbital period modulations.

Other observational studies, however, indicate that the length of the superoutburst cycle does not depend on the presence or absence of negative superhumps (Osaki & Kato 2013; Zamko et al. 2012), a finding that is not consistent with a model in which $\dot{M}$ is affected by disc tilt. Furthermore, a few superorbital periods have been found in faint systems that have never been known to experience an outburst.

Superorbital and negative superhump periods CVs persist on timescales of at least weeks to months, and take at least weeks to develop and decay.

This observation was noted by Patterson et al. (2002) and is difficult to interpret. We tentatively invoke the work on protostellar discs by Lubow & Ogilvie (2002): Those authors showed that at certain resonances in a protostellar disc, tilt will be damped out on a timescale that is approximately the viscous timescale: about 10^3 orbits. The timescale of damping of superorbital and negative superhump periods (of weeks to months) is also roughly 10^3 orbital periods (hours to days). Again, this is a speculative suggestion; it has not been shown convincingly that the work by Lubow & Ogilvie (2000) can be extended to CVs.

About half of CVs that show negative superhumps also show *positive* superhumps.

Example systems include V603 Aql (Patterson et al. 1997), and V442 Oph and RX J1643.7+3402 (Patterson et al. 2002). (For a comprehensive list, see Table 2 of Montgomery 2009). Within each system, the amplitude of modulation of the negative superhump is within a factor of ~ 1/3 to 3 that of the positive superhump. Negative superhumps take longer to develop and decay than do positive superhumps: weeks to months, as opposed to days. As positive superhumps are associated with high-state activity, this observation may be consistent with a model in which a tilted disc exposes the secondary to enhanced irradiation – and hence causes an enhanced mass accretion rate.

Note: Citations are listed in the References section of Chapter 6.

Appendix K: Non-detection of the Tooth Fairy at Optical Wavelengths

The following study was submitted to arXiv on 2012 April 1 and appeared there on April 3 (arXiv:1204.0492). While it does not pertain directly to the topics discussed in this dissertation, the results are sufficiently noteworthy to merit an appendix.

K.1 Abstract

We report a non-detection, to a limiting magnitude of V = 18.4 (9), of the elusive entity commonly described as the Tooth Fairy. We review various physical models and conclude that follow-up observations must precede an interpretation of our result.

Key words: Photometry, multi-wavelength studies, magical creatures: Individual (Tooth Fairy).

K.2 Introduction

The Tooth Fairy is a common figure worldwide, and particularly in the United States and Europe (Wikipedia 2012). The creature is associated with a recently-lost human tooth that is usually deciduous in nature. With as-yet undetermined motivations, the creature purloins these teeth and in exchange leaves behind small gifts. The recently de-toothed person, of age 5.6 (18) (Seuss, Dr. 1981), expects this burglary and, in fact, eagerly anticipates it, typically placing the tooth in a readily accessible location[1]. Despite potential barriers such as bolted front doors and

---

[1] In Europe and the United States, traditionally a child places the tooth under a pillow at bedtime. The Tooth Fairy's gift subsequently appears under this pillow the following morning. In some Asian countries, tradition somewhat complicates the Tooth Fairy's job of finding the tooth: in Korea and Vietnam, for example, a child typically throws the tooth upwards if it came from the lower jaw, or down to the ground if it came from the upper jaw, with the goal of encouraging future teeth to grow in a desirable orientation. The Tooth Fairy is less common in African cultures.

ornery Rottweilers, it appears that the Tooth Fairy obtains the tooth with minimal difficulty, arriving and departing undetected. Indeed, the only observational evidence of the being's transient presence is the vanishing of the tooth in question.

While there exists general consensus regarding the Tooth Fairy's perplexing fetish for discarded human remains, the precise identity of the Tooth Fairy is a contentious topic. Fig. K.1 depicts a representative array of suggested visual counterparts. The majority (74%) believe the

Fig. K.1a: Common depictions of the Tooth Fairy as a female of approximately-human form.

Fig. K.1b-g: Other representations.

REFERENCES. (a: top left) Armstrong 2012a; (a: top right) overstock.com 2012; (a: bottom left) Isbister & Clotworthy 2012; (a: bottom right) Rubies' Costumes 2012; (b) Yeager 2011; (c) Sandoval 2012; (d) Johnson 2012; (e) Armstrong 2012b; (f) stock.xchng.com 2012; (g) Armstrong 2012c.

Tooth Fairy to be a female of approximately[2] human form (Fig. K.1a), while the remaining 26% suggest a myriad of alternatives including man (Fig. K.1c), bear (d), bat (g), bunny rabbit (f), dragon (b), and dental hygenist (e). For simplicity, we shall hereafter refer to the Tooth Fairy using the feminine gender class.

To date, all pictorial representations summarized in Fig. K.1 are speculative. A robust detection of the Tooth Fairy has not been obtained in any bandwidth. A tentative infrared detection was reported based on the experience of a six-year-old Nebraskan boy: “I felt a warm breath on my ear, but it mighta just been my stupid kid sister trying to stick another bug up my nose” (Fox News 1997). No follow-up observation was conducted. Furthermore, the boy’s kid sister subsequently awoke with a suspiciously-fresh black eye, lending credence to his theory that she had been the bedside visitor. Searches for optical and high-energy counterparts to the Tooth Fairy have not been conducted. Here we report on a study aimed to remedy this oversight.

K.3 Observations

Observations were conducted with the MDM 1.3-meter telescope, using a CCD specially designed for near-Earth observations. The chip is 92,084 x 92,084 pixels, with a pixel length of 24 microns. The full unbinned chip yields a 0.38-arcsecond-per-pixel field of view. To push the limiting magnitude on each exposure, we set the integration time at four seconds. This time resolution suited our purposes, assuming that an open-air tooth robbery might be as fast as five seconds. In addition, we used a quarter of the chip area binned 2x2, to reduce readout time to around four seconds. The resulting limiting V magnitude on each image was 18.4 (9).

On the evening of 2012 Mar 31, this author configured a sleeping arrangement on the

---

[2] Embellishments include wings, fairy dust, and ostentatiously pointy ears.

roof of the neighboring 2.4-meter observatory, which has an unobstructed line of sight to the 1.3m dome slit. The distance of the author's sleeping bag to the 1.3m telescope input pupil was 47 (1) m. A wisdom tooth, freshly removed from the author's lower left jaw, was placed under a pillow, upon which the author subsequently laid her head and fell asleep.

The telescope was programmed to obtain an eight-hour time series of a two-meter-radius circle centered on the author's sleeping bag. For a distance of 47 m, the limiting absolute magnitude M_v is 97.5 (9). We performed data reduction via standard UNIX and IRAF scripts. The resulting light curve is a plot of differential magnitude with respect to a 1.0 (6)-Watt flashlight that was left shining near the sleeping bag throughout the night. Fig. K.2 shows the light curve of the eight-hour time series; the right panel is one representative image. Virtually all frames look alike, with the exception of a brief incident occurring around HJD = 2456018.5000 (see *Analysis*). The sky remained photometric throughout the night. Finally, at the end of the observation, the author's wisdom tooth could not be localized.

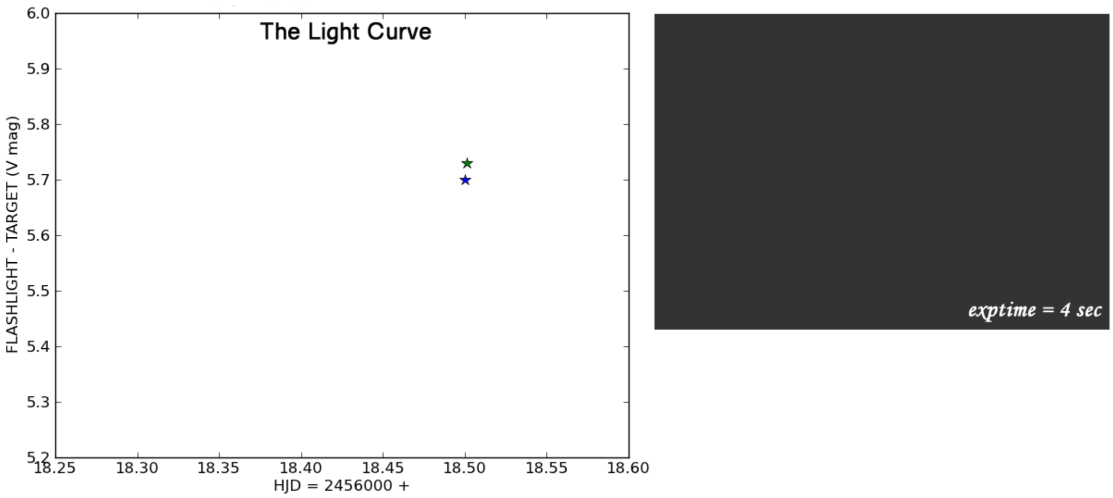

Fig. K.2: *Left*: Light curve of eight-hour time series (2012 March 31). *Right:* A representative four-second exposure from the time series.

K.4 Analysis

K.4.1 Features of the light curve and power spectrum

The single noteworthy characteristic of the light curve is the brief brightening at HJD = 2456018.5000-1, as shown in Fig. K.2. An inspection of a fresh bite upon the author's forehead the following morning, in addition to the author's veritably-annoyed personal narrative, indicated that the optical counterpart was a mosquito that had ventured close approach to the flashlight. The average mosquito luminosity over the two images upon which it appeared was 0.005 (1) W, which yielded a differential magnitude with respect to the 1.0 (6) W flashlight of V = 5.75 (9). Otherwise the light curve appears unremarkable.

Next we created a Lomb-Scargle periodogram of the full time series. The Lomb-Scargle technique is similar to the discrete Fourier transform and is equivalent to least-squares fitting. We performed this transformation because it is what our software does and we hadn't any better ideas. The left panel of Fig. K.3 shows the power spectrum, with the strongest feature around 143-9 cycles per day (c d^{-1}) noted (the low frequency resolution is not entirely unexpected, given

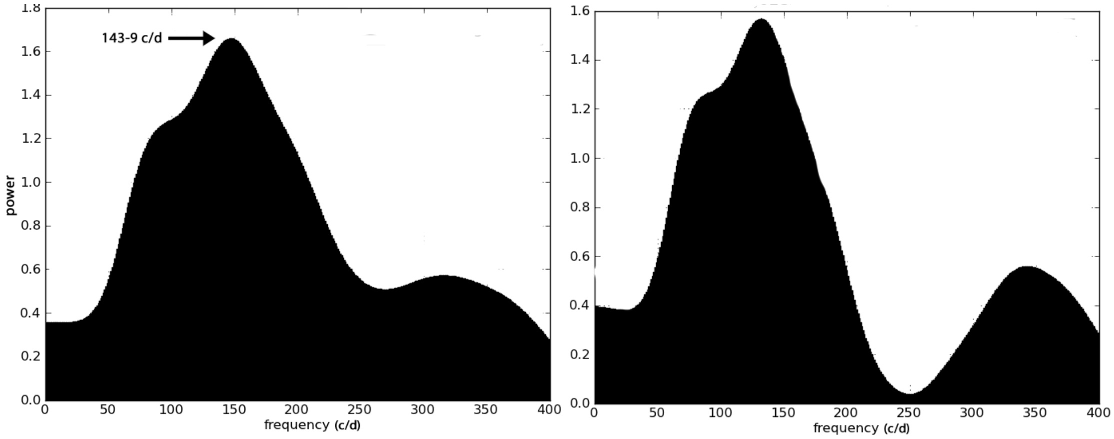

Fig. K.3: *Left*: Lomb-Scargle power spectrum of full light curve. The strong feature at ~ 145 c d^{-1} is noted. *Right*: Prewhitened power spectrum, after the attempted removal of the strongest feature (best-fit $\upsilon = 145.40$ c d^{-1}).

our sample size of two points). To assess the feature's significance, we performed Monte Carlo simulations assuming a typical error of 0.02 mag. The false alarm probability is 97.2 per cent.

To search for weaker periodicities, we modeled the 143-9 c d^{-1} signal as a sinusoid, finding a best fit at υ = 145.40 c d^{-1}, and subtracted this wave from the original light curve. The prewhitened power spectrum (Fig. K.3: *right panel*) looks even worse, which is also unsurprising, given our attempt to model an unresolved feature as a wave of one discrete frequency. At this point we gave up and went inside to make breakfast.

K.4.2 The tooth

As noted above, the wisdom tooth that had been placed beneath the author's pillow prior to the start of observations was not present under the author's head the following morning. (Neither, incidentally, was the pillow. The pillow had tumbled down the sloped roof and come to alight upon a tumbleweed that was resting aside the dormitory wall). We searched for the tooth for five entire minutes, the result of which confirmed our initial null finding.

K.5 Discussion: *Faster-than-light Tooth Fairy?*

Given the tooth disappearance, we conclude that the Tooth Fairy visited during the night. How, then, to account for our non-detection? First, we remind the reader of our limiting time resolution of four seconds for both the exposures and deadtime between images. We had placed a lower limit of five seconds on an expected Tooth Fairy visit, including arrival and departure. However, this estimate is based on the typical timeframe for a *human-based* crime. The assumption that the Tooth Fairy operates on human timescales is speculative, and may have rendered erroneous the lower limit on total visit duration. Indeed, recent discoveries indicate that some non-human entities such as neutrinos (e.g. Adam et al., 2011; Ereditato 2012) and the president of Iran (The Colbert Report 2012) may indeed travel at near-luminal speeds. Thus it is desirable to obtain an observation of higher time resolution, using a collecting area sufficiently large to offset any loss of brightness sensitivity.

K.6 Conclusion

We report a non-detection of the Tooth Fairy at optical wavelengths fainter than V = 18.4 (9), using a time resolution of four seconds. The distance of 47 (1) meters to our target yields a limiting absolute magnitude of M_V = 97.5 (9). It is important to obtain follow-up data in the optical band at higher time resolution with an instrument of larger collecting area, as well as multi-wavelength studies, which have yet to be conducted.

In particular, we expect optical and infrared observations to be relatively straightforward to conduct. Radio detection will present a significant creative challenge, as the surface area to be resolved is on the order of a meter. High-energy observations are probably premature: because it is not known whether the Tooth Fairy ever leaves the Earth's atmosphere, a non-detection from satellite imagery will not necessarily be diagnostic. Thus, a more thorough theoretical framework must precede an interpretation of any high-energy observations.

Finally, we note preliminary evidence that not only is the Tooth Fairy transparent at optical wavelengths, she is also a stingy sonnuvabitch. She left behind nary a penny! We tentatively attribute this swindle to spite: perhaps the creature took offense at what might be interpreted as a crass and deliberate invasion of her privacy.

K.7 Acknowledgements

This research was funded by quarters pilfered from the snack machine up at the Kitt Peak Visitors' Center. This dissertation author was the primary investigator and author of the material.

REFERENCES

[1] Adam, T., Agafonova, N., Aleksandrov, A., Altinok, O., Alvarez Sanchez, P., Anokhina, A., Aoki, S., Ariga, A., et al. 2011, arXiv:1109.4897

[2] Armstrong, E. *Pretty Fairy Drawing*, 2012a

[3] Armstrong, E. *Photograph of My Husband Wayne Yeager Dressed Up as a Dental Hygienist*, 2012b

[4] Armstrong, E. *Bat*, 2012c

[5] [3]*Can Your Child Sense Invisible Monsters*? Fox News Channel, 1997 May 22

[6] Ereditato, Antonio. *OPERA experiment reports anomaly in flight time of neutrinos from CERN to Gran Sasso.* CERN. 2012 Feb 23 http://press.web.cern.ch/press/PressReleases/Releases2011/PR19.11E.html

[7] *Indecision 2012 - New Hampshire GOP Debates*. The Colbert Report. Jon Stewart, Tom Purcell, Stephen Colbert (prod); Jim Hoskinson (dir). Comedy Central. New York, 2012 Jan 9

[8] Isbister, Karen; Clotworthy, Carrie. *Pass It! Dental Hygiene Edition Board Game;* www.PassItGame.com, 2012

[9] Johnson, Nick. http://www.flickr.com: studiod_baltico1, 2012

[10] Overstock.com. *Tooth Fairy Collectible Musical Doll*; item 11496301, 2012

[11] Rubies' Costume Company, Inc. *Fantasy Fairy,* item 889137; www.rubies.com, 2012

[12] Sandoval, Dain. www.flickr.com, 2012

[13] Seuss, Dr., T. The Tooth Book. Random House, 1981

[14] Stock.xchng.com: *Confused Bunny*, 2012

[15] *Tooth Fairy*. Wikipedia, the Free Encyclopedia. Wikimedia Foundation, Inc. Web. 2012 Mar 31

[16] Yeager, Wayne. Polymer Clay Butterfly-style Dragon; http://www.etsy.com/shop/JackTheDragon, 2011

[3] Okay, we admit it: this one we made up.